Titre: Title:	Improving Geometric Accuracy of Fused Filament Fabrication (FFF) 3D Printed Parts by Computational Analysis of Digitized Sacrificial Parts
Auteur: Author:	Moustapha Jadayel
Date:	2024
Type:	Mémoire ou thèse / Dissertation or Thesis
Référence: Citation:	Jadayel, M. (2024). Improving Geometric Accuracy of Fused Filament Fabrication (FFF) 3D Printed Parts by Computational Analysis of Digitized Sacrificial Parts [Thèse de doctorat, Polytechnique Montréal]. PolyPublie. https://publications.polymtl.ca/59432/

POLYTECHNIQUE MONTRÉAL
affiliée à l'Université de Montréal

Improving Geometric Accuracy of Fused Filament Fabrication (FFF) 3D Printed Parts by Computational Analysis of Digitized Sacrificial Parts

MOUSTAPHA JADAYEL
Département de génie mécanique

Thèse présentée en vue de l'obtention du diplôme de *Philosophiæ Doctor*
Génie mécanique

Août 2024

POLYTECHNIQUE MONTRÉAL
affiliée à l'Université de Montréal

Cette thèse intitulée :

Improving Geometric Accuracy of Fused Filament Fabrication (FFF) 3D Printed Parts by Computational Analysis of Digitized Sacrificial Parts

présentée par **Moustapha JADAYEL**
en vue de l'obtention du diplôme de *Philosophiæ Doctor*
a été dûment acceptée par le jury d'examen constitué de :

Abolfazl MOHEBBI, président
Farbod KHAMENEIFAR, membre et directeur de recherche
Oguzhan TUYSUZ, membre
Sasan SATTARPANAH KARGANROUDI, membre externe

DEDICATION

À Salam, source de paix.

ACKNOWLEDGEMENTS

I sincerely thank Professor Farbod Khameneifar, my research director, for his guidance, expertise, and steadfast support throughout this journey. His mentorship has been instrumental in shaping not only my research but also my academic and professional development.

To Salam, my wife, whose unwavering patience, understanding, and encouragement sustained me through the challenges of this doctoral journey, I owe a debt of gratitude that words cannot express. This accomplishment is as much hers as it is mine, and I am profoundly grateful for her unwavering belief in me.

I also want to express my sincere appreciation to the team at Polyfab Normand Brais for their collaboration and assistance, which significantly enriched the practical aspects of my research. Their expertise and resources have been invaluable.

Special thanks to the applied mechanical engineering lab technicians for their technical assistance and support. Their dedication and proficiency were indispensable in executing experiments and analyses.

I am also grateful to the Fonds de Recherche du Québec—Nature et Technologies (FRQNT) for their financial support, which enabled me to pursue this research endeavor.

My gratitude also extends to all supporting personnel whose contributions, large and small, were crucial in completing this thesis.

Lastly, I want to express my heartfelt thanks to all my friends and colleagues who have supported me throughout this challenging yet rewarding journey.

RÉSUMÉ

La technologie d'impression 3D de Fabrication par Filament Fondu a gagné une traction et un intérêt significatif dans diverses industries et dans la communauté scientifique en raison de son faible coût et de sa polyvalence. Cependant, atteindre une haute précision géométrique reste un défi, notamment pour les machines d'usage en millieu de bureau ou laboratoire. Ces machines n'ont pas de systèmes en boucle fermée pour garantir le positionnement de la buse déposant le matériau. Elles peuvent être utilisées avec divers matériaux tels que l'Acide Polylactique (PLA), le Polyuréthane Thermoplastique (TPU) ou même des matériaux s'apparentant au chocolat. Les déformations thermomécaniques propres à chaque matériau affectent aussi la qualité géométrique du processus d'impression 3D due à la haute température du matériau nécessaire pour le déposer sur le plateau de construction de la machine ou sur les couches précédentes.

Cette thèse postule qu'il existe deux composantes aux déviations d'une pièce imprimée en 3D: la composante systématique, qui peut être répétée d'une itération à l'autre en utilisant la même machine avec les mêmes paramètres d'impression, et l'erreur aléatoire, qui est le produit de facteurs externes, de la composition non uniforme du matériau et des vibrations causées par le mouvement de la machine. Cette dernière composante ne peut pas être prédite avant le processus d'impression et donc ne peut pas être réduite que par l'augmentation de la stabilité du processus d'impression lui-même. En revanche, les déviations systématiques pourraient être connues avant le début du processus d'impression et peuvent être améliorer de manière générale en appliquant l'inverse des déviations systématiques à la géométrie qui sera imprimée. Dans cette thèse, cela se traduit par l'ajustement du maillage de surface de la géométrie nominale.

Ce document présente nos recherches pour déterminer comment extraire les déviations systématiques d'une imprimante 3D basée sur des mesures de pièces imprimées en 3D à l'aide d'un scanner 3D à lumière structurée. Nous démontrons d'abord qu'une moyenne des déviations mesurées des pièces imprimées en 3D peut être utilisée pour approximer les déviations systématiques d'une pièce imprimée en 3D et que l'utilisation de la déviation moyenne pour compenser le maillage de surface nominal donne des résultats positifs. Les mesures de déviation moyenne consomment cinq pièces sacrificielles, ce qui est à la fois une perte de temps et de matériau significatif. C'est également spécifique à un matériau et à une machine à un moment donné. Nous proposons, donc, ensuite un algorithme de compensation d'apprentissage automatique constitué de deux composantes : l'algorithme de prétraitement qui crée une

image du voisinage de déviation local d'un point nominal et un réseau de neurones convolutif qui interprète ces images pour déduire la proportion de déviation systématique à ce point. Le processus présente l'avantage d'être généralisable pour n'importe quelle machine et n'importe quelle géométrie à condition que suffisamment de données aient été utilisées dans le processus d'entraînement. Cet algorithme d'apprentissage automatique réduit le nombre de pièces sacrificielles nécessaires ; une seule pièce sacrificielle mesurée à l'aide d'un scanner 3D à lumière structurée est nécessaire pour approximer les déviations systématiques. Enfin, une incursion dans les mesures en cours de processus de pièces imprimées en 3D est présentée, montrant que des investigations supplémentaires sont nécessaires pour modéliser adéquatement les déviations des pièces à mi-parcours dans le processus d'impression 3D.

ABSTRACT

Fused Filament Fabrication 3D printing technology has gained significant traction and interest in various industries and the scientific community due to its cost-effectiveness and versatility. However, achieving precise geometric accuracy remains challenging, particularly for desktop-sized machines. These machines lack closed-loop systems to ensure the positioning of the material-depositing nozzle. They can be utilized with materials like PolyLactic Acid (PLA), Thermoplastic PolyUrethane (TPU), or even chocolate-like materials. By raising the temperature of the material just as it is deposited on the machine's build plate or previous layers, thermomechanical deformations unique to each material also affect the geometric quality of the 3D printing process.

This thesis suggests that deviations in 3D printed parts have two components: systematic and random errors. Systematic errors are repeatable with the same machine and parameters, while random errors come from external factors, nonuniform material, and machine vibrations. Random errors cannot be predicted before printing and can only be reduced by improving the stability of the printing process. On the other hand, systematic deviations could be known before the printing process and can be acted upon holistically by applying the inverse of the systematic deviations to the geometry that will be printed. In this thesis, this translates to morphing the surface mesh of the nominal geometry.

This document details our investigations into determining the systematic deviations of a 3D printer based on measurements of 3D printed parts using a structured light 3D scanner. We first demonstrate that an average of measured deviations of 3D printed parts can approximate the systematic deviations of a 3D printed part and that using the average deviation to compensate the nominal surface mesh yields an improvement in the average of absolute geometric error of 55%. The average deviation measurements consume five sacrificial parts, which are both wasteful in time and material. They are also specific to a material and a machine at a time. We also propose a compensation Machine Learning algorithm of two components. The pre-processing algorithm creates an image of a nominal point's local deviation neighborhood, and a Convolutional Neural Network interprets these images to infer the systematic deviation. The process can be generalized for any machine and geometry on the condition that enough data was used in the training process. This machine learning algorithm reduces the number of sacrificial parts needed; only one sacrificial part measured using a structured light 3D scanner is necessary to approximate the systematic deviations. By applying the inverse of the systematic deviation inferred by the compensation machine

learning algorithm, an improvement in the average of absolute geometric error of 88.5% was demonstrated. Finally, a foray into in-process measurements of 3D printed parts is shown, showing that more investigations are needed to adequately model deviations of parts midway in the 3D printing process.

TABLE OF CONTENTS

LIST OF TABLES

LIST OF FIGURES

LIST OF SYMBOLS AND ACRONYMS

AM	Additive Manufacturing
PPE	Personal Protective Equipment
FDM	Fused Deposition Modelling
FFF	Fused Filament Fabrication
SLA	Stereolithography Apparatus
SLS	Selective Laser Sintering
SLM	Selective Laser Melting
DMLS	Direct Metal Laser Sintering
EBM	Electron Beam Melting
CAD	Computer-Aided Design
FEA	Finite Element Analysis
ICP	Iterative Closest Point
STL	Standard Tessellation Language
GD&T	Geometric Dimensioning and Tolerancing
CMM	Coordinate Measuring Machine
DIY	Do-It-Yourself
RP	Rapid Prototyping
ABS	Acrylonitrile Butadiene Styrene
PLA	Poly-Lactic Acid
PA	Poly-Amide
ASA	Acrylonitrile Styrene acrylate
PC	PolyCarbonate
PET	PolyEthylene Tetraphtalate
PEEK	Poly-Ether-Ether-Ketone
PEI	PolyEtherImide
VDI	Association of German Engineers
ANN	Artificial Neural Network
MLP	MultiLayer Perceptron
DNN	Deep Neural Network
CNN	Convolutional Neural Network
ReLU	Rectified Linear Unit
VGGNet	Visual Geometry Group Network
ResNet	Residual Network

PID	Proportional Integral Derivate
CALC	Circular Approximation with Selective Cornering
PALC	Polygon Approximation with Local Compensation
GPKS	Gaussian Process Kernel Smoothing

CHAPTER 1 INTRODUCTION

For most, the concept of accuracy and precision originates as simply an element of the industrial revolution. Indeed, the need to create interchangeable parts was a significant driver for improving the accuracy of manufacturing machines [2]. Still, the need to be precise in one's work predates the Industrial Revolution by many millennia, notably in the study of astronomy, surveying, and horology [3], where instruments from different artisans needed to agree on the exact measurement. Throughout history, the need for precision steadily grew, and in centuries before the Industrial Revolution, some artisans were renowned for creating precise timepieces, navigation tools, and other instruments requiring incredible precision to be usable [4]. Today, accuracy and precision are paramount in most, if not all, industrial processes because they ensure product quality, consistency, and reliability. Accuracy refers to how close a measured value is to the true value, while precision indicates the consistency of repeated measurements. The rise of Metrology as a field of study has been driven by the need to develop new precision manufacturing methods and accurate measurements, which are essential for maintaining high standards in production and minimizing errors. This rise paved the way for newly developed manufacturing processes, like additive manufacturing, to be studied for their metrological potential.

1.1 Definitions and Basic Concepts

Additive manufacturing (AM) represents a burgeoning set of manufacturing processes characterized by adding material to build a part's geometry where needed. It starkly contrasts conventional manufacturing methods, which are often subtractive. AM techniques entail strategically adding material or support structures to offer unique design freedom, customization, and resource efficiency opportunities.

Additive manufacturing encompasses a variety of processes, including Fused Filament Fabrication (FFF) or Fused Deposition Modeling (FDM), Stereolithography Apparatus (SLA), Selective Laser Sintering (SLS), Direct Metal Laser Sintering (DMLS), and Electron Beam Melting (EBM). Each process has advantages and limitations, making it suitable for different applications. FFF/FDM, for instance, is widely used for rapid prototyping and producing low-cost, durable parts. Meanwhile, SLA is known for its ability to create high-resolution, detailed parts with smooth surface finishes, which is ideal for product design and dental applications. In contrast, SLS offers design freedom and is suitable for producing functional prototypes and complex geometries without supporting structures. Finally, DMLS and EBM

produce fully dense metal parts with excellent mechanical properties, making them suitable for aerospace, automotive, and medical applications.

However, each process comes with complexity regarding setup, material handling, and post-processing requirements. For example, powder-based and resin-based AM processes require adequate health and safety procedures to protect the user, and metal-based AM processes necessitate a large amount of power to solidify the added material. In contrast, filament-based processes might emit fumes or volatile organic compounds during printing, posing potential health risks if proper ventilation measures are not in place. FDM/FFF is nonetheless often considered the most straightforward AM process available today, largely thanks to its greater adoption by the Do-It-Yourself (DIY), small businesses, and research communities.

Unfortunately, the FFF process lacks performance in properties essential for the industrial sector, making it challenging to adopt for end-use products. Mechanical properties must be predictable when strain is imposed on the product. Researching and studying the mechanical properties of FFF allows researchers and engineers to develop better models to predict the mechanical properties of printed products based on their geometry and material using tools like Finite Element Analysis (FEA). Geometric accuracy might be the most crucial property that requires significant attention and continuous improvement from the academic community to facilitate the utilization of FFF in the industrial sector for end-use products. Achieving precise geometric dimensions and tolerances is essential for ensuring interchangeability, compatibility with other components, and meeting design specifications. In industrial applications where consistency and reliability are paramount, addressing dimensional variability, layer adhesion, and surface finish becomes imperative.

1.2 Problem Statement

Reliability in manufacturing accuracy is critical to ensure that manufactured parts will accomplish the required specifications. For AM, the specification could be the assembly of parts, the accurate representation of the CAD model for prototyping, or maintaining expected performance. For example, the aerospace industry needs a high level of geometric accuracy, as all airfoils are meticulously designed to offer optimal performances. Other parts of the airplanes are designed to use the minimum material possible with topological optimization, meaning the designed part could be close to the limit of tolerable strain, and missing material could mean failure. The automotive industry also follows the trend of reducing fuel consumption or augmenting the range of electric vehicles by using topologically optimized parts. Additionally, the medical sector needs high geometric accuracy because some parts manufactured for this industry must couple to a human body, and geometric imperfection

would result in an uncomfortable or even painful experience for the user.

In AM, the process of material addition involves many sources of volumetric errors, such as the mechanical inaccuracies of the machine itself, mathematical errors in the 3D representation of the geometry, the approximation errors of 2D slices to build a 3D part, the material shrinking and expanding due to changes in the temperature, humidity, or phase, impurities in the material itself, and more. Each of these sources of error can be difficult to ascertain due to their non-linearity and interactions. One method often used to obtain a representation of all sources of error is to measure a 3D printed part as-is and measure the deviation of the surface of the geometry. The measured deviations can be used to demonstrate how a fabricated part deviates. Still, a more thorough investigation will reveal that this deviation pattern is altered with every iteration due to the two components of deviations in the 3D printing process: random errors and systematic deviations. The problem arises when attempting to analyze the deviation of the surface of the geometry to determine how it could be improved.

This thesis aims to develop a methodology to enhance the geometric accuracy of desktop FFF 3D printers by harnessing the high-density and high-accuracy measurements obtained from structured light 3D scanners applied to actual 3D printed parts. This objective is then separated into three sub-objectives. First, determine how to affect the 3D printing process to reduce geometric deviations based on 3D deviation values measured on the surface of the entire geometry. Second, decide how to interpret structured light 3D scan data to obtain the optimal deviation value that can be acted on. Finally, create a model that can extract the optimal deviation values using as little data as possible. These objectives will be addressed in chapters 4, 5, 6 after a thorough review of the scientific literature in chapter 2 and chapter 3 which will further develop the objectives and the rationale. Chapter 7 will follow with general discussions and, finally, the conclusion in chapter 8.

1.3 Thesis Organization

While pursuing the primary objective outlined, we achieved two significant milestones, warranting the publication of our findings in two separate peer-reviewed journal papers. Additionally, throughout our research journey, we actively participated in conferences to present interim findings and engage in discussions with fellow academic community members. Furthermore, we expanded on our presentation for one of these conferences by publishing a paper to disseminate our findings widely and stimulate further discourse within the academic community. Each published paper mainly focuses on one sub-objective but still touches on all three. They are presented in chapters 4, 5, 6 after a thorough review of the scientific literature in chapter 2 and chapter 3 which further develops the research's objectives and rationale.

Chapter 7 will follow with general discussions and, finally, the conclusion in chapter 8.

Chapter 4 presents the paper entitled "Improving Geometric Accuracy of 3D Printed Parts Using 3D Metrology Feedback and Mesh Morphing". It determines the methodology to improve the geometric deviations of a desktop FFF 3D printer: we can apply the inverse of measured deviations on the surface mesh of the original geometry to obtain a compensated part that has improved geometric accuracy. This compensation method can also be improved upon by obtaining the deviation values averaged from five parts printed on the same machine. This process allows us to extract the systematic deviation field from the raw deviation, eliminating its random deviation component. The part compensated using the inverse of the systematic deviation field shows greater accuracy than the part compensated using the raw deviation field. This conclusion exposes that there is indeed an optimal interpretation of the 3D scan data, which is yet to be determined.

The second paper, titled "Determining Systematic Deviation Scalar Fields in 3D Printing using Convolutional Neural Networks: A Machine Learning Approach to Improving Geometric Accuracy" and presented in chapter 5, discusses a methodology to extract the systematic deviation scalar field from a singular raw deviation scalar field of a printed part. An ML model is presented, which uses a pre-processing step and a CNN model to compute systematic deviation values. The pre-processing step creates 2D images of the raw deviation field around each point of the nominal surface mesh, and the CNN model interprets these images with the hypothesis that systematic and random deviations present differently locally and globally in the deviation scalar field of a 3D printed part. By using the ML model, we can better interpret the raw 3D scan data, and we are also able to reduce the quantity of data required for each compensation.

The paper presented in chapter 6 published amidst the CIRP ICME ’23 conference discusses the first intermediary results produced from our research’s last logical step: implementing the compensation methodology in a closed-loop form directly on a 3D printer, which reduces the data needed to a minimum. The paper discusses The measurement discrepancies between in-process measurements and offline measurements. These discrepancies proved to be a roadblock important enough and outside of this research’s scope that stopped us from implementing the in-process compensation methodology.

CHAPTER 2 LITERATURE REVIEW

This chapter thoroughly reviews the literature on enhancing geometric accuracy in 3D printing, focusing on four primary axes. First, we present the foundational aspects of the FFF 3D printing process and its intrinsic relationship with geometric accuracy. Subsequently, we demonstrate the role of structured light 3D scanners in capturing a digital representation of manufactured parts for metrological purposes. We then review current methodologies and strategies to improve geometric accuracy within the FFF framework. Finally, we explore the burgeoning domain of Machine Learning applications for metrological qualification and improvement of FFF 3D printed parts, along with other solutions to similar problems in analogous fields.

2.1 FDM/FFF 3D Printing

FDM 3D printing was first developed in the mid-eighties [5] by Scott Crump, who would patent it and found *Stratasys* to commercialize it as a rapid prototyping (RP) process. It demonstrated many advantages that are still attributable to FDM 3D printing: reduced wasted material, creation of the printing program directly from the CAD model, and minimal post-processing required when the printing is done.

2.1.1 Process Overview of FDM/FFF 3D Printing

In FDM, the material is fed into a heated nozzle where its temperature is raised until it becomes malleable, allowing it to be extruded layer by layer to form the desired object, figure 2.1. The printer's nozzle then moves along a predefined path, depositing the flowing material onto the build platform or previous layers in a pattern dictated by the G-Code file 2.2. As the material is deposited, it quickly cools and solidifies, fusing with the previous layers to form the object's structure. Depending on the complexity of the design, support structures may be added to facilitate overhanging features. The G-Code file is constructed by slicing the CAD file to predetermined printing parameters like the printing temperature, the material feed speed, and the printing speed.

2.1.2 Applications and Considerations in FFF 3D Printing

Researchers explored use cases other than rapid prototyping early in developing the FFF process. One such use case is printing the part in wax or similar material for use in a

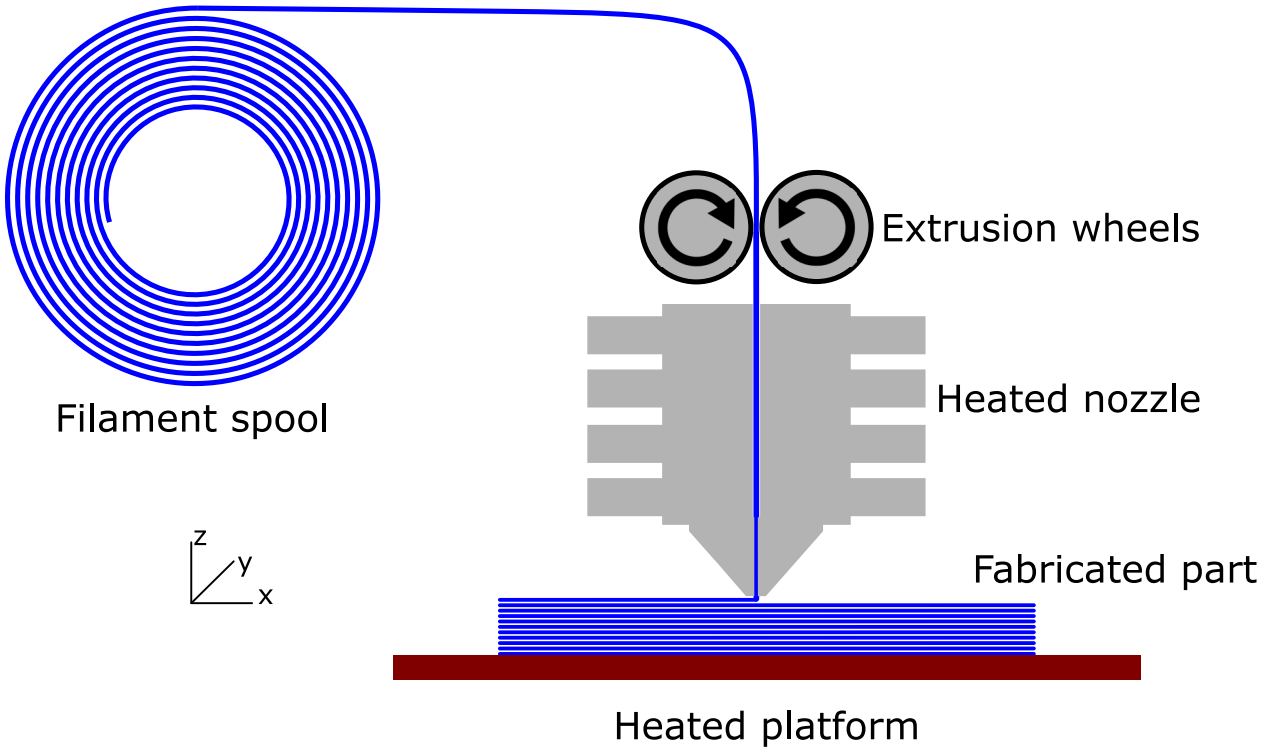

Figure 2.1 Diagram of the 3D printing process using the FDM technique. Inspired by Comb et al. [1]

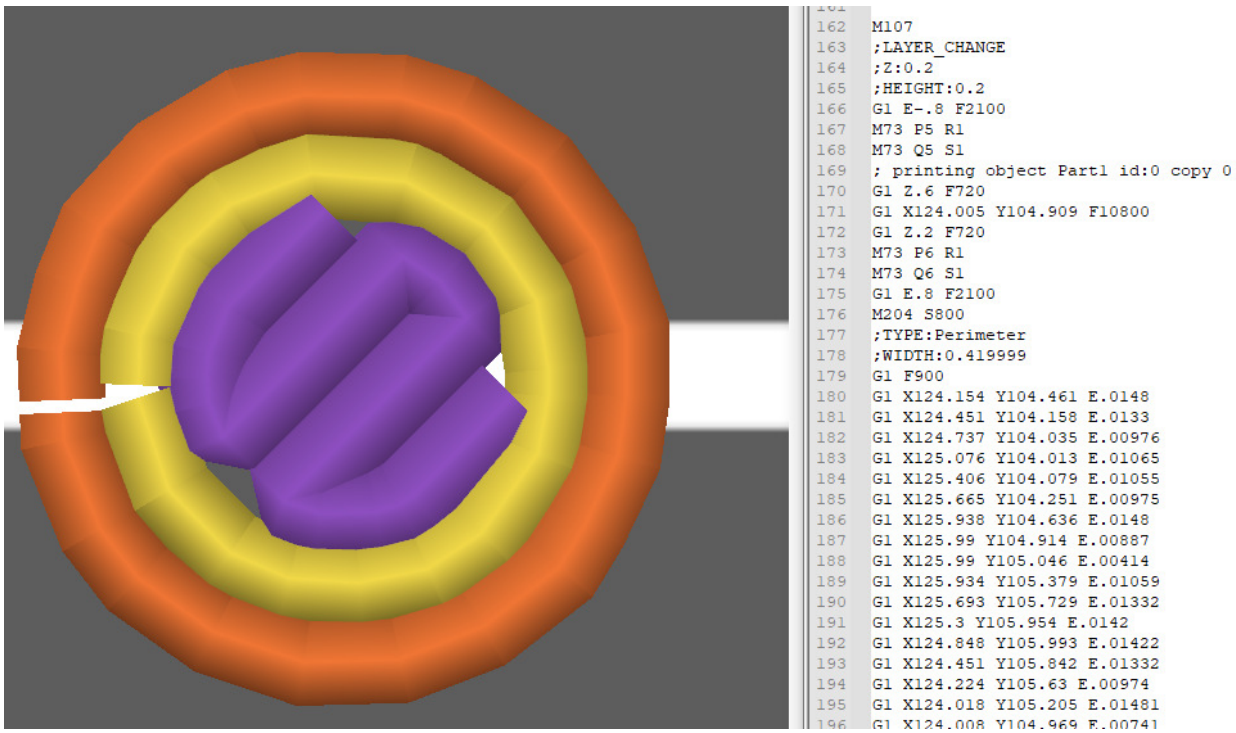

Figure 2.2 G-code example and representation in PrusaSlicer of a small cylinder.

foundry [6]. In situations where the creation of the sacrificial wax geometry is cost-prohibitive or too slow, FDM can present itself as a rapid tooling method and reduce the cost associated with a small quantity production run. Lee et al. explore this opportunity by casting a part using an FDM printed part as the investment casting and studying the quality of the produced part [7]. In another study, Pal and Ravi examine different methods of using RP technologies, including FDM, to cast a part either indirectly or directly. Three routes are investigated: casting the printed part in sand directly, creating a silicone mold from the printed part first, then creating a wax part for investment casting, or creating an epoxy part for sand casting. They note that accumulating dimensional errors in each step of the routes is a significant issue [8]. Pal et al. later demonstrated that casting a part using an FDM part was the worst-performing RP platform, mainly due to the lack of dimensional accuracy [9].

2.1.3 Geometric Accuracy and Process Parameters in FDM/FFF 3D Printing

To develop knowledge of the geometric accuracy of FDM machines, Mahesh et al. developed a benchmark artifact to be measured by CMM. The result of measuring different features and features allows the user to compare the performance of an AM process to another [10]. Zhang and Chou demonstrated the interactions between the printing parameters and how they affect warpage, finding that printing speed is the parameter that affects it the most and that the interaction between road width and layer height is almost as important [11]. Sood et al. later employed a grey-Taguchi [12] method to analyze the effect of the layer thickness, part orientation, raster angle, raster width, and air gap on the dimensional accuracy of an FDM printed part. Using a Taguchi methodology, the authors could also analyze the interaction between the five process parameters. Including a grey method has enabled them to obtain the optimal set of parameters to reduce shrinkage. The authors also note that the grey-Taguchi method must be repeated for every geometry [13]. Hackney also investigated the process parameters required to produce accurate 3D printed parts for tooling and direct use and identified three primary sources of errors: Mathematical errors due to the approximation of part surfaces in the computer file format; The process-related errors stemming from the mechanical nature of the machine; material-related errors induced by the change in temperature and state of the material as it is being extruded and deposited on previous layers [14]. Bochmann et al. investigated the process-related errors and determined that the FDM machine's dimensional accuracy varied to the toolhead's position. The author determined that the error behavior might be improved by implementing better process planning, process control, and machine design [15].

2.1.4 Materials in FDM 3D Printing

In the early days of FDM 3D printing, the material selection was limited to Acrylonitrile Butadiene Styrene (ABS), elastomers, or investment casting wax [16]. In the past decade, Poly-Lactic Acid (PLA), Nylons (PA6 and PA12), Acrylonitrile styrene acrylate (ASA), PolyCarbonate (PC), and Polyethylene Terephthalate (PET) have emerged as prominent thermoplastics frequently utilized in FDM, complementing the longstanding use of ABS [17]. Engineering materials were also developed, in particular poly-ether-ether-ketone (PEEK) and PolyEtherImide (PEI), for their chemical stability [18,19] and good biocompatibility [20,21]. Besides utilizing thermoplastics, fibers can be incorporated into the material to enhance specific properties. Common base polymers include PLA, ABS, and Nylon, while the fibers may consist of Glass or Carbon in chopped or oriented forms [22].

Metal-based FDM, see figure 2.3, was also demonstrated to be a promising development, showcasing the potential for utilizing metal-based materials in FDM processes by using a combination of binder and metal powder [23]. Metal-based FDM enhances the overall advantages of powder-based metal AM, offering increased flexibility and cost-effectiveness, particularly beneficial for small-scale production runs [24]. The post-processing of metal FDM is more involved than for thermoplastic-based material, as the part needs to be debinded and sintered in specialized equipment, which affects the dimensions of the printed part. Indeed, Quarto et al. note that a part printed in a commercial 3D printer shrinks by approximately 16% in the X-Y plane and by 20% in the Z direction [25]. Pelligrini et al. evaluated the shrinkage of 17-4 PH stainless steel printed using a commercial FFF-style 3D printer. The authors demonstrated that the sintering process affects the geometric accuracy non-uniformly and depends on the sintering orientation, infill line direction, and aspect ratio [26].

Figure 2.3 A Metal FDM part printed using an Ultimaker S5 in 316L Stainless Steel.

2.1.5 Impact of Open-Source FFF 3D Printing on Accessibility and Research

In 2007, Dr. Adrien Bowyer developed the first Replicating Rapid Prototyper (RepRap) [27], an open-source FFF 3D printer initiated by the academic world and further developed in the open-source and open-hardware community. Reprap and other open-source low-cost FFF 3D printers enabled many to use a 3D printer for different projects without requiring a bigger budget, costing only 500 $. The cheapest 3D printer at that time still cost 9900 $ and, most importantly, did not allow for experimenting due to the closed nature of the hardware and software. Pei et al. analyzed the geometric accuracy of an artifact printed on a Level 3D printing machine, the RapMan. Despite the low quality of the produced part, the authors indicate many paths to improvement [28]. Johnson et al. evaluated another low-cost 3D printer, the CupCake CNC MakerBot, for its geometric accuracy. This study notably uses a 3D scanner to capture the entirety of the surface of the 3D printed part, enabling a more holistic view of the geometric deviations. This study claims that 97.7% of the scanned points are within +/- 0.5 mm, and the standard deviation for the data is 0.3101 mm [29]. Minetola and Galati demonstrated a methodology to improve the performance of different versions of an I3-style 3D printer by optimizing the printing parameters. The improved printers showed greater geometric accuracy and speed, showing the importance of parameter optimization in DIY/open-source 3D printers [30]. Minetola et al. also demonstrated the geometric tolerance capability of different AM systems, including a DIY FFF 3D printer and a commercial Ultimaker 2. This study points out the better geometrical accuracy of the Ultimaker 2 commercial 3D printer [31].

2.2 Structured Light 3D scanning

3D scanning technology has revolutionized the process of capturing real-world objects and environments with unparalleled resolution and detail, making it an indispensable tool across various industries and academic disciplines. Although the ideas and technology have existed since the late eighties [32,33], the application was quite limited. An important application of this technology was cultural conservationism, where artworks, e.g., sculptures, could be 3D scanned to obtain a digitized version of the object [34, 35]. The 3D scanners used in these projects were often tailor-made set-ups of a laser, range camera, spotlight, and digital color camera.

2.2.1 Process Overview of Structured Light 3D Scanning

Rochinni et al. later developed a low-cost 3D scanner using structured light. The authors combined a video projector to create patterns with a high-resolution digital camera set at an exactly known angle, as shown in figure 2.4. The camera captured the pattern's deformation on the subject and created a 3D representation of the observation [36] as seen in figure 2.5. While it is widespread today, using two cameras is unnecessary. It mainly helps index the pattern stripes in the case of self-occlusion [37]. Bieri and Jacot examined the potential for this system to enhance quality control in the production line. The main interest was the capacity of 3D scanning to capture the height dimension when capturing an image of the subject, and the authors developed methodologies to filter random phase noise and improve the efficacy of the projected pattern [38]. Voisin et al. examined the effect of color on the accuracy of the acquisition. The authors demonstrated that the color has a notable impact on the position of the captured points by way of noise with an amplitude that is consistent depending on the color of the surface [39]. Researchers have studied many other parameters to evaluate their effects on the accuracy of structured light 3D scanners, including the ambient temperature [40], the ambient light [41], the reflectivity [42] or the pattern used [29].

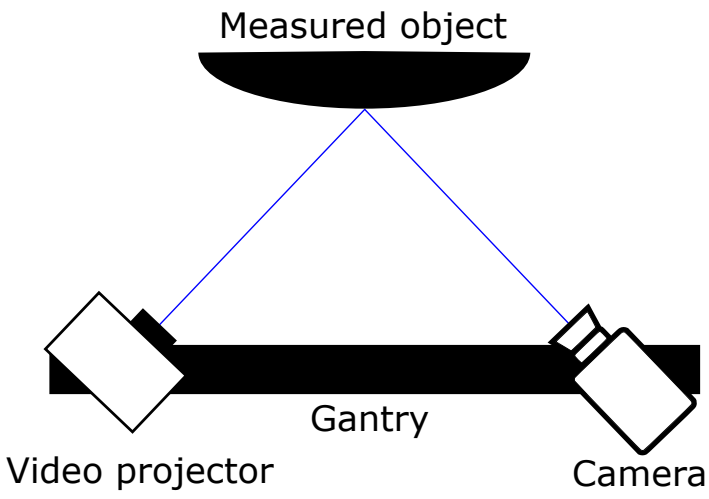

Figure 2.4 Diagram of a single camera 3D scanner

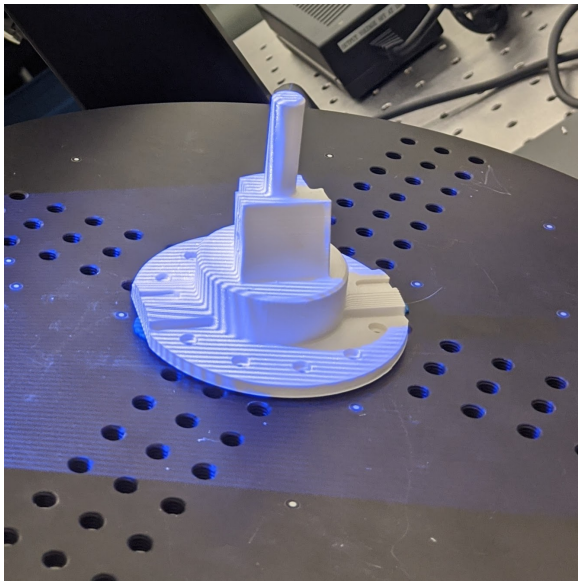

Figure 2.5 The structured light pattern projected on a 3D printed part.

2.2.2 Standard and Methods of Evaluation 3D scanners' Accuracy

The Association of German Engineers (Verein Deutscher Ingenieure, VDI) published in 2008 the VDI/VDE 2634 part 2, which determines the methods to rate the uncertainty of a 3D scanning system, and part 3, which applies to systems that generate multiple views by moving the 3D scanner or the scanned object [43]. To further develop an understanding of the metrological capabilities of 3D scanning systems, Ghandali et al. developed a methodology to characterize the measurement errors of a commercial 3D scanner concerning the position of the measured object in the measuring space [44]. Isa et al. developed a volumetric error mapping to correct errors in photogrammetric metrology, determining that the measurement error magnitude could be reduced by 10 to 30% [45]. Dicking et al. devised a methodology of directly comparing measurements of a Coordinate Measuring Machine (CMM) and a structured light 3D scanner. This comparison can allow the user to craft a compensation methodology for their machine [46]. Cuesta et al. produced a GD&T-feature-based artifact accompanied by a unified calibration methodology to respond to the ever-growing number of systems and solutions to structured light 3D scanning [47]. Gayton et al. provide a parametric uncertainty evaluation methodology, which offers the user more information about the capacity of their 3D scanning systems. Zhao et al. implemented an uncertainty evaluation for profile measurements for an industrial-grade 3D scanner to determine the quality of its measurements [48].

2.2.3 Applications of 3D Scanning in Manufacturing and Inspection

Researchers see opportunities in using structured light 3D scanning in metrology thanks to its high density of measurements. Indeed, the automotive [49], medical [50], and dental [51] fields are all in the process of adopting structured light 3D scanners as part of their process. For applications where accuracy is of higher importance, like in aerospace, 3D scanning is in development [52], and more advanced measurement methodologies are being currently under development to improve their accuracy [53].

2.3 Machine Learning

The proliferation of machine learning applications across domains such as healthcare, finance, natural language processing, computer vision, robotics, and recommendation systems underscores its transformative impact on society. It has revolutionized how we analyze data and make decisions. Not long after Donald Hebb introduced the biological model for the neuron in 1947 [54], Frank Rosenblatt developed a working artificial neuron, named the perceptron, that could recognize shapes and images. Still, it did not meet the author's expectation [55]. At that time, the neurons' weights in the neural network were set manually by the Artificial Neural Network's (ANN) designer, requiring expert knowledge of the ANN's architecture and the subject the ANN was designed to work on. It was a stumbling block in the road of perceptrons. A network performing complex computations requires nonlinear components that aren't solely reliant on the input data. However, when such a network produces incorrect results, pinpointing the specific connection strength responsible for the error becomes a formidable challenge due to the multitude of interconnected elements [56]. Backpropagation, developed by Rumelhart et al., is a learning procedure that can correct the errors of an ANN by propagating that error to each neuron of the network and applying a modification to the weight using gradient descent. It was shown to be able to effectively tweak the weight parameters of an ANN to enable it to generalize and capture underlying patterns in the training data autonomously, solving the stumbling block and fueling the first neural network renaissance [57].

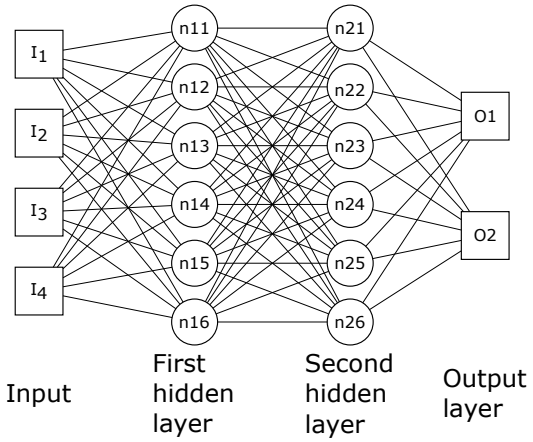

Figure 2.6 Diagram of a three-layer Multilayer Perceptron

Figure 2.6 illustrates the architecture of a basic three-layer Multi-Layer Perceptron (MLP). This model showcases input data flow through successive layers of computation, ultimately culminating in the output layer. The hidden layers depicted in the diagram serve as an intermediary stage where transformations occur, hidden from direct observation by users or external algorithms. Each neuron within the first layer, denoted as n_{1u} and u is the index of the neuron in the first layer, transforms the input values, represented by I_i where i is the input index according to equation 2.1. An additional bias parameter B can also be included to introduce further flexibility and adaptability in the neural network's learning process.

$$n_{1u} = B + \sum_{i=1}^{k} (w_{1u,i} \times I_i) \tag{2.1}$$

After the first layer is fully computed, the result of each neuron is passed to the neurons of the second layer n_{2v} where v is the index of each neuron in the second layer, multiplying them by the corresponding weight $w_{2v,1u}$ and adding the optional bias parameter. This process persists iteratively until reaching the final layer, which also comprises neurons. At this stage, the output treatment varies depending on the model's purpose. For instance, when tackling regression challenges, the output typically remains unchanged. In this scenario, the final layer directly produces the predicted values without further manipulation. Conversely, in classification tasks, the output of the last layer undergoes a transformation through a softmax function. This operation yields a probabilistic interpretation, indicating the likelihood of the input belonging to different classes, such as Class A or B. The softmax equation is represented in equation 2.2 where z is the input vector, e^{z_i} is the standard exponential of the input z_i and k is the number of classes.

$$\sigma(z)_i = \frac{e^{z_i}}{\sum_{j=1}^{K} e^{z_j}} \tag{2.2}$$

2.3.1 Convolutional Neural Networks

Most DNNs working on images aim to analyze and classify them to determine their content. For this task, Convolutional Neural Networks (CNNs) were found to be very powerful. CNNs use a learnable filter to extract hierarchical patterns from input data automatically; see figure 2.7. LeCun et al. developed the LeNEt-5 using only seven layers, two convolutions, two pools, one fully connected, the input, and the output to classify handwritten digits into their values. The authors claimed an error rate of 0.95% after only ten epochs on the MNIST dataset. In contrast, the best other algorithms could claim an error rate of 1% while being approximately 60% more computationally expensive [58].

Various CNN advancements have been developed to enhance their performance across diverse image datasets. For instance, AlexNet, introduced in 2012, builds upon the foundational architecture of LeNet while incorporating contemporary innovations [59]. It integrates Rectified Linear Units (ReLU) as a non-linear activation function after convolutional layers, enabling the network to capture intricate non-linear patterns and relationships within the data [60]. Furthermore, Dropout between fully connected layers is a regularization technique to mitigate overfitting and prevent the co-adaptation of neurons, thereby enhancing the model's generalization capability [61]. These enhancements contribute to the improved performance and robustness of AlexNet across a wide range of image recognition tasks, obtaining an error rate of 15.3% on the Fall 2011 ImageNet dataset, while the following best algorithm achieved an error rate of 26.2%.

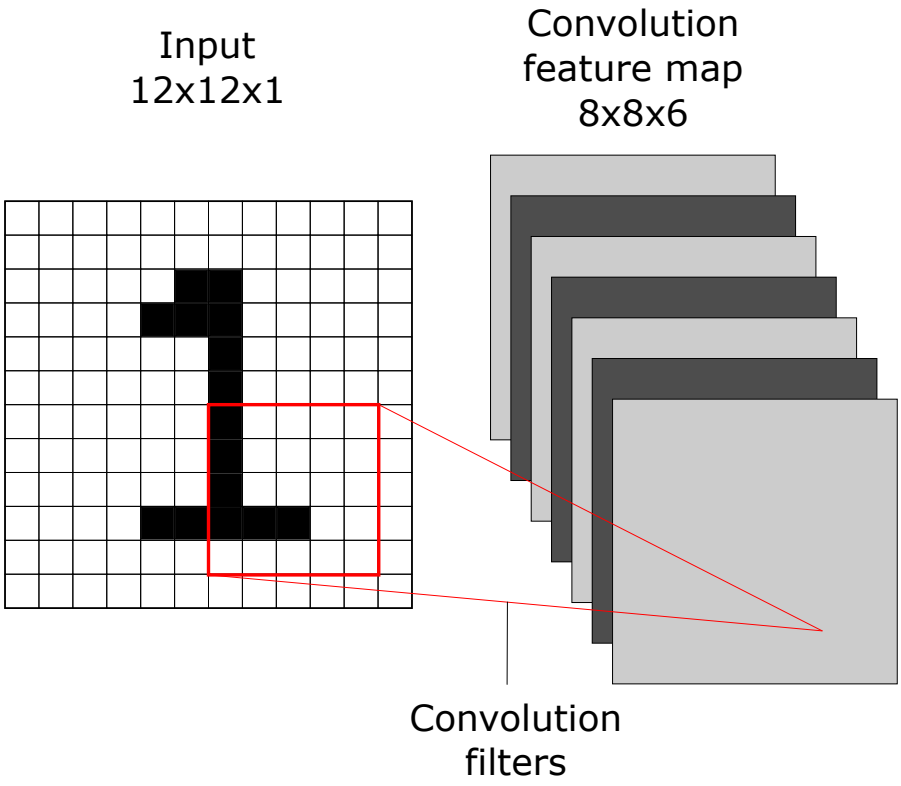

Figure 2.7 Diagram of a Convolutional Layer.

Visual Geometry Group Network (VGGNet) is a CNN architecture investigating the effect of increasing a network's depth using tiny convolution filters. Indeed, VGGNet is designed with 16 to 19 weight layers, more than double the 8-layer deep AlexNet. The authors note that the configuration of their proposed CNN is quite different from other CNNs that use a large receptive field for the first convolution layers (11×11 convolutions with stride 4 in AlexNet). Instead, they use a series of 3×3 convolutions with stride one and a rectification layer between each convolution layer. In effect, replacing a 7×7 convolution layer with three 3 convolutions, both having the same receptive field, but the first needs 81% more parameters for its weights, and the second has the added benefits of having integrated non-linearity [62]. The authors claim a top-5 error in the validation set of 7.1%, meaning the proper image classification is within the top 5 predicted classifications from the network. GoogLeNet is another deep CNN architecture with 22 convolution layers. Szegedy et al. utilized small convolution filters (1×1, 3×3, 5×5) in inception modules, which are the main building blocks of the network. The inception modules transform the data from the previous layer through different convolution filters and rectification layers in parallel before concatenating and passing it to the next layer. The authors note that the impressive network depth might have prevented the gradients from effectively propagating through all the layers, so they

implemented auxiliary classifiers. Adding them at strategic positions in the network could ensure a strong gradient could be backpropagated through the middle part of the network, circumnavigating the vanishing gradient problem [63]. The top-5 accuracy reported by the authors is 7.9%.

He et al. continued making CNNs deeper by demonstrating the Residual Network (ResNet): a CNN architecture that can be built with 18 to an astonishing 152 convolution layers. The residual learning blocks, shown in figure 2.8, were designed to enable the construction of deeper networks by solving the vanishing gradient problem in a novel way. The framework presented by the authors allows for the input to a residual learning block to be passed to the next layer by performing identity mapping and adding them to the output of the residual learning block. This block comprises stacked convolution with ReLu layers of size 3×3. This simple layout is surprisingly powerful, resulting in a top-5 error rate ranging between 5.71% for ResNet-34 to 4.49% for ResNet-152, all with lower complexity than VGGNet-19 [64].

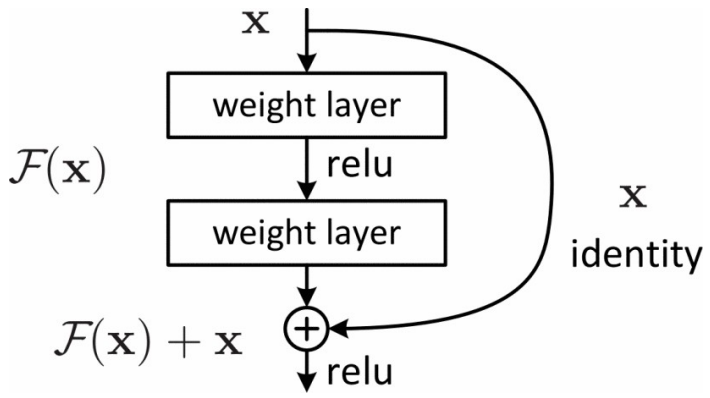

Figure 2.8 The ResNet basic building block [He et al. 2015]. ©2016 IEEE

2.3.2 Machine Learning for 3D shapes

Both DNNs and classical machine learning tools work well for structured and organized datasets by taking advantage of the inherent information in the distribution of data in the input. One example is the convolutional layers in CNNs that learn to detect what digit is in an image by finding loops or straight lines by analyzing the values in discrete pixels. In the domain of 3D shapes, where discrete data representation is not common, DNN implementations are rare. Some implementations used images, or views, of the 3D object and classified them to inform on the subject of the 3D model [65,66]. Wu et al. demonstrate their algorithm for a deep representation of volumetric shapes that could allow for the classification of 2,5D depth measurements of objects. In this implementation, it is necessary to voxelize the 3D

shape, enabling 3D convolutional layers and the previously mentioned tools and optimization already developed for image classification [67, 68].

Qi et al. later developed PointNet, which could work directly on an unorganized and unstructured point cloud to apply classification or segmentation and offered results that could compete with or even beat 2D representations of the 3D model [69]. The authors identify three properties that their networks will need to account for. The first property is the lack of order in the set of points, and an NN consuming a point cloud of N points needs to be invariant to the N! possible permutation of the point sequence. The second property is the importance of the position of each point compared to other points. The subset of points neighboring each point is significant to conclusions made on it. The third property of point clouds is the invariance under transformations. Depending on how they were created, point clouds might have no relationship with the coordinate system they are currently under and always represent the same object, regardless of the orientation in the 3D space. The authors integrate modules in PointNet's architecture to solve these issues: a symmetry function for the unordered input and a joint alignment network to ensure the network is not affected by rigid transformations of the input point cloud. The segmentation network learns the second property to determine what group a particular point belongs to. On the ModelNet40 shape dataset, PointNet claims an average class accuracy of 86.2% and an overall accuracy of 89.2% in point cloud classification tasks and 83.7% mean interaction over union (mIoU), which is competitive with or beats other NNs using images or voxel representations of a 3D shape. The successor algorithm, PointNet++, improved upon its predecessor by implementing, amongst other things, a nested partitioning of the input point cloud [70]. A hierarchical structure abstracts local regions of the point cloud using three layers: the sampling layer, the grouping layer, and the PointNet layer. The abstracted point set can then be fed to a classification MLP or a segmentation network. Thanks to the sampling layers, PointNet++ is also robust in the case of non-uniformly sampled point clouds. It claims an overall accuracy of 91.9% on the classification of the ModelNet40 dataset, improving upon its predecessor and other classification methods.

Following these seminal works, many other methodologies have been published, improving upon their predecessor in the classification and segmentation of the ModelNet40 dataset. Namely, Kd-Net [71], O-CNN [72], SO-Net [73], MeshNet [74], PointGPT [75], ShapeLLM [76], and the current record holder (overall accuracy of 96.9%) GeomGCNN [77]

2.4 3D Printing Geometric Accuracy Improvement Methods

Initially, 3D printing was conceived as an RP platform, where the printed parts only needed to be accurate enough to represent the geometry of the intended design. The attention to geometric accuracy was documented in chapter 2.1.3. This section will delve into methodologies that various researchers have implemented to actively affect the printing process and improve the accuracy of the produced part. We will not limit the section's scope to a single printing process to enable intersectionalism and facilitate a comprehensive understanding of methodologies across various 3D printing techniques. These methodologies can be categorized into several groups:

1. Dynamic Process Parameter Adjustments: Methods that measure actual process parameters to form a closed-loop control system, allowing real-time adjustments during the printing process to optimize accuracy and quality based on feedback from sensors or monitoring devices.
2. Predictive Geometric Compensation: Methods that use physics-based analyses to determine the deviations created by the printing process, allowing adjustments to be made in advance to compensate for anticipated deviations and improve geometric accuracy.
3. Retrospective Error Analysis: Methods that use fabricated parts and their measured deviation fields to build a deviation model for the following parts.

While the goal of each method group is the same, ensuring the printing process results in a part with as little deviation from the intended geometry as possible, the hypothetical source of errors for each is different. The first points to fluctuations in printing parameters as the source of errors, the second highlights the thermo-mechanical effects of the printing process on the solidified material, and the third encompasses machine errors occurring during the printing process in addition to the thermo-mechanical effects. An ideal methodology for improving the geometric accuracy of a printed part would require an element from each group, but as researchers focus on a method in their published work, so will the following sections.

2.4.1 Dynamic Process Parameter Adjustments

In 3D printing processes, some process parameters are controlled in a closed loop to ensure precise and consistent parts fabrication. In FFF, for example, the nozzle hotend and the print-bed temperature are closely monitored and adjusted via Proportional Integral Derivate

(PID) controllers [78] to ensure the flow of material is consistent and solidifies as is prescribed. If the nozzle hotend temperature was too low, insufficient material could be extruded, and the part could be in under-material conditions, failing to reach the intended geometrical accuracy. In this example, the error source is the low temperature of the extruder, and the effect is under-extrusion of material. The same effect can also arise from factors such as a smaller filament diameter, nozzle clogging due to impurities, or excessively high printing speeds where the material has insufficient time to soften. In these cases, the hotend temperature cannot verify if the printing is under-extruding material. To better control the 3D printing process, researchers have considered many process parameters to evaluate the quality of the process itself and, when possible, adjust controllable parameters to improve it. It is worth noting that these methods do not necessarily attempt to control the geometric accuracy of the 3D printed part in particular but instead strive to stabilize the process. This stability will indirectly improve the final printed part's geometric accuracy by eliminating instabilities often described as random errors, like blobs or over/under-extrusion.

Acoustic emission sensors installed in 3D printers can detect different modes of operation due to their sensitivity to mechanical system dynamics. This sensitivity allows the sensor to detect friction, force, or vibration variations. Researchers have implemented algorithms to parse the acoustic emission signal to monitor the status of the printing process [79–82]. Shevchik et al. also implemented acoustic emission sensors to monitor the quality of a Selective Laser Melting (SLM) process. The acoustic signals from the sensors are analyzed by spectral convolutional neural networks, which were able to ascertain the porosity of the fabricated part with an accuracy of 83 to 89% [83]. Wu et al. studied monitoring and diagnostic methods based on acoustic emission sensors to detect different failure modes of FFF 3D printing. By training a Self-Organizing Map, an unsupervised machine learning model, on the signal of failing and successful printing processes, it could later detect that a print had failed and determine the root cause of the failure. The authors' proposed method is limited to first-layer monitoring and diagnosis, the most critical step in an FFF 3D printing process [79]. Li et al. investigate a similar approach: using piezoelectric vibration sensors to monitor the extrusion quality in an FFF 3D printing process. By detecting the vibrations caused by the extruder stepper motor in a regular and abnormal state, the authors can determine the production quality and the machine state of the extruder stepper motor at more than 90% accuracy [84] To date, there is a notable absence of literature exploring the integration of acoustic emission sensing within a closed-loop system to enhance the efficacy or accuracy of the 3D printing process.

Infrared Imaging systems have also been used with FFF 3D printers to characterize the melt pool characteristics, providing insights into the nature of the inter-layer bond. Seppala and

Nigler implemented a method to determine the quality of the weld between layers and how the high-temperature nozzle and newly deposited material affected the temperature of the already solidified material. The authors conclude that a small amount of heat is transferred to the last solidified layer, and the layer before that doesn't see its temperature rise above the glass transition temperature, meaning the weld is never annealed in the printing process. To accomplish this, a temperature compensation algorithm to eliminate the reflection of the nozzle hotend on the 3D printed surface was also developed by the authors [85]. In the powder-based laser processes, the energy density of the laser is one of the most critical process parameters that can be controlled, either by changing the power available to the laser or by moving it faster across the surface of the powder bed [86]. A robust process control methodology was required to obtain repeatable and reliable results. Bi et al. propose such a process control methodology by implementing a PID-controlled system based on the infrared temperature measured on the melt pool. This approach improved the laser's capability to build thin-walled structures and ensured a constant melt pool size, which in turn enabled constant cooling and resulting homogeneous microstructures [87]. Kousiatza and Karalekas investigated the in-situ use of Fiber Bragg Grating sensors to monitor the temperature profile and strain in the manufacturing process. This data allows the author to determine the post-fabrication residual strain in the free-standing state [88].

Another avenue for error detection in printing is vision-based methodologies, which leverage cameras or imaging systems to capture and analyze real-time data during printing. The imaging system can comprise a single source of data or an array of cameras to view the fabricated part from all sides. Vision-based process control methodologies are often paired with an ML algorithm that interprets the received images and outputs a conclusion on the quality of the printing process. The ML algorithm used in vision-based process control methodologies leverages the vast amount of research in computer vision for robots and other industrial processes, showing signs of a relatively mature process compared to different types of in-situ process control in AM.

Gardner et al. present a method for optimizing the printing parameters in response to faults detected by cameras and interpreted by the AlexNet CNN. By using transfer learning, a process where the model is trained initially on generic and large dataset [89] like ImageNet [90] and then fine-tuned on a smaller particular dataset concerning the subject, the authors were able to detect the presence of blobs, delaminations or warpings on the surface of the printed part, see figure 2.9. The printing process parameters are then adjusted to improve the geometric quality of the fabricated part. The defect detection module achieved an inference accuracy of 66% to 89% on the nature of the defect, and the quality optimization shows a 14% augmentation in the number of "No defect" labels when compared to the average part [91].

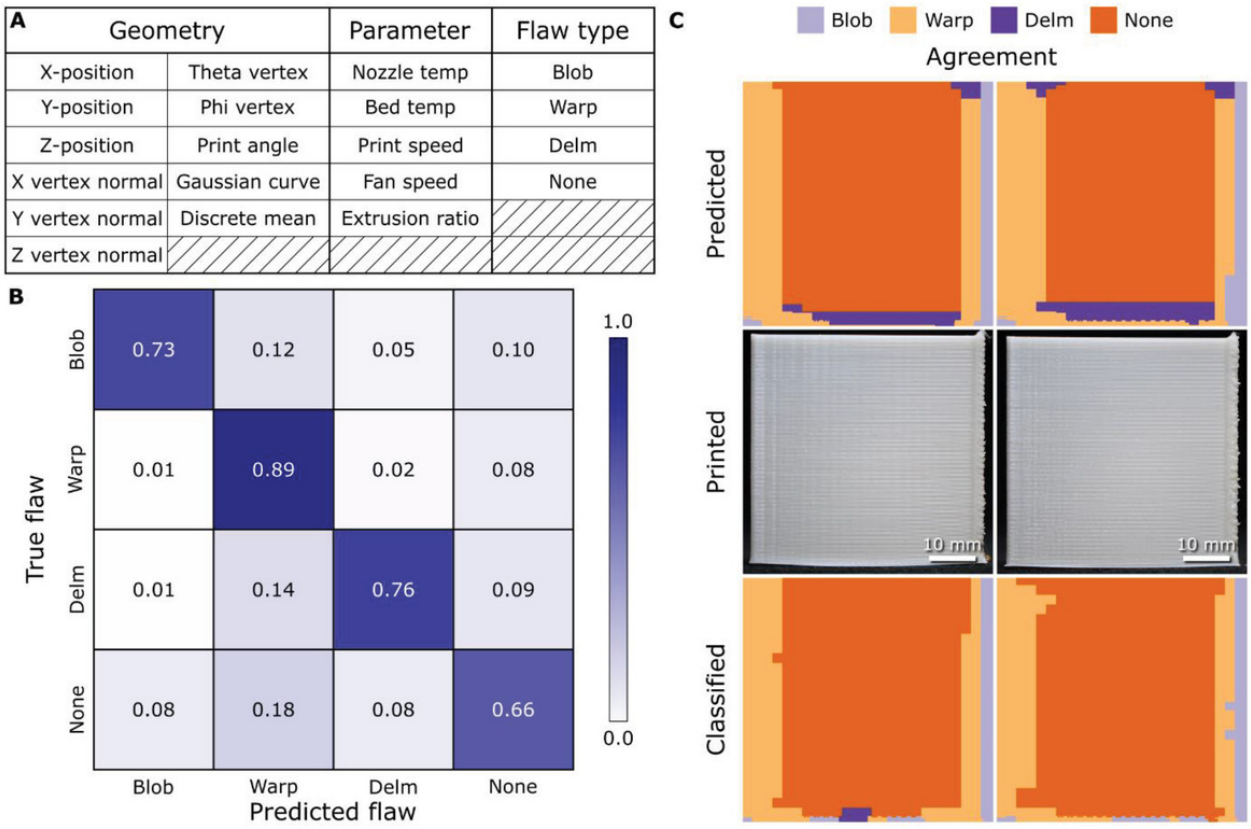

Figure 2.9 A) The CNN uses the inputs and outputs to infer defect classification. B) Confusion matrix of the trained CNN. C) Comparison of the inferred and actual classification of a printed part [Gardner et al. 2019].

Liu et al. present an image analysis-based methodology to enhance the quality of the printing process's infill component. Their approach involves the installation of two digital microscopes positioned closely to the printing nozzle, enabling the assessment of extrusion quality by analyzing the texture of captured images. A gray-level co-occurrence matrix [92] is used to interpret the image data, and a K-Nearest Neighbor algorithm [93] is then used to classify the obtained images to finally conclude what modification to the printing process should be applied [94]. Jin et al. propose a similar methodology using the ResNet-50 CNN with transfer learning as the image classifier to detect under-extrusion, over-extrusion, or standard extrusion. The print speed, the material flow rate, and the layer height are then adjusted to compensate for the extrusion to improve the quality of the printed part [95].

Brion and Pattinson developed the methodology by implementing a regression-type neural network model to accurately predict the actual material flow rate based on images of the material as it exits the nozzle. This value can then compensate for the flow rate of subsequently deposited material by modifying the on-the-fly flow rate modifier of the machine [96]. Brion

and Pattinson later generalized this application to other printing parameters: the material flow rate, the lateral machine speed, the machine z-offset, and the hot end temperature. To achieve this generalization, the authors used a multi-head neural network, a neural network with multiple output layers and multiple objectives [97], see figure 2.10. By classifying the image related to the printing parameters, a compensation algorithm can adjust the parameter to ensure the quality of the printed part [98].

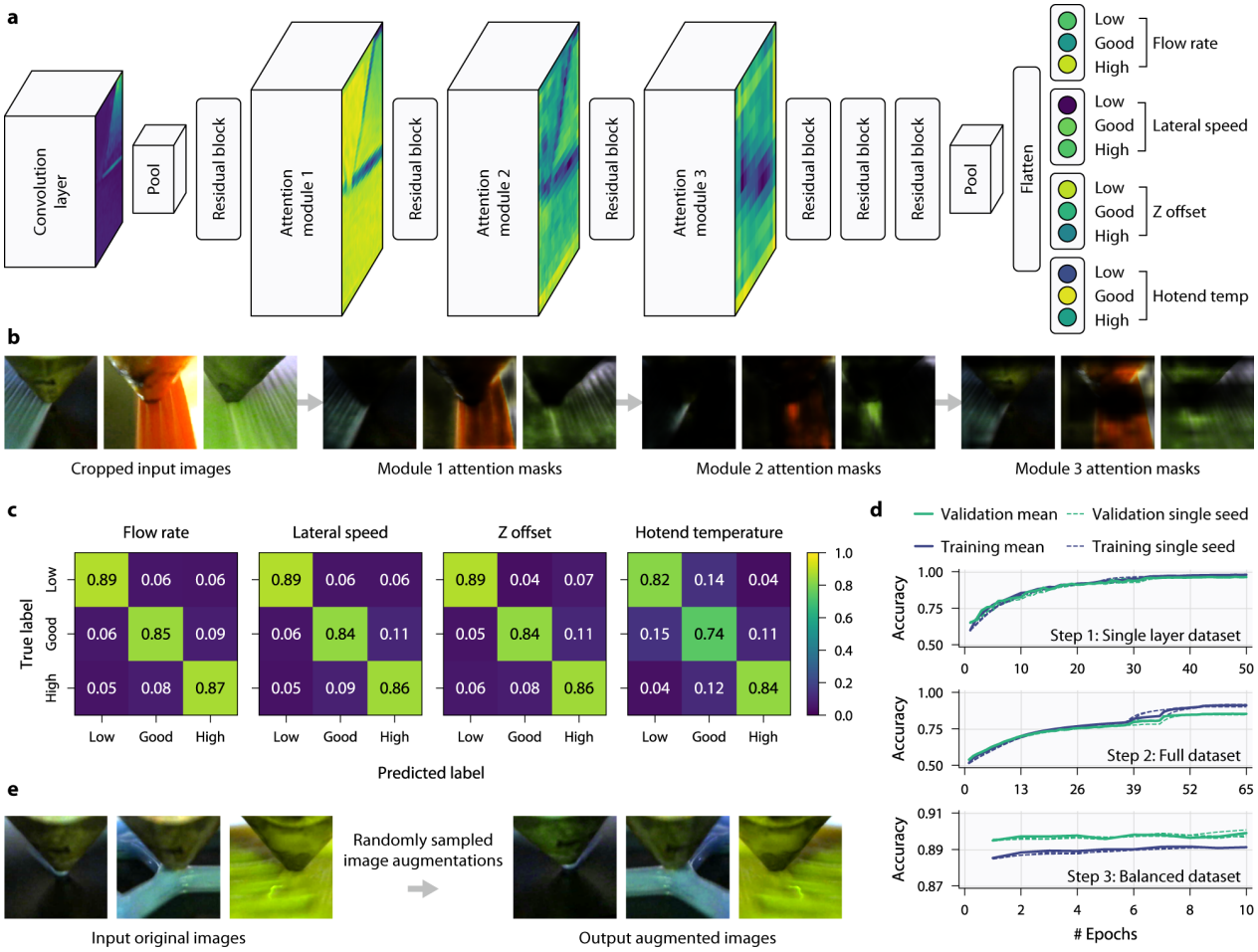

Figure 2.10 a) The proposed multi-head Neural Network architecture by Brion and Pattinson. b) The different attention masks for each head. c) Confusion Matrices of the final matrices after each tr ining. d) Training and validation accuracy plots from the training and validation sets [Brion and Pattinson, 2022].

2.4.2 Predictive Geometric Compensation

Many researchers have also investigated the approach of predicting the deviations attributable to the printing process. These approaches are characterized by being applied before the print-

ing process, enabling the user to compensate the printing process and improve the geometric accuracy of the printed part. A significant appeal of this approach is the possibility of testing and developing the optimal geometry and compensation methodology in simulations and experiments without requiring machine time or wanted material, freeing them for continued production. Sartori and Zhang present some conditions for compensation of machine errors to be successful [99], which will be applicable for this section and the next:

- The magnitude of systematic error components must significantly surpass that of random errors, i.e., the machine must be repeatable.
- Adequate error modeling is essential; treating measurement errors as machine errors can distort compensation efforts.
- Error assessment and compensation should align with the machine's absolute coordinate system.
- High-frequency errors, like the stairway effect in 3D printing, may remain uncompensated due to mechanical limitations.
- Real-time compensation procedures should not compromise machine performance.

One approach to predicting immutable deviations of the 3D printing process is to simulate that process using Finite Element Analysis (FEA), as presented by Chowdhury et al. Indeed, the authors use FEA to predict the thermo-mechanical deviations in metallic powder 3D printing. An NN is then trained on the output of the FEA to predict the deviations for the points representing the nominal CAD STL, which can then be used to compensate them by the inverse of the expected deviations [100, 101]. Zhu et al. showcase an approach where FEA-simulated data form the dataset for a statistical error model. This error model combines Statistical Shape Analysis with a Gaussian Process to model deviations while considering process parameters. This method can then predict the 3D printed part geometric deviation of a part with new process parameters, which can enable the designer to determine what are the best tolerances that can be reached with a given shape and process parameter [102]. Another study by Zhu et al. proposes using CNNs to learn deviation patterns based on the outline of the geometry and some process parameters. The input, CNN, and predicted output are presented in figure 2.11. It was trained using data created with FEA to simulate the thermomechanical deviations caused by the printing process [103].

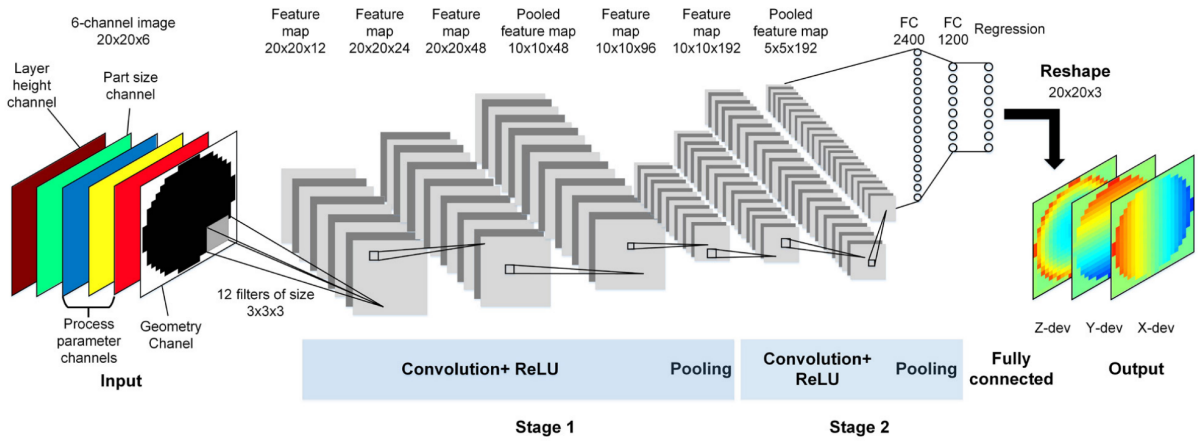

Figure 2.11 The Convolutional Neural Network for Geometric Deviation Prediction [Zhu et al, 2020]

Charalampous et al. propose a learning method in which a regression-based machine learning model is trained to predict deviation on primitive shapes concerning process parameters. The model can infer scaling errors from the process parameter by training on a set of printed cubes and evaluating them on different axes. It allows the trained model to determine the inverse scaling necessary to eliminate, by compensation, the deviations of the more complex 3D printed part [104].

2.4.3 Retrospective Error Analysis

Other researchers have opted to analyze the deviations of a printed part to determine the 3D printer's deviation model. The computed deviation model then includes all deviations from the 3D printer, including kinematic errors, thermo-mechanical deviations, deviations caused by environmental changes, etc. In this situation, most research focuses on methods to interpret the deviation fields into models that can predict the deviations based on selected input parameters.

One approach to determining the deviations of a printed part is to analyze the printing process itself and create a mathematical model of the deviations that can then be applied to other geometries. Tong et al. present a parametric error modeling based on a master reference artifact fabricated using an SLA 3D printer and measured using a CMM. The measurements then estimate the error function coefficients using Legendre polynomials. The error model can be simplified to 2D by assuming $z = 0$ and using a plate with holes as the reference artifact. The authors then apply the inverse of the predicted error to the STL file to produce a compensated hole plate, which shows reduced errors in all measured

parameters [105]. Caja et al. propose a similar parametric error modeling in 3 dimensions to capture 18 independent error functions defined by Legendre polynomials to characterize the kinematic model of a PolyJet 3D printer by fabricating an artifact that can be measured in a CMM. After building that kinematic error model, the authors apply the inverse of the predicted systematic errors to the STL of the nominal CAD file and obtain a part with 70% reduced max deviation [106, 107].

Cheng et al. propose a method for modeling the dimensional error of the 3D-printed part using a parameter-based transfer learning approach. The shape deviation is separated into a shape-independent and a shape-specific error model. The first can be described by a statistical model involving expert knowledge and statistical analysis of datasets, while the second requires specific investigation. This method allows for a level of generalization that identifies a part of the systematic deviations caused by a 3D printer [108].

Song et al. address the issue of low dimensional accuracy in low-end FDM 3D printers by implementing an error modeling approach using the Kriging method [109]. This error model includes deviations due to mechanical error and thermo-mechanical effect while focused on in-plane deviations, which corresponds well with the 3D printing process [110]. Huang et al. built a unified modeling approach on the previous study for cylinders and polygon shapes built using 3D pr nters. This approach uses a polar coordinate system to ensure the correlation between the reference geometry and the measured data and simplifies the mathematical definition of the error model $f(r, \theta)$. In the case of cylinders, they have a constant radius r, meaning the in-plane deviations vary only with respect to the angle $heta$. In the case of polygons, the authors relate the r coordinate to the angle θ using a square cookie-cutter function $sign[cos(n(\theta - \phi_0)/2)]$ to obtain equation 2.3, which establishes the deviation of any polygon to its angle $theta$ and the computed radius $r_0(\theta)$. In this method, β_0, β_1, β_2, and β_3 are parameters that require fitting using the Least Square Estimation, ϕ is a phase variable determined by the used polygon and its orientation, and ϵ is the parameter including all non-modeled geometric deviations and random measurement errors.

$$f(\theta, r_0(\theta)) = \beta_0 + \beta_1 cos(2\theta) + \beta_2 sign[cos(n(\theta - \phi_0)/2)] + \beta_3 cos(n\theta) + \epsilon \tag{2.3}$$

This equation showed promise in modeling the in-plane deviations of squares fairly well but struggled with pentagons and dode agons. The model was able to fit the pentagons better but still failed to fit the dodecagon when using an alternative cookie-cutter function [111, 112]. Huang et al. later propose an optimal compensation methodology based on a previously determined deviation model. The authors affirm that negating the measured or computed deviation at a particular position is not optimal unless the deviation is uniform across the

surface of the 3D printed part. In reality, the compensation needs to follow equation 2.4, where $x^*(\theta)$ is the optimal compensation amount, $g(\theta, r_0(\theta))$ is the deviation model presented by Huang et al. and $g'(\theta, r_0(\theta)$ its derivative. By applying this compensation methodology to a 1" cylinder printed using an SLA 3D printer, the mean error was reduced from -5×10^-3 to 9×10^-4, and the standard deviation of the error was reduced from 4×10^-3 to 4×10^-4 [113].

$$x^*(\theta) = \frac{g(\theta, r_0(\theta))}{1 + g'(\theta, r_0(\theta)} \tag{2.4}$$

Luan and Huang then propose a new method to compute the deviation model for freeform 2D shapes, utilizing Circular Approximation with Selective Cornering (CASC) instead of the previously presented method, which used Polygon Approximation with Local Compensation (PALC). This new method to approximate in-plane deviations of a freeform 2D shape is generalized and can be applied from cylinders to freeform shapes. It could also predict deviations of new shapes using a limited number of tested shapes. The authors also determine the optimal compensation and apply it to obtain a reduction of 40% and 49% of the absolute average deviation of a convex and a concave shape [114]. Cheng et al. propose a schema to model the deviations of an FFF 3D-printed part using the mathematical definition of the shape and a printer process parameter as input. Indeed, the authors affirm that the effect of process parameters on the geometrical accuracy of printed parts is usually non-linear and non-uniform in different parts of the geometry and propose using Gaussian Process Kernel Smoothing (GPKS). A compensation model is also proposed and compared to the other methods presented in the literature to demonstrate that their method's performance was on par or better than the other proposed methods [115].

The Shape Deviation Generator is a convolution framework presented by Huang et al. to integrate the layer-by-layer fabrication mode typical of 3D printers to build a deviation model adapted for 3D shapes. Indeed, as layers are deposited onto previous layers, they heat and cool each other, causing shrinkage and dilatation that depend on the geometry of the last and current layers. This convolution framework should also facilitate learning and prediction of 3D printing accuracy by enabling machine learning for AM. For example, the authors propose a dome approximated by a series of cylinders, or disks, with heights equal to the printer's layer height and varying radii. The deviation model $f(x)$ of each disk is known via equation 2.3 presented in a previous study, and interlayer interactions are determined by identifying and learning a transfer function $g(x)$ presented in equation 2.5. In that equation, $y(x)$ is the shape deviation, x is the parameter describing the shape deviation, and ϵ is the model error term [116].

$$y(x) = (f * g)(x) + \epsilon \tag{2.5}$$

Jin et al. propose a prescriptive approach to predict out-of-plane deviations, not perpendicular to the build direction, in SLA 3D printed parts. The authors first determine that while in-plane deviations exhibit repeatable patterns of deviations for cylinders of various radii, out-of-plane deviations vary with part size. By utilizing the equivalence of effect approach proposed by Wang and Huang, which states that multiple factors have the potential to produce identical results [117], the authors present a new deviation model to account for the complicated interlayer interactions and the accumulation of errors that are proportional to the size of the part and hence the number of layers required to build the part. The authors also create a compensation model and demonstrate a reduction of 58% for a vertical irregular polygonal and 37% for a vertical freeform shape [118].

Afazov et al. propose another method to improve the geometric accuracy of 3D printed parts using the deviation data directly to update the coordinates of the reference surface mesh. By measuring the 3D printed part using a structured light 3D scanner, the authors can obtain a high-density point cloud of the deviated printed part. Using a signed point-to-plane distance metric, they compute the deviation vector field between the reference surface mesh and the scanned data surface mesh. To do so, they determine to which triangle $\triangle ABC$, from the scanned surface mesh point, point P, from the reference surface mesh, relates to and find the closest point O inside triangle $\triangle ABC$, see figure 2.12. The distance d_α represents the deviation, and applying the same deviation to the reference point P will output a compensated point P'. The authors experimentally demonstrate that approximately 75% of deviations on a generic shape can be eliminated and that the process can be repeated to improve the final result [119].

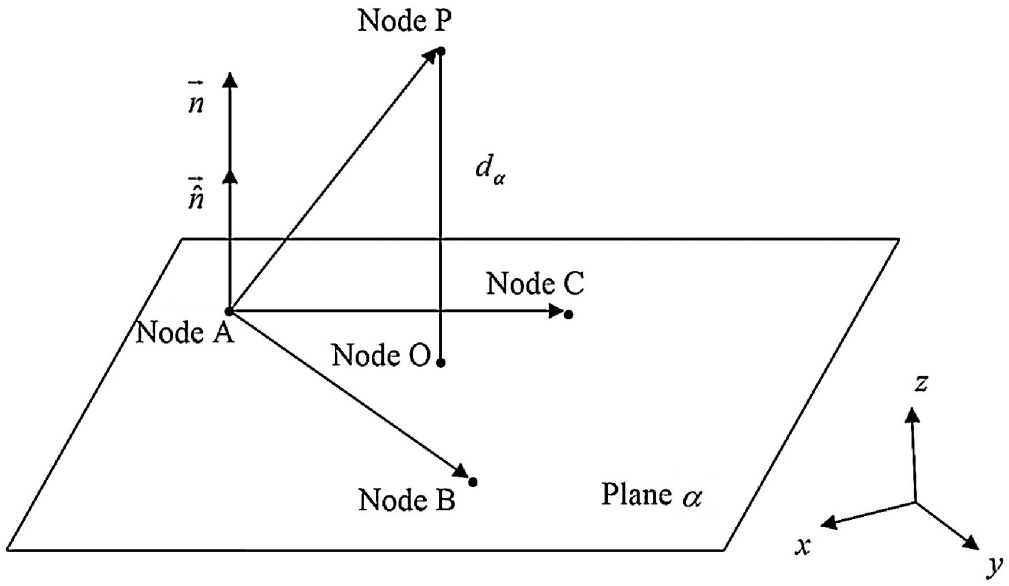

Figure 2.12 Schematic description of the compensation process proposed by Afazov et al. [Afazov et al., 2017]

Decker et al. present a methodology for predicting deviations on FFF 3D printed parts using a random forest method based on the triangular mesh shape data. This supervised ensemble machine learning method uses several regression trees to output the mean prediction of the individual trees. The authors claim that the benefit of using the random forest is that inputting dissimilar data, as in the triangular mesh coordinates of different shapes, can be accommodated by individual trees and ensure the model is generalizable. In training, the authors try different numbers of trees in the ensemble and determine the optimal number of trees in terms of performance. The result of the compensation based on the inverse of the predicted deviations is a 50% reduction in the Root Mean Square of the vertex error for a shape the model has not trained on [120].

Zhao et al. introduce a neural network-based methodology to predict deviations based on the point cloud of the nominal geometry. This methodology uses 3 set abstraction levels and three interpolation layers before an MLP, shown in figure 2.13 to determine the deviation for each point in the point cloud. This deviation is then added to the nominal point cloud coordinates to form the predicted deviation point cloud. The average error of the trained model is 0.037 mm for the test dataset [121].

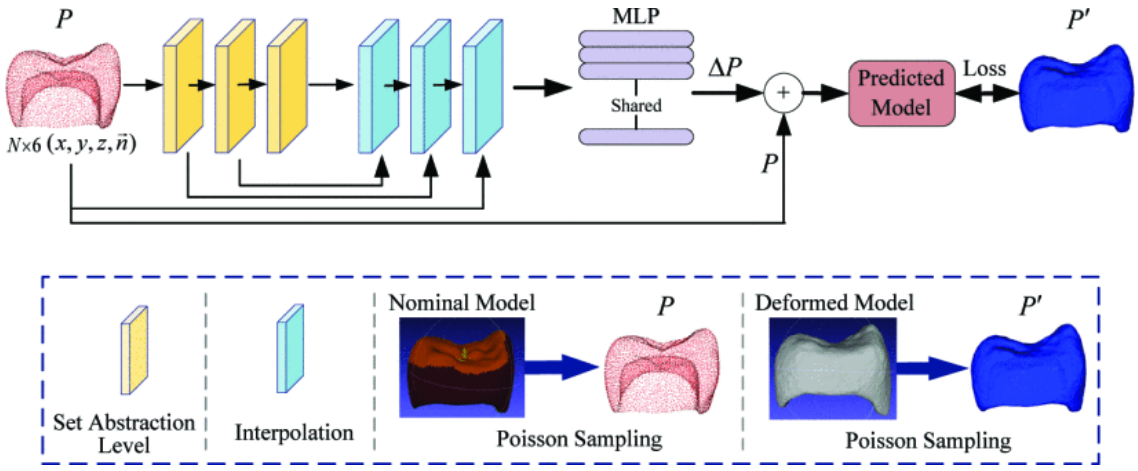

Figure 2.13 The architecture of the proposed neural network in Zhao et al. [Zhao et al., 2022]. ©2022 IEEE

Wang et al. put forward a formalized mathematical decomposition of the fabrication of non-smooth 3D printed parts into two steps. First, additively build the smooth base shapes, i.e., domes or cylinders, then subtractively remove extra material to obtain the non-smooth edges and corners. The general formulation of such a model is shown in equation 2.6, where y is the predicted deviation, x_i are location-dependent covariates, p_j are the process parameters covariates and s_j represent the shape-dependent covariates. The mean pattern of the shape deviation is represented by μ, η is a zero-mean random field capturing the spatial correlation, and ϵ is the measurement error.

$$y(x_i, s_j, p_j) = \mu(x_i, s_j, p_j) + \eta(x_i, s_j, p_j) + \epsilon \tag{2.6}$$

The authors also demonstrate that the additive and subtractive steps are critical to accurately predict deviations of 3D geometry with sharp edges without first projecting them to 2D approximations. They also note that the geodesic distance between two points provides a better metric to determine the spatial correlation of two points on a surface mesh [122].

CHAPTER 3 OBJECTIVES AND RATIONALE

3.1 Objectives

This thesis presents a comprehensive investigation to develop a methodology to enhance the geometric accuracy of desktop FFF 3D printers. By harnessing the high-density and high-accuracy measurements obtained from structured light 3D scanners applied to actual 3D printed parts, we seek to refine our understanding of geometric discrepancies produced by desktop FFF 3D printers and ultimately improve the reliability of the printing process. To accomplish this objective, three sub-objectives were determined.

- Determine how to affect the 3D printing process with the goal of reducing geometric deviations based on 3D deviation values measured on the surface of the entire geometry.
- Determine how to interpret structured light 3D scan data in order to obtain the optimal deviation value that can be acted on.
- Create a model that can extract the optimal deviation values using as little data as possible.

The main objective, supported by sub-objectives, is propelled by two main opportunities. First, advancements in 3D scanning technology and a growing interest in utilizing 3D metrology for inspecting and qualifying manufactured parts. Model-based definition and inspection, often considered a necessary part of Industry 4.0, can fully leverage 3D scan data as a measurement input and create digital twins for all necessary simulations and evaluations. While the industry seems to be going further in using 3D scanning as a metrological tool, section 2.2 of the literature review shows the sparsity on best interpreting 3D scan data for particular applications.

Second, there have been many improvements in the quality and reliability of 3D printers and an increasing interest in employing these machines to fortify supply chains across various industries worldwide. Section 2.4 shows that very little work is available in the scientific literature on improving geometric accuracy in a closed loop form, or at the very least in an iterative improvement method. The few works that are available in this field either lack generalizability or interpretation of input data.

3.2 Research Questions and Hypothesis

Like a study's blueprint, the research design guides the entire process from data collection to analysis. It plays a pivotal role in ensuring that the research questions are addressed systematically and that the findings are valid and reliable. This study's main research question was how to improve the geometric accuracy of desktop-sized FFF 3D printers. Based on anecdotal knowledge, we know that compensating the nominal geometry by the inverse of measured deviations can improve the geometric accuracy of subsequent 3D printed parts. This poses a second question: How can we determine if measured deviations are a reliable source of information to determine the systematic component of the deviations caused by the 3D printing process?

To answer this question, a hypothesis is posed that will allow us to proceed with the research and hopefully demonstrate its validity. Assuming the printing process and the measurement of the part remain unchanged, the deviation field of any 3D printed part should comprise two components: one systematic and the other random. The systematic component is repeated in all 3D printed parts, and applying its inverse to the nominal geometry would eliminate it. Meanwhile, random errors are unpredictable and can only be reduced by improving the printing process. This hypothesis requires the 3D printing process to remain unchanged, meaning it is valid only for a single printer, a single set of printing parameters, and a single material. The Measurement of 3D printed parts should also be consistent, as the measurand should not introduce non-negligible noise in the measurement data.

CHAPTER 4 ARTICLE I: IMPROVING GEOMETRIC ACCURACY OF 3D PRINTED PARTS USING 3DMETROLOGY FEEDBACK AND MESH MORPHING

Authors Moustapha Jadayel, Farbod Khameneifar

Published in the Journal of Manufacturing and Materials Processing on November 29th 2020.

Abstract Additive manufacturing (AM), also known as 3D printing, has gained significant interest due to the freedom it offers in creating complex-shaped and highly customized parts with little lead time. However, a current challenge of AM is the lack of geometric accuracy of fabricated parts. To improve the geometric accuracy of 3D printed parts, this paper presents a three-dimensional geometric compensation method that allows for eliminating systematic deviations by morphing the original surface mesh model of the part by the inverse of the systematic deviations. These systematic deviations are measured by 3D scanning multiple sacrificial printed parts and computing an average deviation vector field throughout the model. We demonstrate the necessity to filter out the random deviations from the measurement data used for compensation. Case studies demonstrate that printing the compensated mesh model based on the average deviation of five sacrificial parts produces a part with deviations about three times smaller than measured on the uncompensated parts. The deviation values of this compensated part based on the average deviation vector field are less than half of the deviation values of the compensated part based on only one sacrificial part.

4.1 Introduction

Additive Manufacturing (AM) is known for its many advantages in design and manufacturing [123] and its importance has been growing steadily for the last three decades now [124]. However, like any other manufacturing process, the parts produced by AM deviate from their nominal designed geometry. Some industries call for tighter tolerances and more accurately produced parts to ensure top quality and superior performance. Normally, 3D printing these parts necessitates expensive 3D printers, as the lower cost machines will be unreliable [125]. In this case, the compensation to improve the geometric accuracy of the final part provides a very interesting opportunity by allowing the use of less expensive machines, one to two

orders of magnitude cheaper, to produce sufficiently accurate parts.

It is also clear that the 3D printing community was instrumental in filling the gaps of manufacturing cycles of Personal Protective Equipment (PPE) at the beginning of the COVID-19 pandemic [126, 127]. As most machines in this community are of lesser quality and are not professionally maintained and calibrated, the geometric accuracy of printed parts is low. Having an automated and inexpensive way to improve the quality of these parts would be essential in the future to rely on this community in case of emergency.

Bochmann et al. [15] named several sources for the geometrical inaccuracies of the AM processes, including the mathematical errors in the conversion from a 3D model into a surface mesh by the 3D modelling software, the process errors, which includes the deviations due to the positioning inaccuracy of the machine and deformations induced by the layering of the part (i.e., the staircase effect), and the material-related deformations due to the characteristics of the materials used, such as shrinkage or warping. Some of the most common 3D printing technologies are Fused Deposition Modelling (FDM) (also known as Fused Filament Fabrication (FFF)), Stereolithography (SLA), Selective Laser Sintering (SLS), and Multi Jet Fusion (MJF) [128]. The FDM, SLS, and MJF processes require the printing material to be heated close to the fusion temperature for consolidation into a desired geometry, and, similarly, the SLA process requires a laser to polymerize and solidify liquid resin to obtain a solid part [129]. These changes in the state of matter (i.e., solid to semi-liquid to solid, and liquid to solid) result in material shrinkage [130–132] that reduces the geometric accuracy of the finished part and causes residual stresses to accumulate in the part, which can lead to warpage [133].

Researchers have proposed different error compensation approaches to improve the geometric accuracy of AM parts, mainly using a predictive model. Tong et al. [134] proposed a method inspired by the techniques used for machine tools to reduce geometric errors, by creating a parametric error model of the volumetric errors of the machine and compensating the machine's movement accordingly. The error model was obtained based on the measurement of a printed artifact. The machine used in their paper is an SLA 3D printer and the measurement of the artifact's deviation is done using a contact probe on a Coordinate Measuring Machine (CMM). They initially used a 2D artifact. Then, they extended their previous work by using specially designed 3D artifacts and measuring them by CMM to obtain the parametric error model in 3D [105]. The inverse of this error model was then applied to the STL model and later also to the slice files [135] for compensation. Lyu and Manoochehri [136] proposed a parametric error model of the FDM machine augmented by including the effects of interactions between the printing temperature, infill density, and layer thickness. Their

error model was obtained based on the CMM measurement of a printed artifact. By using a CMM, the inspection and compensation rely on the limited number of measurements possible to take.

Huang et al. [111,113,137] proposed a series of statistical error models to predict the in-plane shrinkage and out-of-plane deviation of the printed part. Later, they proposed a convolution model to describe more accurately the deformation of 3D printed parts by processing the 3D model layer by layer and including the effect of layers on previously printed layers [116]. Machine learning can be used on the convolution framework to learn on simulation results and compare them with real-life examples to improve the predictions made by the convolution model. Chowdhury et al. [101] presented an Artificial Neural Network (ANN) to predict deviations and compensate the original CAD model of the part by applying the negative values of the predicted deviations. Their ANN model is trained on deviated models simulated by Finite Element Analysis (FEA) of thermal deviation and strain deformation on the part. This method would not take into account the machine errors, as it compensates only for the thermal deformations. McConaha and Anand [138] implemented the geometry compensation based on scan data of a sacrificial part using a modified version of the developed neural network of [101]. They used a non-rigid variant of the iterative closest point (ICP) algorithm for the registration of scan data and the nominal geometry. Xu et al. [139] proposed a compensation framework in which the nominal model is fabricated and scanned along with some offset models to interpolate the right amount of compensation to apply to each point of the model. This method assumes that the needed compensation is inside the offset values. They used physical markers to help the registration and correlation of the 3D scan data to the reference geometry. Afazov et al. [119] presented an error compensation method that predistorts the nominal surface mesh based on 3D scan data. They proposed that an initial part should be printed based on the nominal geometry, and then scanned and inspected for the specified tolerances. If the deviations of the part are out of tolerance, then the coordinates of the reference surface mesh are updated using distortion inversion. The updated mesh is then used to print the next part. The mesh morphing approach used in our paper is the same general model that was used in theirs. However, their compensation is based on the deviation data of only one part without differentiating the systematic and random deviations.

There is an important gap in the literature of CAD compensation for improving the geometric accuracy of 3D printed parts. The existing works that use the 3D scan data for CAD compensation employ the data from a single part and perform the compensation based on all the deviations measured on that part. When the scan data of a printed part is used to perform compensation, it should be noted that the deviation measured from each part consists of systematic and random portions of manufacturing error. Therefore, it is essential to separate

the systematic deviation from random deviations, otherwise, as random deviations are non-repetitive, including them in the compensation will lead to introducing more deviations in the compensated part.

The original contribution of the method presented in this paper lies in the differentiation between the systematic and random deviations and their application on a compensated part. The presented method uses multiple parts and calculates an average deviation vector field over the original CAD model. Smoothing is also applied over the deviations measured from the scan of each part to eliminate the high-frequency noise and reduce the adverse effects of random errors compared to systematic deviations. We demonstrate the proposed compensation scheme on the Fused Filament Fabrication (FFF) process, but the method can be equally used for improving the geometric accuracy of the parts manufactured by any other additive manufacturing process.

4.2 Proposed Method

Figure 4.1 presents an overview of the proposed method. First, the part is printed N times with the same material and process parameters. Each printed part is then scanned using an optical 3D scanner to capture its 3D shape with a sufficiently high degree of accuracy. In the next step, each scan is aligned with the CAD model of the part and the deviation of each part from its nominal geometry is measured by comparing the scan data and the CAD model. Thanks to the Laplacian smoothing, we can denoise the acquired deviation vector field. Next, the mean deviation vector field is computed based on the N denoised deviation vector fields of the N printed parts. The CAD model geometry is then modified by morphing based on the mean deviation vector field. The morphing locally moves the CAD geometry to the opposite direction of the measurement data to compensate for the systematic errors on the printed part. Finally, the modified CAD is used to print a new part with the same material and process parameters used for the previous N parts. In this work, we chose to print and measure five initial parts (i.e., $N = 5$).

In the following subsections, we describe each component of the proposed approach in detail, and in the same order that they are to be executed.

4.2.1 Printing Sacrificial Parts Based on the Original CAD Model

The first step is to print the part N times with the same material and process parameters. Each of the printed parts has some systematic errors on it and some random errors. The reason for printing these multiple parts is to capture, in the next steps, the map of systematic

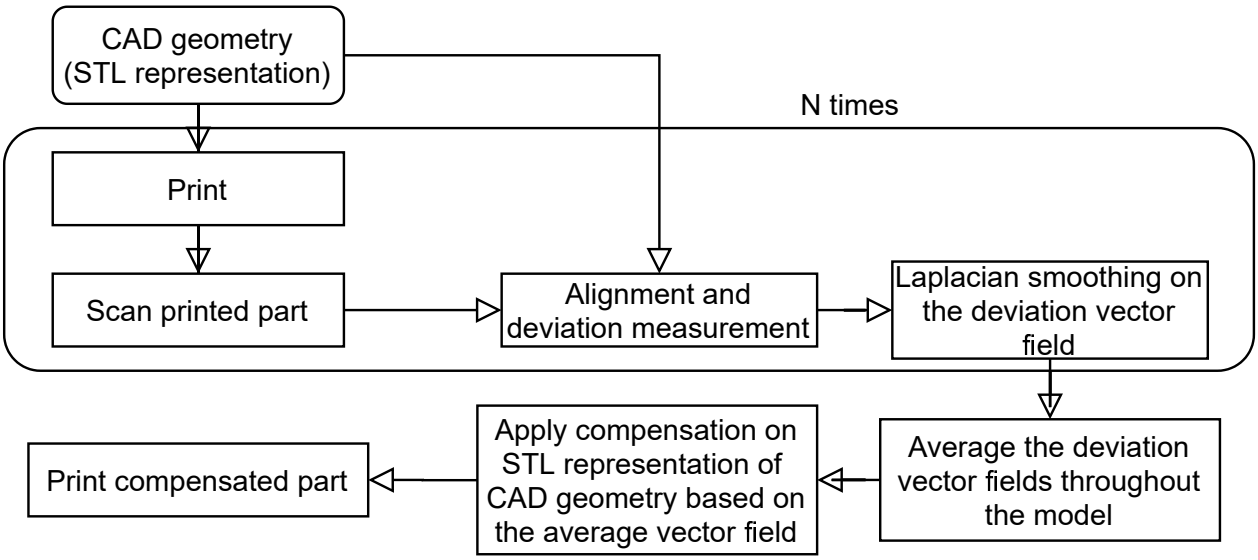

Figure 4.1 Outline of the proposed 3D compensation.

errors on the same part being printed with the same material and process parameters. The more parts that are printed and analyzed, the more reliable would be the acquired map of systematic errors because, with more parts, the effect of individual random errors on the mean is lower. However, there is a trade-off between cost and accuracy. Printing many sacrificial parts can be costly, while the estimate of the systematic errors based on them will be more accurate. In this work, we print five parts, as it appears to be an optimal number considering the cost and accuracy according to our experiments.

To print the part, its 3D CAD model in any CAD/CAM software is exported in Standard Tessellation Language (STL) file format [140]. This file format is used to enable direct manipulation of the data that the slicer, the 3D printing software, will use. The CAD model in the STL format is the CAD surface geometry tessellated into triangles, described by the unit normal vector and vertices of the triangles. The CAD/CAM software (e.g., CATIA) allows the user to set a resolution for the resulting triangular mesh when exporting the model in STL format. The use of a finer mesh reduces the approximation errors of the model and makes the morphing as local as possible later on. However, the ability to handle very high-resolution mesh depends on the computing power available to the user.

4.2.2 Part Inspection

Once each part is printed, it has to be inspected first by comparison against the original CAD model to recognize any deviations on the part. To ensure a complete inspection throughout

the part, we should capture high-density surface measurement data. To this end, the part is digitized using an optical 3D scanner. An optical 3D scanner was deemed the more appropriate solution as it is easier to obtain accurate and repeatable results. The scanned data are collected as a point cloud.

Registration and Deviation Measurement

The point cloud data from 3D scanning and the CAD model are not originally located in the same coordinate frame. To be able to compare the scanned data and the CAD model, they must be brought to a common coordinate frame via a registration (aka alignment) algorithm. Therefore, accurate registration of the scanned data and the CAD model is a critical step to ensure a reliable geometric deviation measurement. We use the Iterative Closest Point (ICP) algorithm [141] for registration, which is one of the most popular registration methods. The ICP algorithm consists of the following four steps:

1. For each point of the scan data, find the closest vertex on the tesselated representation of the CAD model as its corresponding point.
2. Find the rigid body transformation (translation and rotation) that minimizes the mean of squared distances between the corresponding pairs of scan point and CAD vertex.
3. Apply the transformation of Step 2 to the scan data.
4. If the change in the mean of squared distances between the scan points and CAD vertices falls below a pre-specified threshold, stop. Otherwise, iterate from 1.

Once the scan data and the CAD model are properly aligned, for each vertex of the tesselated representation of the CAD model, we find the closest point of the scan data. Then, we compute the vector $vf_{v,er}$ from the CAD vertex to its corresponding closest point of the scan. The deviation vectors from CAD to scan at all the vertices of the CAD mesh form the deviation vector field vf_{er}.

4.2.3 Random Error Reduction Strategies

The deviation vector field obtained by comparing the scanned data of a printed part to the CAD geometry will have two types of deviations: systematic deviations, which are repeatable and can be detected on multiple parts printed by the same machine with the same parameters, and random deviations, which are also present in every single part, but are different on each one of them [142].

The random errors are from both the manufacturing process and the 3D scanning process itself [143]. It matters little to differentiate between the two sources, but it is important to make sure that the compensation that is applied to the CAD geometry is based on actual systematic deviations and not on random noise. To do so, two tools are applied to reduce the adverse effects of noise and random variations in the data: (1) smoothing (denoising) the deviation vector field acquired from the scan data of each single part, and (2) averaging the deviation vector fields of multiple parts.

Smoothing

High-frequency noise is initially present in the scan data. Smoothing the vector field vf_{er} can reduce the noise that would be transferred to the compensated part. The noise attenuation is performed through a diffusion process. Laplacian smoothing is applied, which is considered as the time integration of the heat equation on a mesh [144]. It is then possible to solve the discrete heat diffusion equation on the CAD model's mesh to smooth the vector field vf_{er} [145]. The solution of this equation is a new vector field $vf_{er,m+1}$ that is smoother than the previous vector field $vf_{er,m}$. Equation (4.1) is then solved iteratively from $m = 1$ to $m = 10$, where $vf_{er,1}$ is the original vector field of deviations before smoothing. $\lambda = 0.05$ is used and L is the discrete cotangent Laplace–Beltrami operator as described by Bunge et al. [146]:

$$vf_{er,m+1} = (I + \lambda L)vf_{er,m} \tag{4.1}$$

Averaging the Deviation Vector Fields

Once each deviation vector field of the five scans is smoothed (denoised), an average vector field $vf_{av,er}$ is computed from the smoothed vector fields to extract the systematic deviations. To do so, deviation vectors measured at every vertex of the tesselated representation of the CAD model from the five scans are averaged. The average vector at each vertex is calculated component-wise. In other words, the mean of five values for each one of the three coordinates X, Y, Z is calculated as the coordinate of the average deviation vector. The average vectors at all the vertices form the average deviation vector field $vf_{av,er}$.

4.2.4 Morphing

The morphing procedure is performed on a copy of the CAD model surface mesh. Equation (4.2) shows the mathematical representation of the morphing:

$$V_{NEWmesh} = V_{CADmesh} - vf_{av,er} \tag{4.2}$$

$V_{NEWMESH}$ is the compensated CAD mesh, $V_{CADMESH}$ is the original CAD mesh, and $vf_{av,er}$ is the average deviation vector field.

In essence, we move the CAD surface mesh inward where the systematic deviations bring the printed part's surface outside the nominal, and we move it outward where the part's surface is inside the nominal, with the exception of the following:

- The algorithm does not move the points of the bottom surface, in order to allow a good printing surface. Their position remains the same as it was before the compensation.
- The algorithm eliminates the deviations on the mesh that are bigger than a realistic predetermined range. This range is fixed at 500 μm as the range of deviations for FDM 3D printers is usually smaller. [31]

The final surface mesh obtained after compensation can then be sliced using the same parameters and printed using the same printer with the same material.

4.3 Results and Discussion

4.3.1 Experimental Setup

To verify the effectiveness of the proposed method, we printed a test part of the National Institute of Standards and Technology (NIST) five times using an *Ultimaker 3* (Ultimaker, Geldermalsen, Netherlands) 3D printer (Figure 4.2) with white 2.75 mm PLA filament from Ultimaker. The adopted part is CTC 5 [147], shown in Figure 4.3. The part was scaled uniformly to a reasonable size to print. The outside dimensions of the part are $75.00 \times 79.52 \times 70.47$ mm. CATIA allows the export of the part's CAD model in the STL file format by imposing a step (i.e., maximum edge length) and a maximum chord deviation. In this work, the step was set at 0.5 mm and the maximum chord deviation at 0.001 mm. This allowed to minimize the deviation between the STL and the original CAD model and make it negligible in our experiment [148]. The exported STL model was sliced using Ultimaker Cura with the fast default profile and the layer height set to 0.04 mm. With the negligible

part file errors, the deviations of the printed part are mostly due to the machine's imprecision and the material shrinkage. Table 4.1 presents the process parameters used for printing the original and compensated parts.

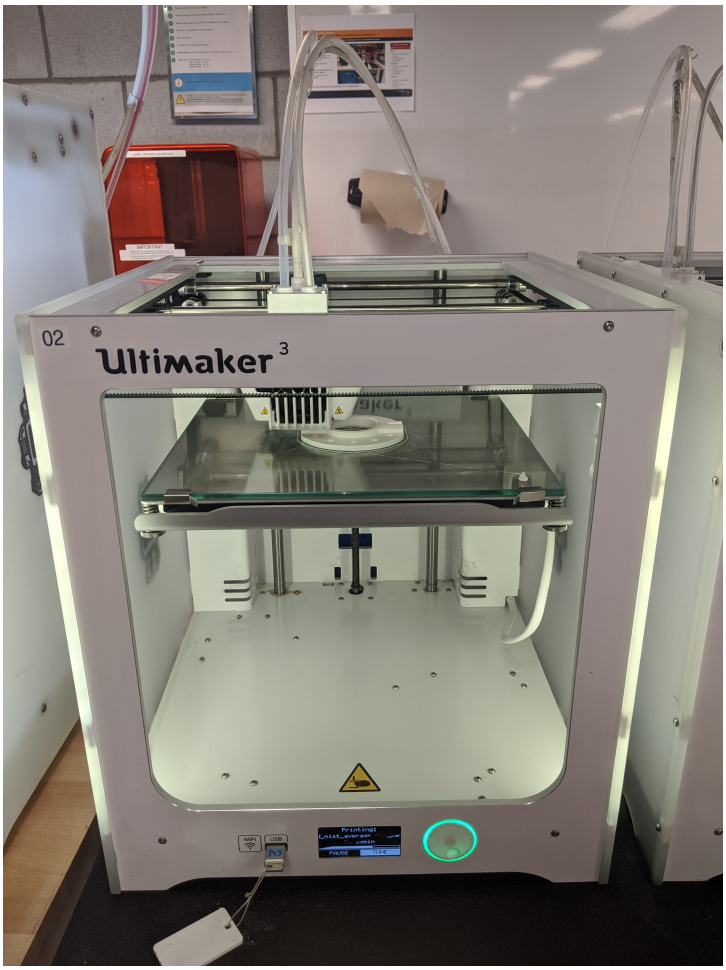

Figure 4.2 Ultimaker 3, 3D printing the part in PLA.

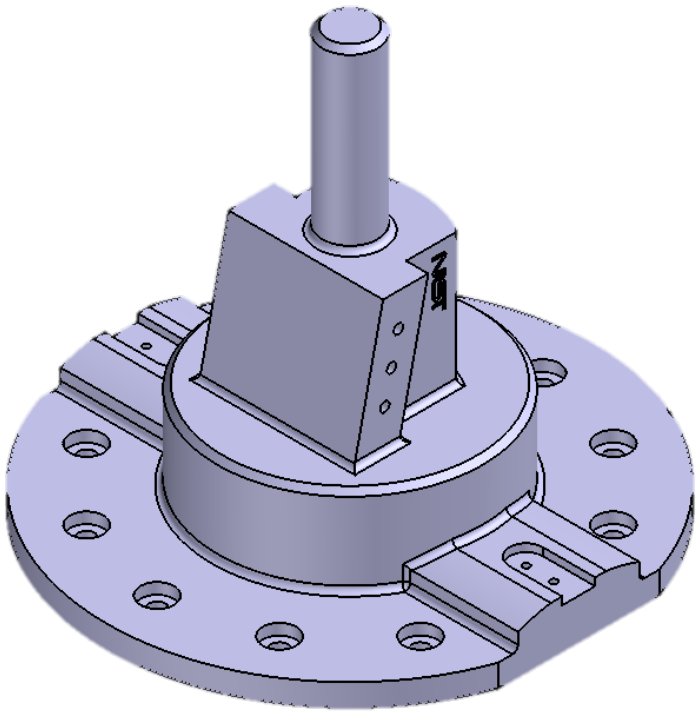

Figure 4.3 NIST CTC 5 CAD model.

Table 4.1 Printing parameters for the original and compensated parts.

Printing temperature	215 °C
Printing speed	70 mm/s
Cooling	100%
Support	None
Infill type	Triangles
Infill density	10%
Plate adhesion	None
Layer height	0.04 mm
Nozzle diameter	0.4 mm

Each printed part was visually inspected first to make sure that no burrs, stray filaments, or major defects were present and then scanned using an ATOS Core 200 (GOM, Braunschweig, Germany) 3D scanner (Figure 4.4). The scan data are then exported from GOM Scan (the scanner's data acquisition software). The resulting scan data are made of about 300,000 points at a density of $28\frac{\text{points}}{\text{mm}^2}$. The scanner is able to detect every detail on the surface of the part, even the track of the printer's nozzle (Figure 4.5). However, the holes on the sides and the bottom are harder to scan. A study of the 3D scanner's accuracy in [149]

demonstrated an accuracy of 10 µm in length measurement and, more interestingly for us, 2 µm in the probing error of form measurement.

The proposed algorithm is coded in Python 3.6. External libraries, namely the Trimesh [150] for mesh processing, and the Libigl python bindings [151] for the quick computing of the distances are used.

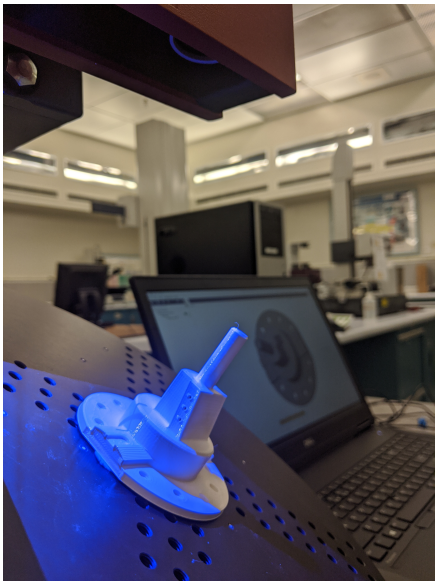

Figure 4.4 3D scanning setup with ATOS Core.

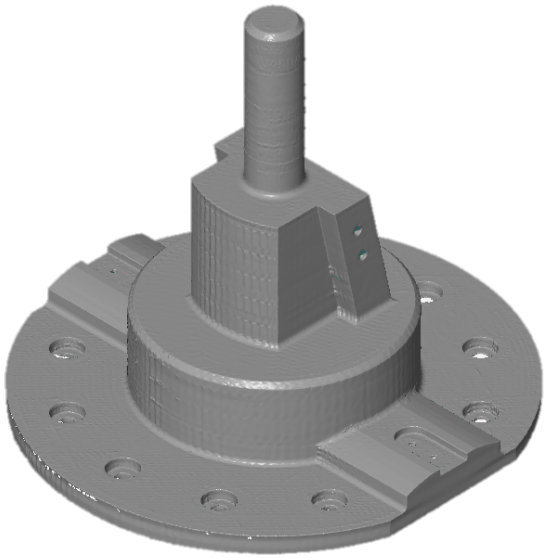

Figure 4.5 Scan data of the printed part.

4.3.2 Comparative Analysis

The comparison between the scan data of each printed part and the original CAD model yields the geometric deviation of the part. The colormaps of the deviations of the five printed parts (A–E) with respect to the original CAD model is presented in Figure 4.6. The deviation values on the colormaps represent the signed Euclidian distance of the deviation vectors. The sign of these values represents the direction of the deviation; A negative value means the deviation vector points opposite to the CAD surface's normal vector and vice-versa.

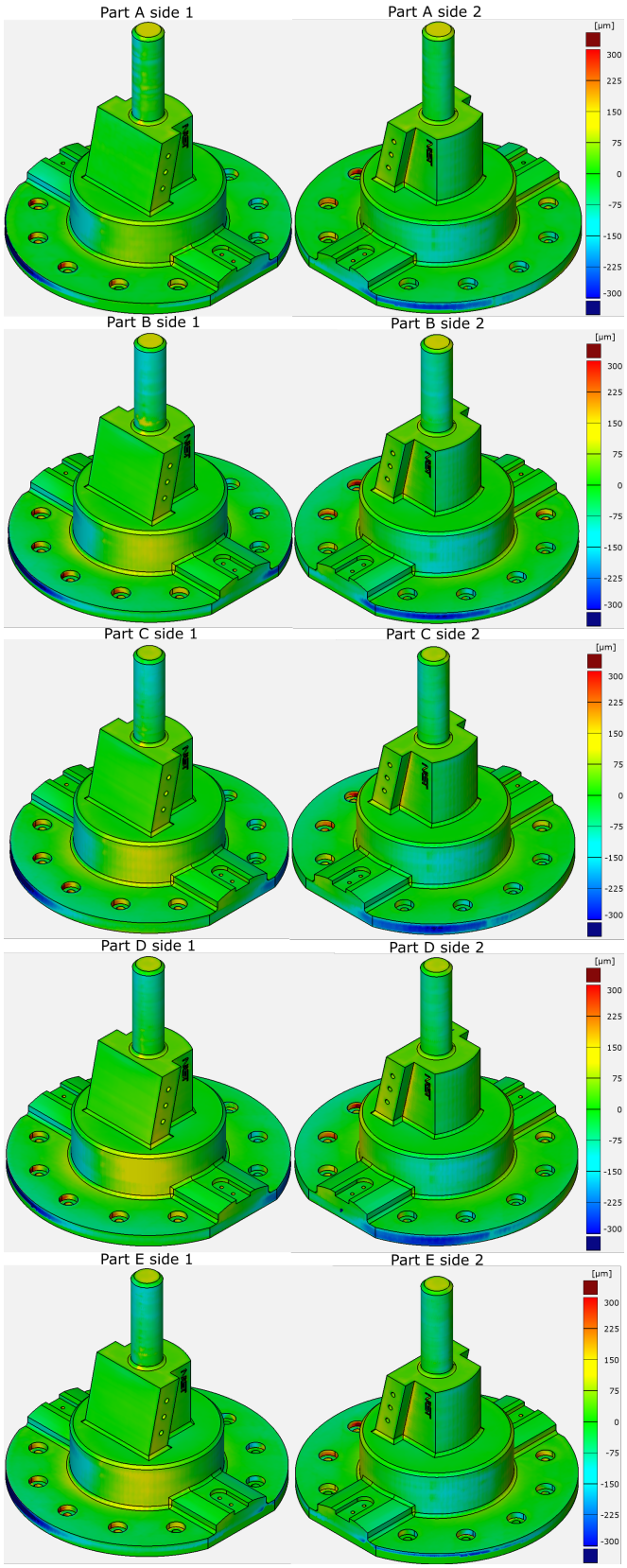

Figure 4.6 Deviation colormaps of the five original printed parts, ranges are in µm.

The results of Sections 4.3.2 and 4.3.2 validate the proposed compensation approach using the average deviation obtained from five parts and compare it to the compensation based on only one part. To this end, two compensated parts are obtained and compared. The first one only uses the deviation vector field of Part B for its compensation. The deviation vector field obtained from the scan was smoothed by the presented Laplacian smoothing before the morphing. The selection of which part to use for the compensation was random so as to not affect the result. The second one uses the average of all of the five parts' deviation vector fields as proposed in this paper.

Deviation Analysis

Part B, the part based on which the first compensated part was obtained, chosen randomly, can be seen in Figure 4.6. It has an average absolute error of 53 µm and a standard deviation of 60 µm. The 99th percentile of the absolute errors is at 318 µm. There is a clear deviation on the cylinders and other round features. There are some random deformations that are not repeated in other colormaps of Figure 4.6 (e.g., the yellow patch near the bottom of cylinder A, see figure 4.11). The compensated part based on these deviations is displayed in Figure 4.7.

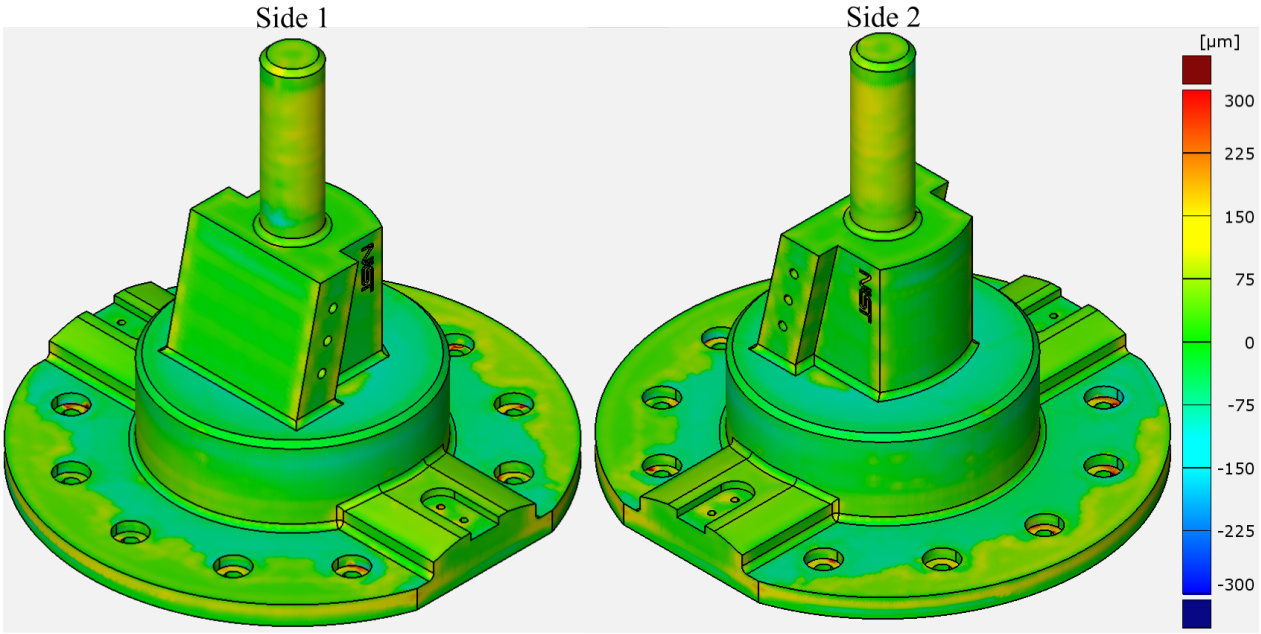

Figure 4.7 Deviation colormap of the compensated part based on part B, range is in µm.

The average absolute error of this compensated part is 52 µm and the standard deviation is 48 µm. The 99th percentile is at 221 µm. Compared to Part B, the average absolute error

of the compensated part shows no improvement, but the standard deviation and the 99th percentile show an improvement of 20% and 31%, respectively.

Table 4.2 presents the values of the average of absolute errors, standard deviation, and the 99th percentile of absolute errors for each of the five initial parts and the two compensated parts. The average absolute error of all the five original parts (of Figure 4.6) combined is 51 μm with a standard deviation of 57 μm. The average 99th percentile is at 311 μm. It can be observed in Figure 4.6 that the deformation on the cylinders is present in every colormap, with a slight difference between them. It is then clear that there is a systematic deviation there that should be eliminated. The average deviation colormap and the standard deviation colormap are displayed in Figures 4.8 and 4.9. The average colormap shows deformation patterns similar to the ones on each individual part of Figure 4.6. The low values on the standard deviation colormap confirm that the manufacturing process typically causes similar deviations in the same regions of the part.

Table 4.2 Average of absolute errors, standard deviation, and 99th percentile of absolute errors of the original five parts (A–E) and the two compensated parts.

	Average of Absolute Errors (μm)	**Standard Deviation (μm)**	**99th Percentile of Absolute Errors (μm)**
Compensated part based on the average deviation of 5 parts	23	20	98
Compensated part based on deviation of part B	52	48	221
Part A	52	62	330
Part B	53	60	318
Part C	51	57	309
Part D	49	54	288
Part E	48	54	309

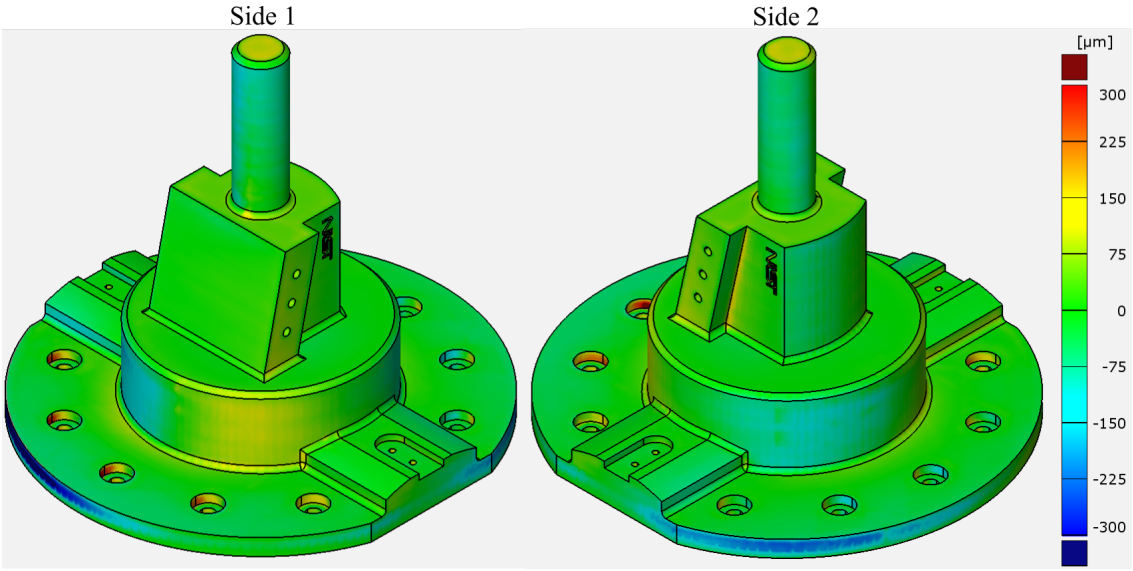

Figure 4.8 Average deviation colormap of the five original printed parts, range is in µm.

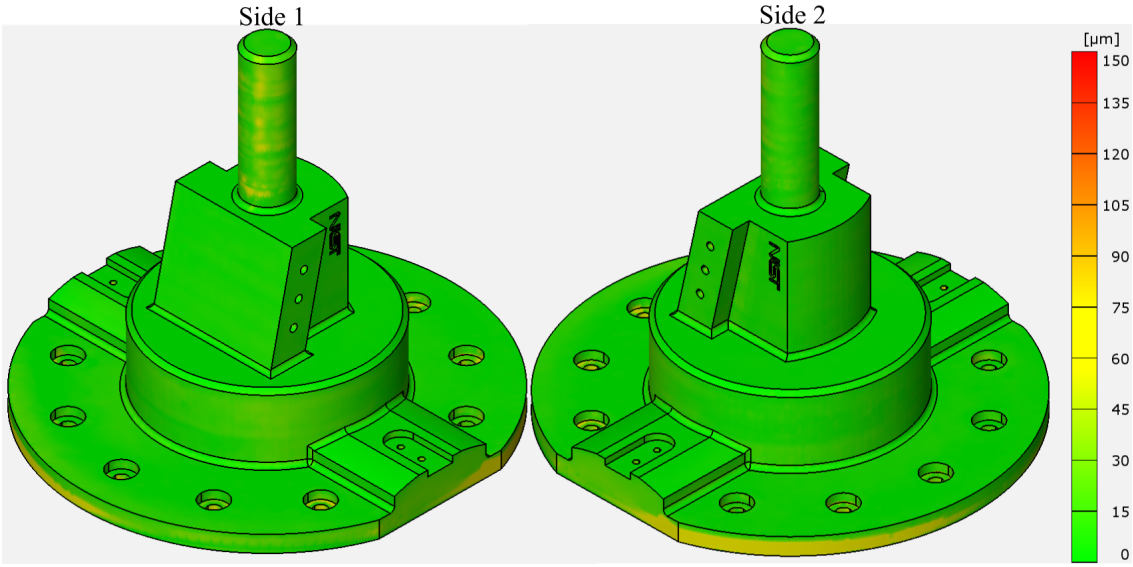

Figure 4.9 Standard deviation colormap of the five original printed parts, range is in µm.

The compensated part based on the average of the five original parts is presented in Figure 4.10. It is clear that the cylinders show no deviations like the original parts and the deviations are smaller on the horizontal surfaces. The average absolute error of the compensated part is 23 µm and the standard deviation is 20 µm. The 99th percentile is at 98 µm. These are an improvement of 55%, 65%, and 68%, respectively.

Random deviations are still clearly visible on the compensated part. These are, in part,

from the manufacturing of the compensated part and the measurement, but also from the random deviations that are non-negligible in the average deviation vector field and are included in the compensation.

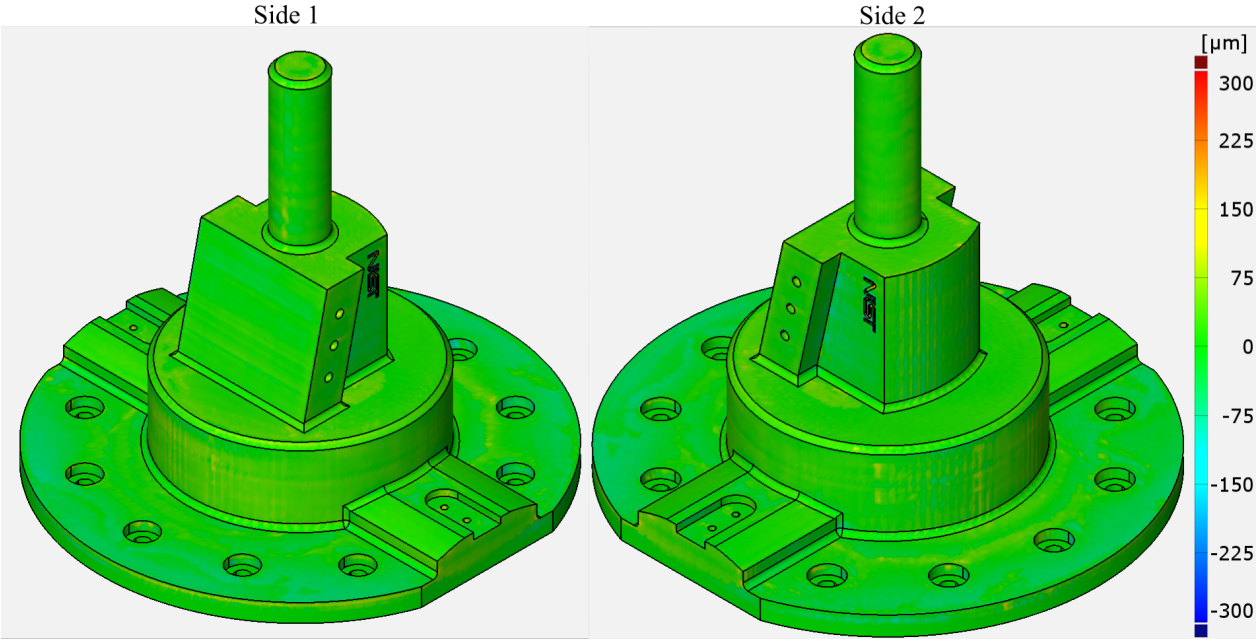

Figure 4.10 Deviation colormap of the compensated part based on the average of five parts, range is in µm.

Tolerance Analysis

A Geometric Dimensioning and Tolerancing (GD&T) analysis is also performed, using GOM Inspect software, on each printed part. GD&T requirements are often used to increase the interchangeability of manufactured parts by ensuring the tolerance is sufficiently tight for specific engineering intents while allowing for variations in other directions. The tolerance features can be identified in the drawing of Figure 4.11. The tolerances are not the ones originally defined on NIST CTC 5 part. We have specified these tolerances merely for the sake of case studies of this paper. The standard used for tolerancing is the ASME Y14.5 2018 [152]. As it can be seen in Figure 4.11, the cylindricity tolerance is defined for cylinder A, the position tolerance is specified for the centroid of the 10 holes on the bottom surface, named as element group B, and the angularity tolerance is defined for plane C with respect to plane D as datum.

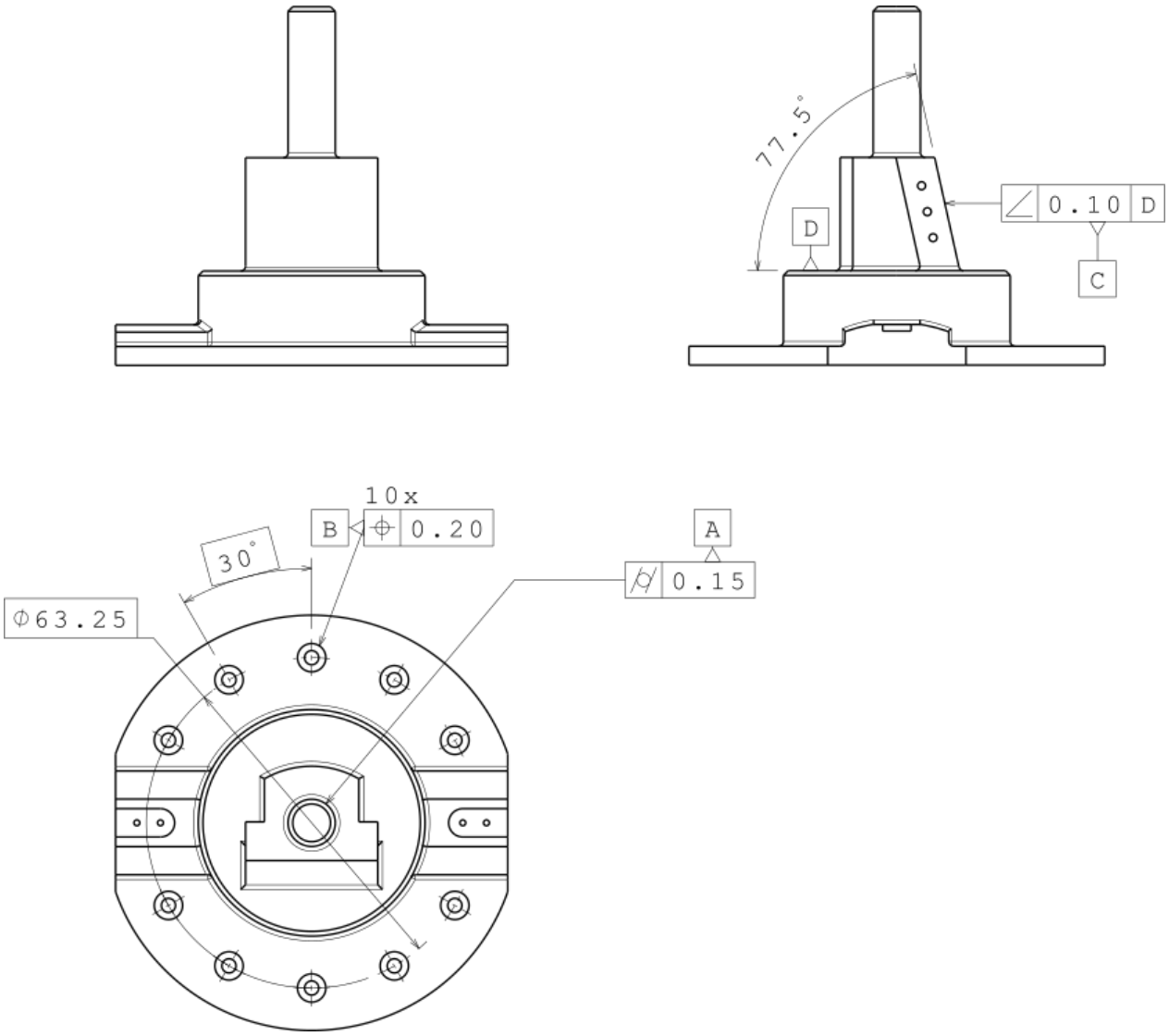

Figure 4.11 Drawing of the part with the toleranced features to inspect. Unless otherwise specified, dimensions are in mm.

Table 4.3 presents the specified tolerance values for each of these tolerances and the corresponding deviation values obtained from the scan of each of the printed parts, namely, the initial five parts (A–E) and the two compensated parts.

Table 4.3 The values of the specified tolerances on the part, and the corresponding deviation values obtained from the scans for each of the five initial parts, the compensated part based on part B, and the compensated part based on the average of five parts. The values are in μm.

Element	**Cylinder A**	**Element group B**	**Plane C**
Datum			**Plane D**
Property	**Cylindricity**	**Position**	**Angularity**
Tolerance	150	200	100
Deviation of Compensated part based on the average deviation of five parts	125	179	98
Deviation of Compensated part based on part B	165	194	156
Deviation of part A	285	499	108
Deviation of part B	282	455	103
Deviation of part C	244	499	117
Deviation of part D	179	502	125
Deviation of part E	273	471	122

It can be seen in Table 4.3 that the five original parts (A–E) are out of tolerance for all three features. The compensated part based on part B is out-of-tolerance for two tolerances. Cylinder A is out of tolerance because the compensation included a random deviation from part B. The yellow patch mentioned earlier in Figure 4.6 was compensated; its inverse, a blue patch, is visible in Figure 4.7. This patch, as it is not a high-frequency error, was not filtered by the Laplacian smoothing.

Finally, it can be seen in Table 4.3 that the compensated part based on the average deviation of the five original parts is in-tolerance for all inspected features. The compensation is clearly effective in removing deviations on cylindrical shapes. The reduction in cylindricity deviation, compared to the average of the five original parts is 51% for cylinder A. The position deviation of holes B is reduced by 61% and the angular deviation for plane C is reduced by 15%.

4.4 Conclusions

The proposed method of surface mesh compensation based on 3D metrology feedback adjusts the CAD model to oppose systematic deviations. The main sources of these deviations are material shrinkage and residual stress-induced deformations, as well as the positioning errors of the machine. We proposed the compensation based on the average deviation vector field obtained from the scans of multiple printed parts to ensure that the compensation is performed only for the repeated systematic deviations and not the random deviations of a

single part. The use of an optical 3D scanner allows for quick digitization of the printed parts. Local deviations can be easily measured since a high-density point cloud is obtained through optical 3D scanning. The presented Laplacian smoothing can filter out the high-frequency noise of the scans.

The case study results confirm that random deviations have an adverse impact on the compensation outcome if not mitigated by compensating based on the average deviation of multiple parts. The compensation based on the deviation of only one part shows a lower capacity to reduce deviations as the improvement of geometrical accuracy was only 31%. This was not enough to bring the deviations of the compensated part within all specified tolerances.

The proposed approach of compensation based on the average of five parts is able to improve geometrical accuracy by 68% based on the 99th percentile of absolute deviations. The proposed compensation based on the average of five parts could successfully bring the deviations of the compensated part within the specified tolerance values.

CHAPTER 5 ARTICLE II: INCREASING 3D PRINTING ACCURACY THROUGH CONVOLUTIONAL NEURAL NETWORK-BASED COMPENSATION FOR GEOMETRIC DEVIATIONS

Authors Moustapha Jadayel, Farbod Khameneifar

Submitted to the Journal of Progress in Additive Manufacturing on September 9th 2024.

Abstract As Additive Manufacturing (AM) transitions from prototyping to full-scale production, addressing its inherent geometric accuracy issues becomes critical. In this study, we propose a novel approach to enhance the geometric accuracy of 3D printed parts of the Fused Filament Fabrication (FFF) process. By employing a trained Convolutional Neural Network (CNN), we generate a systematic deviation scalar field based on the scan data of a sacrificial 3D printed part obtained by a structured light 3D scanner. We demonstrate that the original geometry compensated by the inverse of the systematic scalar field generated by the compensation CNN produces part with a reduction of 88.5% mean absolute geometric deviations. Our results suggest that this technique can improve the overall quality of AM-produced parts and support their broader adoption in industrial applications.

5.1 Introduction

Fused Filament Fabrication (FFF), often referred toq as Fused Deposition Modeling (FDM), involves the layer-by-layer extrusion of thermoplastic filament to create three-dimensional objects [153], making it an easily adoptable and accessible form of additive manufacturing. An evident advantage of the FFF process lies in its capacity to generate intricate geometries with printed support structures, eliminating the necessity for individual setups for each unique part. Such attributes render FFF particularly suitable for rapid prototyping or small-scale production scenarios where geometric accuracy is not the primary concern, and lead time is paramount [154]. Lately, FFF has increasingly found applications in larger-scale manufacturing environments. The accessibility and adaptability of AM machines have transformed them into indispensable tools within factory settings, where their capacity to produce intricate geometries on-demand is invaluable [155, 156]. This evolution reflects the shifting role of FFF and analogous AM techniques from temporary prototyping solutions to permanent components within the manufacturing landscape, offering novel avenues for innovation and efficiency.

To support this evolution, researchers have investigated the geometric accuracy of additively manufactured parts to assess the reliability of AM machines in producing geometrically correct parts. Additionally, efforts are underway to develop methodologies to improve the geometric accuracy of 3D-printed parts, enhancing FFF technology's overall capabilities and applicability. The following sections will review related works in this area.

5.1.1 Dynamic Process Parameter Adjustments

One method to indirectly improve the geometric accuracy of a 3D printed part is by dynamically adjusting the 3D printing process parameters, such as the deposition rate, movement speed, and nozzle temperature, in a closed feedback loop. By improving the stability of process parameters, the resulting printed part should remain close to its specified geometric accuracy, thus reducing non-repeatable errors. Dynamic parameter adjustments can additionally affect the mechanical capabilities of a manufactured part by ensuring that the optimal printing parameters are consistently maintained, thus resulting in more reliable mechanical properties. Ye et al. [157] propose a deep forest approach to detect the effects of a process shift using the 3D scan measurement of a 3D printed part. Tamir et al. [158] use an in-situ camera to capture the newly printed layer and a combination of Machine Learning (ML) models and a fuzzy logic controller to adjust four printing parameters to remain at optimal values for the duration of the printing process. Brion and Pattison [159] demonstrate a multi-head Neural Network, a neural network with multiple secondary neural networks with different objectives, able to determine deviations from optimal process parameters by analyzing images of deposited material in FFF 3D printers. Detecting parameter drift allowed automated process parameter adjustments to keep the printer working within expected conditions and improve geometric accuracy. Many other researchers contributed to this field of study by analyzing different materials [160] or processes [161], by adding new parameters [162] or by implementing different methodologies to detect process parameter shift [163].

5.1.2 Predictive Geometric Compensation

Another exciting approach investigated by many researchers is to enhance the geometric accuracy of additively manufactured parts by analyzing and optimizing the 3D model before printing to identify predictable deviations and modify the print file accordingly, eliminating any errors or issues affecting the final print's geometric accuracy. Some researchers have proposed pre-compensating the 3D model of the desired part by running a Finite Element Analysis (FEA) of the printing process to predict the deviations caused by thermo-mechanical deformations caused by the printing process [164]. Chowdhury et al. [101,165] propose to use

FEA simulations to build a training dataset for an Artificial Neural Network (ANN). The ANN would be faster and more generalizable to new situations without requiring the valuable time of experienced personnel to set up and run an FEA simulation. Francis and Brian [166] have demonstrated a neural network able to predict the distortion of a Laser-Based Additive Manufacturing machine by measuring the local heat transfer from the Laser to the solidified part. This Neural network retains a thermal history of the heat distribution and produces a prediction of deviation due to thermo-mechanical effects. Nath et al. [167] propose a similar process design optimization framework to optimize the FFF process parameters. The thermal history obtained from simulation is used to predict the geometrical inaccuracy of the printed part. The FFF process parameters are then optimized to minimize the inaccuracy by affecting the thermal history obtained from the simulation.

5.1.3 Retrospective Error Analysis

Another method for enhancing the geometric accuracy of AM machines involves leveraging the geometric deviations observed in a sacrificial part to inform the fitting of an error model. Tong et al. [134] propose a parametric error model for the laser focal point positioning in a StereoLithography Apparatus (SLA) 3D printer. A kinematic path from the origin of the machine to the laser focal point is created by measuring with a Coordinate Measuring Machine (CMM) the deviations of a printed part to accumulate the rotational errors of predecessor axes to the current axis. Running axis errors are repeatable and are only related to the theoretical position of the laser focal point. In addition, a random error term is added to the parametric error model, representing the errors due to non-repeatable components. Parametric error analysis is further explored by Huang et al. [111] who compute a predictive statistical model best-fitting the deviation of an SLA 3D printed part. The statistical model is a closed-form equation with three components: the average deviation of the printed part, the position-dependent deviations, and a high-frequency component added to the main trend. The authors also present the equation in polar form to clarify the relationship between the deviated and nominal points, reducing potential confusion. Both researchers aim to build a model that can fit the deviations produced by a 3D printer. The solution to the equation allows the authors to modify the CAD model accurately to overcome repeatable errors and minimize the impact of random errors in their model.

SLA 3D printers are often more accurate than FFF 3D printers [168] and can produce a more stable and repeatable dataset, ideal for parametric analyses such as those previously presented. On the other hand, FFF 3D printers have a more complex kinematic system due to the need to precisely coordinate multiple moving parts and manage filament extrusion, which

introduces additional variables and potential sources of error and increases the complexity required for predictive statistical models. Wang et al. [169] produce a statistical prediction model based on Kriging spatial statistics [109], which is suitable due to the natural spatial correlations in the extruder positioning error. The prediction model is experimentally tested by modifying the CAD model by the inverse of the predicted deviation, demonstrating it as an effective in-plane deviation compensation method. Alternative geometric compensation schemes are proposed and compared experimentally by Cheng et al. [115], integrating process parameters into their statistical model to make it more generalizable.

To help determine the optimal compensation equation, an analytical framework is proposed by Huang [137] using quality measures, such as the Minimum Area Deviation and Minimum Volume Deviation. Then, to improve the geometric accuracy of freeform geometries, a generic and prescriptive methodology is established by Luan and Huang [170]. A convolution framework is also developed by Huang et al. [116] to predict 3D shape accuracy. This convolution model provides a layer-by-layer in-plane prediction of deformation, which can be used to compensate the initial geometry to eliminate the predicted deviations. Wang et al. proposed a formalized mathematical decomposition for fabricating non-smooth 3D printed parts, involving additive building of smooth base shapes followed by subtractive removal of extra material. Their model accounts for predicted deviations using location-dependent, process parameter, and shape-dependent covariates, with a zero-mean random field for spatial correlation and measurement error [122].

5.1.4 Machine Learning for modeling and improving the geometric accuracy of AM

Machine learning for AM has been a new trend, and researchers have been applying machine learning tools to improve AM performance. Wang et al. [171] do so by creating a learning framework for shape deviation modeling and learning of 3D geometries in AM by decomposing the AM process in an additive and a subtractive step to unify smooth and non-smooth shapes. A Bayesian methodology is employed by Sabbaghi et al. [172] to model deviations in a polygon and straight edges of freeform objects based only on the deviation measured on pentagons and cylinder, showing the capacity of the author's model to generalize based on a limited dataset. Sabbaghi and Huang [173] refined this methodology by developing a new effect equivalence framework to enable the deviation model to transfer across AM processes.

Tsung et al. [174] explore transfer learning to share domain knowledge and combine multiple data sources for shape deviation prediction for 3D printed parts. The domain knowledge sharing would enable statistical models built for a specific geometry or printing process to

be generalized to other applications. Ferreira et al. [175] present a methodology for building a predictive shape deviation model for different 3D geometries by implementing a class of Bayesian Neural Networks to reduce the need for user inputs and efforts. Another Bayesian methodology is employed by Tao et al. [176] to identify and model anomalies in an unorganized 3D point cloud. This method can also discriminate outliers, allowing for higher accuracy in acquiring automated measurement data. Huang [177] decomposes the input geometry into stacks of 2D primitive geometry, which simplifies the printing process and enables them to establish an impulse response formulation and modeling framework to apply control theory to AM. Khanzadeh et al. [178] propose to use self-organizing maps on 3D printed parts scan data to define the geometrical quality of a 3D printed part when a large dataset is obtained from 3D scanning. Decker et al. [120] propose a data-driven methodology of compensating a 3D printed part to increase the geometric accuracy by training a random forest model [179], a machine learning algorithm that constructs a multitude of decision trees during training and outputs the average prediction of the individual trees, and using it to predict the systematic deviations on a known geometry. An advantage of the proposed methodology in [120] is that it is not limited to planar deviations and can control all dimensions simultaneously.

Zhu et al. [103] demonstrate that a trained Convolutional Neural Network can reliably predict layer-by-layer, in-plane and out-of-plane, geometric deviations of simple geometries. The Convolutional Neural Network presented by the authors enables a user to predict deviation distribution in three dimensions. Li et al. [180] produce a trained Conditional Adversarial Network able to predict the out-of-plane geometric inaccuracies of a printed part with the slice of a CAD model as input. The proposed Conditional Adversarial Network allows the authors to apply compensation to the CAD model before printing. McGregor et al. [181] separate the inference of geometric accuracy of 3D printed parts into two algorithms: a feature detection algorithm to classify the geometry and a shape deviation generator that is specialized to each type of geometry. The two-algorithm approach limits the scope of the shape deviation predictor while enabling the algorithm to be broader.

Zhao et al. introduced a neural network-based approach using point cloud data, with 3 set abstraction levels and three interpolation layers before an MLP, achieving an average error of 0.037 mm on the test dataset [121].

Some researchers presented in this study reported using Artificial Neural Networks and their derivatives to solve the complex problem of geometric accuracy improvement of 3D printed parts. Indeed, Artificial Neural Networks have proven to be a powerful tool for such complex tasks [182]. For instance, the tasks of image classification [183] and image processing [184] presented significant challenges, but Convolutional Neural Networks (CNNs) have shown great

potential and are showing continuously improving results [185]. CNNs make use of spatial correlations in the input data, usually images or videos, resulting from pixel arrangement and organization [58] and can detect patterns not necessarily discernible by a human [186]. Because 3D models, surface meshes, or point clouds do not have spatial correlations in their data structure, other types of ANN were developed to work with them. For example, PointNet can classify 3D models in real-time with a novel input format to enable itself to use the CNN architecture [187]. Many other Neural Networks have been developed for model segmentation [188, 189], object detection [190] and 3D model reconstruction [191].

Based on a review of the current literature, while several techniques have been developed to assess and improve the geometric accuracy of 3D-printed parts by analyzing deviations and fitting models to represent systematic deviations caused by the printer, a significant gap remains unaddressed. Specifically, no methods can produce a representation of systematic deviations caused by a printer by analyzing the deviation patterns present in the raw deviation data of a 3D printed part. One proposed approach is to print five sacrificial parts of the same geometry on the same machine and average their deviation vector field [192]. The average deviation vector field can then be utilized to compensate the nominal geometry and produce a part with significantly lower geometric deviations. However, printing multiple sacrificial parts can be wasteful and expensive in terms of cost and time.

We propose a new ML compensation method to compute the systematic deviation scalar field from a single sacrificial part to address this issue. Given enough training data, the proposed method can potentially compute the systematic error of any printed part from any FFF 3D printer without requiring additional training data. It also significantly reduces the number of sacrificial parts required after training and simplifies the overall process while maintaining or improving the quality of the final part. The proposed compensation CNN also differs from currently available methodologies by eliminating the geometric specificity inherent in other compensation approaches, which often require expert knowledge to produce the deviation model for a particular geometry. In addition, by pre-training the model on a large dataset, the proposed method has the potential to further improve the geometric accuracy of 3D printed parts by ensuring that the compensation for each point is treated independently. This approach allows the algorithm to effectively handle varying patterns of deviation across different sections of a printed part, maintaining high accuracy regardless of localized differences in the deviation field.

5.2 Proposed Method

The present study follows previous investigations that have demonstrated that morphing the nominal geometry by the inverse of the systematic deviations measured on sacrificial parts can enhance the geometric accuracy of subsequent printed parts [192]. However, the authors note that the raw deviation scalar field obtained from measuring a single sacrificial part E_1 comprises two distinct components: systematic deviation E_S and random errors E_{R1}, as shown in equation 5.1. Although compensating the nominal geometry using both components of the deviation scalar field might eliminate some of the systematic deviations, it would also contain random errors, as is shown in equation 5.2. In that equation, E_C and E_{RC} are the deviation scalar field and the random errors of the compensated part. The random errors E_{R1} and E_{RC} are theoretically independent and different in any two printed parts.

To address the accumulation of random errors issue, the authors propose to use the average deviation scalar field by printing and measuring multiple parts. Theoretically, since the systematic deviations are repeated in all parts printed in the same machine with the same printing parameters, the systematic deviations should be represented in the average deviation scalar field. In contrast, the random errors should be significantly reduced, as they are not repeated.

The average deviation E_{ave} of n parts is computed by equation 5.3 with E_i the error of scanned part i. The systematic deviation E_S average remains constant, and the averaged random deviation components E_R are added. Equation 5.4 shows the deviation $E_{c,ave}$ of a part compensated with the average deviation scalar field. The systematic deviations E_S are still eliminated. However, the random error component is reduced by a factor $\frac{1}{n}$, improving the geometric accuracy of the compensated part.

$$E_1 = E_S \pm E_{R1} \tag{5.1}$$

$$\begin{aligned} E_C &= E_S \pm E_{RC} - E_1 \\ E_C &= E_S \pm E_{RC} - (E_s \pm E_{R1}) \\ E_C &= \pm(E_{RC} + E_{R1}) \end{aligned} \tag{5.2}$$

$$
\begin{aligned}
E_{ave} &= \frac{1}{n}\sum_{i=1}^{n} E_i \\
E_{ave} &= \frac{n \times E_S}{n} \pm \frac{1}{n}\sum_{i=1}^{n} E_{Ri} \\
E_{ave} &= E_S \pm \frac{1}{n}\sum_{i=1} E_{Ri}
\end{aligned}
\tag{5.3}
$$

$$
\begin{aligned}
E_{c,ave} &= E_S \pm E_{RC} - E_{ave} \\
E_{c,ave} &= E_S \pm E_{RC} - E_S \pm \frac{1}{n}\sum_{i=1} E_{Ri} \\
E_{c,ave} &= \pm E_{RC} \pm \frac{1}{n}\sum_{i=1} E_{Ri}
\end{aligned}
\tag{5.4}
$$

However, this approach also has some limitations. For example, it may be difficult or expensive to print and measure multiple parts in some cases, especially when dealing with complex or large-scale prints. The averaging process can also introduce additional errors or inaccuracies if the scan data are not perfectly aligned with the reference geometry represented by the part's nominal CAD model.

Due to the additive nature of the 3D printing process, layers at higher Z coordinates are necessarily printed later than layers with lower Z coordinates, creating a type of repetition in time and space following the build direction that can be leveraged for analyses. Following this hypothesis, a systematic deviation related to the extruder's position would be repeated from layer to layer. It would only be detectable by comparing the deviation at one point on a layer to another point on the same layer. In contrast, random errors occur only in a single layer. They should appear as horizontal streaks on the surface of the 3D printed part and in the deviation scalar field. See figure 5.1 for an example of a part with random deviations presenting themselves as horizontal lines. It would then be possible to observe a neighborhood around a point of interest in a single scan and determine the proportion of systematic deviation in the measured error. However, the complexity of the scan data, with its multidimensional nature and unorganized structure, requires extensive data manipulation and complex methods such as machine learning to accurately define the systematic deviation scalar fields.

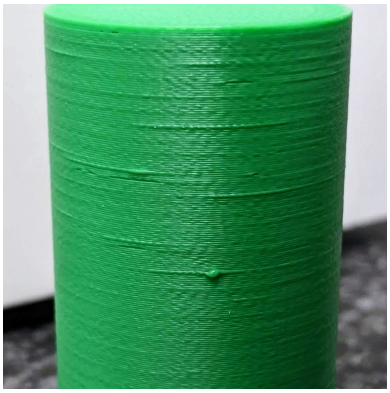

Figure 5.1 Random errors on the surface of a cylindrical 3D printed part occurring on a single layer. They often present themselves as horizontal streaks or bumps on the surface of the printed part.

We propose an algorithm to accurately identify the systematic deviations from a 3D scanned model of a single 3D printed part. This algorithm uses a Convolutional Neural Network on representative arrays of the neighboring deviations for each vertex. By training the compensation CNN on a dataset of scanned 3D printed parts, we aim to learn to compute the systematic deviation scalar field for a given 3D printed part. The deviation scalar field can then compensate the nominal 3D model to improve the accuracy of subsequent prints. An approach based on computing the systematic deviation scalar field would not be limited to a single geometry or machine but only limited by the breadth of the training dataset.

Our algorithm is divided into two modules: (1) data preprocessing and (2) Compensation Convolutional Neural Network. The data preprocessing module requires a 3D scanned model of the printed part and a surface mesh of the reference geometry. The module will produce a series of arrays that describe, in grid array form, the deviation at and around each vertex of the reference geometry. The Compensation Convolutional Neural Network module consists of the compensation CNN, which takes the arrays produced by the first module as inputs and produces a single value approximating the deviation amplitude at a vertex. This amplitude is then multiplied by the vertex's normal vector to create the compensation vector field.

Each algorithm module is discussed further in sections 5.2.1 and 5.2.2, respectively.

5.2.1 Data preprocessing

As discussed above, the unstructured and multidimensional data obtained by 3D scanning a 3D printed part are not conducive to analyses requiring positional information. Preprocessing the scan data in a generalized manner is necessary to assemble the deviations of a vertex

neighborhood in an accessible configuration.

For each vertex v_i on the reference geometry's surface mesh, a planar grid tangent to that vertex is created. The orientation vector V_{ori} is initially aligned with the z axis of the reference geometry. If the angle between the normal vector n_{vi} and the $X-Y$ plane exceeds 45°, V_{ori} is reoriented towards the centroid of the reference geometry from the vertex's position. The perpendicular vector V_{per} is computed by taking the cross product of V_{ori} and n_{vi} and is used to align the rows of the grid. Subsequently, the orientation vector V_{ori} is recomputed by taking the cross product of V_{per} and n_{vi}, aligning the columns of the grid. Figure 5.2 illustrates three example situations and demonstrates the orientation of the orientation vector and perpendicular vectors.

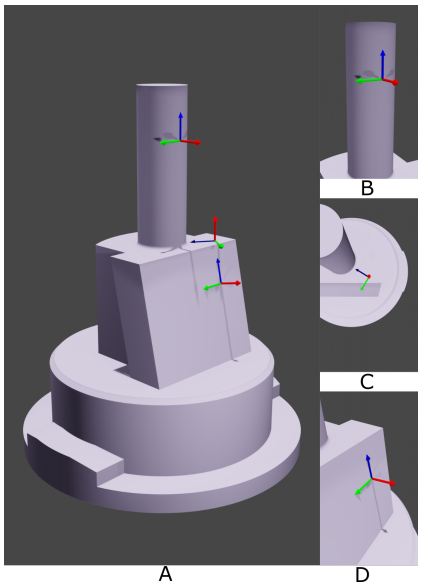

Figure 5.2 A) Examples of vectors on the reference geometry's surface mesh. Red arrows are the normal vector (n_{vi}) to the vertex of interest, green arrows are the perpendicular vectors (v_{per}), and blue arrows are the orientation vectors (v_{ori}). B) Example of vectors on cylinder. C) Example on a plane perpendicular to the Z-axis. D) Example on a sloped surface.

The position of the center of each grid cell p_{uv} is defined by equation 5.5 where u and v are the cell indices in the grid array, *shape* is the number of cells per row and column, and D is the size of each grid cell. Parameter D is driven by the point density of the surface mesh, as it determines the grid's ability to capture the necessary detail of the surface. Each cell must contain at least one vertex from the mesh to ensure proper representation. A size D that is too small would result in insufficient point inclusion per cell, compromising the grid's representativeness of the surface. Conversely, a size D that is too large would include too many points within each cell, reducing the cells' independence and the grid's ability to

accurately reflect local variations in the surface mesh. In contrast, The parameter *shape* is driven by the size of the typical part that will be analyzed using the grid arrays. We aim for the largest possible size to ensure that the CNN has the best receptive field and contextual information. However, if *shape* is too large, the grid arrays will contain many empty cells when analyzing the edges of the surface mesh. Therefore, *shape* must be carefully chosen to balance the receptive field and contextual information provided to the CNN with the need to minimize empty values in the grid arrays. This study defines the parameters *shape* as 20 cells per row and column and D as 0.2 mm.

$$p_{uv} = v_i - V_{per} D \left((u-1) - \frac{shape-1}{2} \right) - V_{ori} D \left((v-1) - \frac{shape-1}{2} \right) \quad (5.5)$$

Once the grid has been constructed, a ball query is applied to find all vertices of the reference mesh within a certain radius r_{ball} of each grid cell center p_{uv} using a K-d tree [193], a data structure used for organizing multidimensional data, facilitating efficient search operations by partitioning the space into smaller regions. This radius is related to the size D by this equation: $r_{ball} = \sqrt{2 * D^2}$. The deviation of each selected vertex is then averaged and stored in an accompanying array A_i. Vertices can be excluded from this average if the angle between the normal vector n_{vi} and the selected vertex's normal vector exceeds a threshold value. This study sets this threshold at 45° as a convenient angle threshold for simplifying computations while being an effective filter.

This process allows the creation of a set of grid arrays representing the neighborhood deviations of the printed part at each vertex of the reference geometry. The grid arrays A_i and the deviation at vertex v_i are then fed to the compensation CNN to determine the systematic deviation for vertex v_i. Figure 5.3 shows examples of this grid applied to different vertices of a mesh with various geometric features, with the deviation scalar field color-coded to show the deviation of the printed part from the reference geometry.

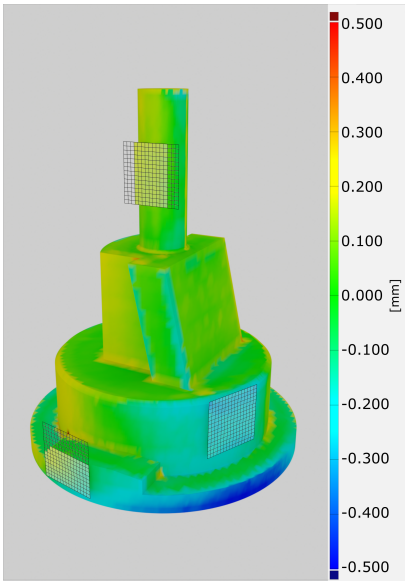

Figure 5.3 Illustration of grid arrays presented on a geometry with various geometric features.

5.2.2 Compensation Convolutional Neural Network

In this section, we present the development of a compensation CNN designed to interpret the deviation scalar represented in the 2D grid arrays prepared in the previous section. These grid arrays serve as input data, akin to grayscale images with dimensions of 20 x 20 pixels. Given the small size of the inputs, we adopted an architecture inspired by the Visual Geometry Group (VGGNet) [62], renowned for its use of small convolution filters (3x3) but with significantly increased depth. During our implementation, we found that a combination of 5x5 and 3x3 convolution filters yielded better performance after hyperparameter tuning. The final architecture of the compensation CNN, illustrated in Figure 5.4, incorporates Rectifier Linear Units (ReLUs) alongside each convolution filter to introduce non-linearity. Additionally, max-pooling layers were integrated to capture the most salient features while reducing computational complexity in subsequent layers. The number of channels C_1, C_2, C_3, and C_4 were also optimized, and the best-performing number of channels were 9, 17, 27, and 64, respectively.

Conventional CNN architectures such as VGGNet or the popular ResNet [194] are typically designed for classification tasks, wherein the network's objective is to categorize input data into predefined classes. To facilitate this task, these networks commonly employ a final fully connected layer with a size equal to the number of categories in the classification scheme. This layer consolidates the features extracted by the preceding convolutional layers and maps them to the respective class labels, enabling the network to make accurate predictions. In

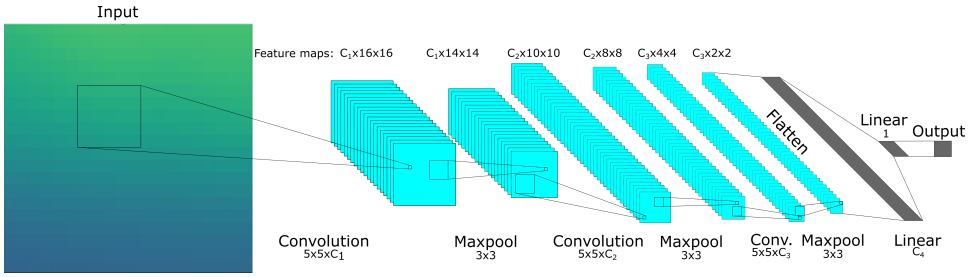

Figure 5.4 Architecture of the Compensation Convolutional Neural Network used to determine the systematic deviations present in the input image. Each intermediary level is a feature map, where the result of the previous layer is represented.

our study, the objective of the Compensation CNN differs from typical classification tasks; instead of categorizing input data into predefined classes, our CNN is tasked with regression, where the goal is to predict a continuous value. We have designed our CNN with two final fully connected layers to accommodate this task. The first layer performs the necessary non-linear computations on the extracted features. In contrast, the second layer consolidates these computed features into a single scalar value, serving as the output of the regression task. This output is then applied to the nominal geometry following equation 5.6, where v_i is the coordinate vector of the original vertex i, R_i is the output of the compensation CNN for the vertex i, n_{vi} is the normal vector of vertex i, and $v_{i,c}$ is the coordinate vector of the resulting compensated vertex i.

$$v_{i,c} = v_i - R_i \times n_{vi} \tag{5.6}$$

This process effectively adjusts the 3D model to account for the systematic deviation of the printed part from the reference geometry, resulting in a compensated 3D model that can be printed with improved geometric accuracy and no systematic deviations.

5.3 Experimental Methodology

We now present the methodology employed to prepare the dataset used to train the compensation CNN, the training process itself, and the evaluation of the compensation CNN.

5.3.1 Reference Geometry

The geometry selected for training the compensation CNN had to meet specific requirements: it must be quick to print, easy to analyze mathematically, and suitable for comparing the

proposed methodology to other 3D printing error compensation methods. Thus, a primary cylinder, a base, and a clocking feature were chosen. This configuration takes less than one hour to print, and the cylindrical portion of the point cloud can be analyzed mathematically to determine global deviation metrics such as RMS, mean, and standard deviation. Cylinders are also commonly used in other 3D printing error compensation methodologies, helping to reduce distortions induced by the heated build plate and minimizing misalignment errors. Figure 5.5 shows a rendered version of the chosen geometry.

The nominal CAD model and the files used for the printing and the inspection were prepared using the *CATIA V5* (Dassault Systèmes, Vélizy-Villacoublay, France) CAD software. The tessellated file used to prepare the printing process was created with a maximum permissible chord error of 0.001 mm between the nominal geometry and the lines of any triangle created by the tessellation process and a maximum edge length of 0.1 mm to obtain a regularly meshed tessellated file. Consequently, the file contained 340,925 points and 681,846 triangles and should be a negligible source of geometric deviations for the experiments. We focused exclusively on non-horizontal surfaces for training and evaluating the compensation CNN. This decision is driven by 3D printing's layer-wise nature, where even minor compensations on horizontal surfaces will necessarily cause a discrete layer change.

5.3.2 Dataset Collection

To assemble the dataset, a combination of four *Ultimaker 3* and four *Ultimaker S5* (Ultimaker, Geldermalsen, The Netherlands) 3D printers, shown in figure 5.6 were employed using 2.75 mm Poly-Lactic Acid (PLA) filament from *Polymaker* (Polymaker, Shanghai, China). The training dataset comprised 12 sets of five 3D printed parts of the chosen reference ge-

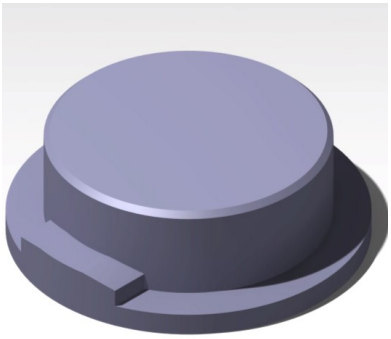

Figure 5.5 Render of the geometry selected for the training and evaluation of the compensation CNN.

ometry, totaling 60 3D printed parts. It's important to note that each *Ultimaker 3* produced two sets of parts. However, the first sets were printed much earlier than the second sets and should be considered independent due to potential differences in printer calibration or environmental conditions. Each part was printed using the default "fast" printing parameters from the *Cura* (Ultimaker, Geldermalsen, The Netherlands) slicing software. The key printing parameters are presented in table 5.1 and are the same for both 3D printer models.

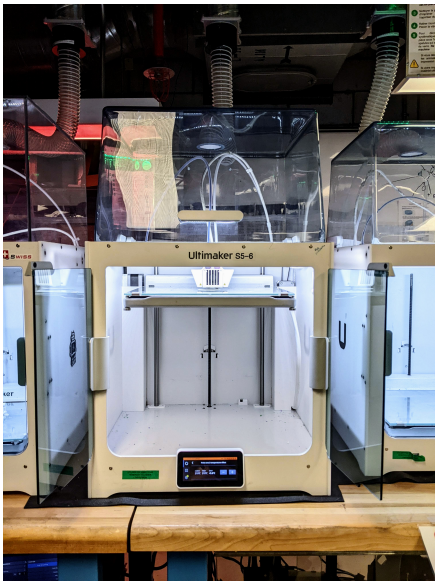

Figure 5.6 An Ultimaker S5 printing the chosen reference geometry.

Table 5.1 Printing parameters for the original and compensated parts on the Ultimaker 3 and Ultimaker S5.

Printing temperature	215 °C
Printing speed	70 mm/s
Cooling	100%
Support	None
Infill type	Triangles
Infill density	10%
Plate adhesion	None
Layer height	0.2 mm
Nozzle diameter	0.4 mm

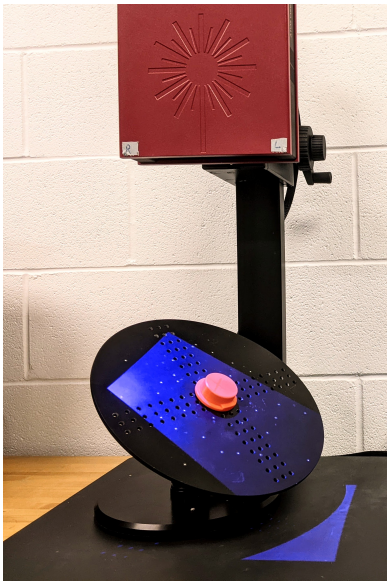

Figure 5.7 Atos core 200, 3D scanning the part.

The 3D scanner used to obtain the digitized version of the 3D printed part was an *Atos Core 200* (GOM, Braunschweig, Germany) shown in figure 5.7. This scanner was shown to attain a probe error in measuring form of 0.002 mm and a probe error in measuring size of 0.009 mm [149]. The *GOM Scan* software interpreted the images from the scanner to produce a tessellated 3D model representing the 3D printed parts using the high-resolution setting, resulting in a mesh of approximately 550,000 points at a density of roughly 30 $\frac{points}{mm^2}$. The alignment of the 3D scanned models to the nominal geometry was done using the *GOM Inspect* software.

5.3.3 Data Preprocessing and Compensation CNN training

The preprocessing of the training dataset has been implemented according to the methodology presented in section 5.2.1. This implementation was done using the Python 3.9 programming language using external libraries, namely Trimesh [150] for mesh processing and Libigl Python bindings [151] for the computation of the deviation scalar field. To enhance this study's stability and repeatability, we opted to utilize the vertices of the CAD tessellated geometry as measurement points and the 3D scan data as the reference for the computation of the deviation scalar field. Consequently, this approach ensures that a corresponding deviation value can be identified for each coordinate within every deviation scalar field. The grid arrays are then prepared using the previously computed deviation scalar field. The ground truths are also determined using the average deviation scalar field of each set of five printed

parts. The output of the data preprocessing for the training dataset is 3,439,800 groups of input grid arrays, deviation values, and ground truths.

Following the preparation of the training dataset, we implement the Compensation CNN using the PyTorch Machine Learning Framework [195] following the methodology presented in section 5.2.2. A portion of the training dataset is set aside to create the validation dataset to validate the training process. The training dataset will undergo backpropagation [57] to minimize the Mean Squared Error (MSE) [196] loss of the inference to the ground truths, while the validation dataset will not. By segregating these datasets, we mitigate the risk of overfitting [197], where the model would memorize training data patterns rather than learning meaningful relationships. Maintaining independence between the validation and training datasets ensures our CNN's robustness and generalization capability. An independent validation set is also an unbiased evaluator, providing insights into a model's performance on unseen data. We have segregated whole sets of printed parts from unique printers to ensure the validation dataset's independence. This results in a split training and validation dataset of 2,579,850 and 859,950 inputs, respectively.

The training process was done using an *NVIDIA TITAN Xp* (NVIDIA, Santa Clara, United States), a *Cuda* enabled Graphics Processing Unit (GPU). Using the *Weights & Biases* software [198], we could track various training and validation parameters to determine when the compensation CNN performed optimally on data it has not been trained on. We also used the hyper-parameter tuning tools of the *Weights & Biases* software to enable the CNN to better generalize on unseen data. Also, the ADAM optimizer [199] was used with $\beta_1 = 0.9$ and $\beta_2 = 0.999$ and an initial learning rate lr_0 of 1×10^{-3} with an exponential learning rate schedule [200] following equation 5.7, where n_{epoch} is the current epoch and $lr_{n_{epoch}}$ is the value of the learning rate at that epoch.

$$lr_{n_{epcoh}} = lr_0 \times 0.995^{n_{epoch}} \tag{5.7}$$

5.3.4 Compensation CNN evaluation

After successfully training the compensation CNN, it is necessary to evaluate its efficacy with brand-new data. In this study, we evaluate CNN by using a compensation process with a newly printed part. The same reference geometry was chosen for this evaluation to better showcase the compensation CNN's efficacy. We used an *Ultimaker 3* 3D printer with a significant time difference between the data collection and this evaluation, making the 3D printed part independent from the training dataset. The 3D scanner is the *Atos Core 200* presented earlier with its accompanying software, *GOM Scan* for the scan interpretation and

mesh creation, and *GOM Inspect*, for mesh alignment and metrological analysis.

5.4 Results

5.4.1 Compensation CNN Training

We now present the result of the training process for the compensation CNN. This training process spanned 500 epochs and lasted 3 hours. Figure 5.8 illustrates the progression of these losses throughout the training period. The presented loss metrics provided insights into the performance of the CNN, indicating its ability to approximate the average deviation scalar field. Optimal performance was observed when the validation loss reached its minimum, highlighting the model's effectiveness. Notably, at epoch 306, the CNN achieved its lowest validation loss, suggesting more robust generalization capabilities. The MSE validation loss was -5.24×10^{-6} mm^2 and the MSE training loss was -6.07×10^{-6} mm^2. The MSE loss presented here is the difference between the MSE loss of deviation at the current vertex and the MSE loss of the compensation CNN's output. It is negative because the CNN output is closer to the ground truth than the input deviation. However, after this epoch, an increase in the validation loss was noted, indicative of potential overfitting.

To test the efficacy of the compensation CNN in isolating systematic deviations within a deviation scalar field, we can visually compare the input deviation scalar field with the inferred output of the compensation CNN against the ground truth. From figure 5.9, we can observe that the inferred deviation scalar field is representative of the systematic deviations presented in the ground truth. It also eliminates other random deviations passed through the average deviation scalar field. In the subsequent section, we delve deeper into an analysis of a compensated 3D printed part utilizing the compensation CNN, aiming to evaluate the geometric improvements facilitated by this trained model.

5.4.2 Result of Compensation using the Convolutional Neural Network

To assess the effectiveness of the compensation CNN in identifying systematic deviations from a deviation scalar field, we compare the geometric accuracy of a compensated 3D printed part with the deviation scalar field of the sacrificial 3D printed part.

For this evaluation and to showcase the capability of the compensation CNN, we utilized the same geometry as previously presented on an *Ultimaker 3*, and sufficient time had elapsed between the collection of the training and validation datasets and this evaluation, resulting in significantly different deviation patterns due to the continued usage and maintenance of

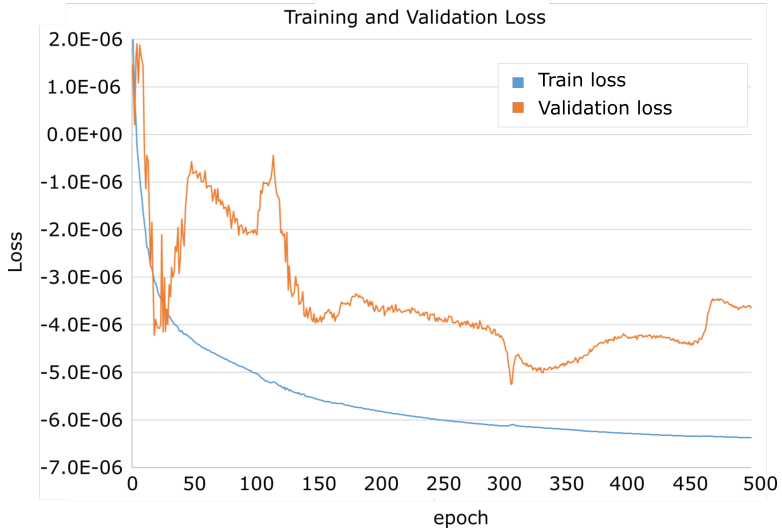

Figure 5.8 Training and validation loss of the Convolutional Neural Network.

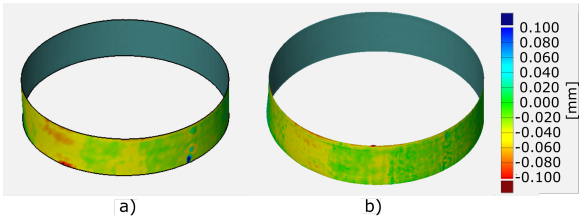

Figure 5.9 a) Colormap of the difference between the 3D scan of the cylindrical portion of a 3D printed part b) Colormap of the difference between the CNN output using that 3D scan and the corresponding ground truth.

the 3D printer. Subsequently, this part was scanned using the *Atos Core 200* 3D scanner, following the same procedure as previously presented. The acquired 3D scan data was then aligned with the nominal geometry to extract the deviation scalar field and processed using the preprocessing methodology outlined in Section 5.2.1. The output of the compensation CNN was used to compensate the nominal geometry, which was subsequently printed using the same machine and printing parameters as the sacrificial part.

The sacrificial and compensated parts used for the evaluation are depicted in Figure 5.10, with their deviation scalar fields represented as colormaps. A visual inspection reveals that most deviations have been eliminated.

A more meticulous observation of the compensated deviation scalar field of the printed part reinforces our initial hypothesis. Assuming systematic deviations have been successfully eliminated, the remaining errors should stem from random sources. These remaining random errors are observable on the surface of the compensated 3D printed part as horizontal patterns of deviation. Hence, horizontal deviations could serve as indicators for identifying random errors.

To further study the efficacy of the compensation CNN to reduce the geometric deviation of the compensated 3D printed part, a numerical analysis is presented in table 5.2. It demonstrates that the CNN compensation method leads to substantial improvements in geometric accuracy, as evidenced by reductions in mean absolute error, standard deviation, and improvements in cylindricity. The reduction in the standard deviation of the deviation scalar field holds particular significance in this evaluation, as it provides insights into the distribution of the errors in the compensated part. In that sense, it serves as a proxy to evaluate the filtration of random errors from the sacrificial part of the compensation process. Reinforcing this, the standard deviation of the CNN-compensated 3D printed part is 0.0173 mm, which closely aligns with the standard deviation of 0.020 mm obtained by Jadayel and Khameneifar [192] for the compensated part using the average deviation scalar field of five parts. Considering that the 3D printer and the 3D scanner inherently introduce random errors into

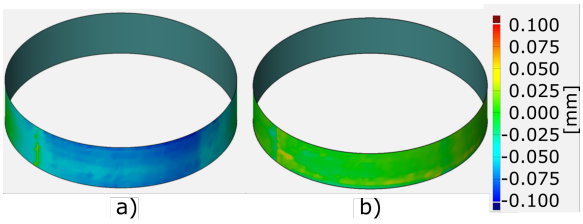

Figure 5.10 Deviation colormap of the cylindrical feature of the a) sacrificial and b) CNN compensated 3D printed part

the process, it is essential to acknowledge that some random errors cannot be eliminated. This similar result between the two experiments may suggest that we are approaching such a limit.

5.5 Discussion

This study proposes a compensation methodology to reduce geometric deviations in 3D printed parts. This methodology consists of the preprocessing algorithm and the Convolutional Neural Network. The first introduces an innovative approach to interpreting the deviation scalar field, or color map, by encoding not only the scalar values but also capturing the patterns and spatial correlations of the deviations across the surface of the geometry in a computer-readable format, allowing the following algorithms access to insights previously inaccessible. In essence, it transforms disorganized information into structured data. While alternative methods for organizing information exist, such as generating a parametric function to depict surface deviations on geometry, they fail to account for the original dataset's dimensionality and discrete nature.

This study's proposed preprocessing method creates 2D grid arrays of the deviation neighborhood, representing the deviation values associated with the vertices neighboring each vertex of the nominal geometry within a certain distance. It organizes the deviations measured on the surface of the 3D printed part as a 2D projection organized in a grid array representing the measured data in 3D while being entirely interpretable to a machine learning algorithm. It is also more accurate than other methods of organizing data because there is no interpolation or extrapolation in the output; only measured data is presented. This ensures that the information provided is precise and reliable without introducing inaccuracies through additional computations. These 2D grid arrays also encapsulate the local deviations and the spatial hierarchical structure of the deviation scalar field, allowing for the detailed analysis

Table 5.2 CNN compensation evaluation result

	Sacrificial Part Deviation Scalar Field (mm)	CNN Compensated Deviation Scalar Field (mm)	Geometric Deviation Improvement from CNN Compensation
Mean Absolute of Geometric Error	0.1275	0.0146	88.5%
Standard Deviation of Geometric Error	0.0694	0.0173	75.0%
Cylindricity	0.2382	0.0806	66.2%

of deviation patterns around a vertex.

The second algorithm presented in this work is specialized to detect patterns in an image or image-like data, in our case, a grid of values. After being trained on a large dataset, the compensation CNN is specially optimized to detect patterns of systematic deviations and approximate the proportion of the deviation that is random vs systematic. Thanks to the preprocessing step, the compensation CNN can leverage the spatial hierarchical structure of the deviations in the grid arrays without requiring knowledge of the underlying geometry. The proposed methodology presents distinct advantages, notably its generalized and machine-agnostic approach. Although the generalization is not thoroughly demonstrated in this work, NNs and CNNs have consistently shown a remarkable capacity for generalization when trained on extensive datasets [201]. In addition, the success of the compensation CNN on a limited dataset for training and validation demonstrates the efficacy of the compensation methodology. To obtain a generalized compensation CNN, popular image classification CNNs like AlexNet and VGGNet are pre-trained using datasets like ImageNet holding more than 1.2 million images [183] and Trained on specific datasets containing millions of images [62]. For our implementation, the precise number of independent data points required remains uncertain and would likely depend on factors such as the complexity of the CNN model and the desired level of performance. Given the resource limitations of this study, a thorough investigation into the optimal dataset size is not considered. However, this remains an important avenue for future research. These data points would consist of sets of 3D scanned 3D printed parts of different geometry produced from different machines using various sets of printing parameters. On the other hand, a production team that is required to scan all produced 3D printed parts for quality assurance purposes could already have all the necessary data to train the compensation CNN.

Assuming successful training leads to a generalized model, no additional training, work, or adjustment would be needed to obtain a compensated nominal geometry. Only a single sacrificial part per machine and printing parameter would be necessary to compensate the nominal model for a production run. In contrast, previous methodologies necessitated a more labor-intensive approach, especially with increasing geometric complexity. For instance, the parametric function required to model the deviations on a 3D free-form shape is more complex than the parametric function necessary to model the deviations on a primitive geometry. Another method of compensating a nominal geometry to reduce systematic deviations necessitated five sacrificial parts for every machine and sets of printing parameters [192]. The method proposed in this paper reduces wasted time, material, and cost.

Future work would be required in the preprocessing algorithm to resolve the missing data

issue when no valid vertex of the nominal geometry is present to occupy a cell in the grid array. As the CNN is a purely mathematical tool, a placeholder value has to be inserted in the cell, as it is impossible to input an empty cell in a grid array. This placeholder can still affect the perception of the CNN, even if pooling layers and masks were implemented.

5.6 Conclusions

The proposed method of training a compensation Convolutional Neural Network to produce a deviation scalar field representing the systematic deviation of a 3D printed part by analyzing grid arrays of the projected original deviation scalar field obtained by scanning a sacrificial 3D printed part was successfully demonstrated and shown to improve the geometric accuracy of subsequently printed parts when the nominal shape is compensated using the inverse of systematic deviations. The compensated part used to validate the compensation algorithm displayed a mean average error improvement of 88.5% and a standard improvement of 75% over the non-compensated part. By training the compensation CNN to recognize and quantify the systematic deviations in the deviation patterns represented in the grid arrays, we were able to reduce the importance of random deviations in the sacrificial part's deviation scalar field and, through this approach, reduce the impact of random deviations from the sacrificial part on the compensated part, allowing the cylindricity of the compensated part to be improved by 66%. This improvement can allow a lower-priced 3D printer to compete with high-end machines or allow for tighter tolerances with FFF machines. While our study provides valuable insights into the effectiveness of the proposed method for improving the geometric accuracy of 3D printed parts, future work would expand the datasets to encompass a broader range of geometries and printing platforms.

Acknowledgements The authors would like to acknowledge the financial support of the Natural Sciences and Engineering Research Council of Canada (NSERC) through the Discovery Grant RGPIN-2017-06922.

Statements and Declarations The authors have no competing interests to declare that are relevant to the content of this article.

CHAPTER 6 ARTICLE III: STRUCTURED-LIGHT 3D SCANNING PERFORMANCE IN OFFLINE AND IN-PROCESS MEASUREMENT OF 3D PRINTED PARTS

Authors Moustapha Jadayel, Farbod Khameneifar

Accepted for publication in Procedia CIRP on July 12 th 2023.

Abstract This paper presents a geometric analysis comparison of structured-light 3D scanners against coordinate measuring machines (CMMs) in measuring 3D printed plastic parts. The resulting geometric analysis of a 3D printed part measured with a contact probe on a CMM and measured with a structured light 3D scanner is presented, along with an error analysis that includes a statistical comparison of the measured geometric deviation. This analysis is then used to determine if structured-light 3D scanners are reliable enough to perform a GD&T analysis of specific features. This paper also presents the results of in-process 3D scanning and compares them to offline 3D scanning to determine the suitability of in-process 3D scanning for comprehensive analysis of geometric deviation and GD&T features.

6.1 Introduction

Additive manufacturing (AM), or 3D printing, has revolutionized the production of complex and intricate parts across various industries [202]. While AM offers numerous benefits, including faster prototyping, reduced material waste, and increased design freedom, it also poses unique challenges regarding quality control [203]. Traditional methods for measuring the accuracy of manufactured parts, such as coordinate measuring machines (CMMs), are time-consuming and costly, reducing the efficiency of rapid prototyping or low-volume production. As a result, CMMs may not be adequate to analyze the geometry of a 3D printed part promptly, especially for parts with intricate features and shapes.

Structured-light 3D scanning is a promising alternative for measuring 3D printed parts, offering faster results than traditional methods [204]. In structured-light 3D scanning, a pattern of light is projected on the surface of an object, and two cameras capture the distortion at a calibrated distance and angle between them. The difference in the captured pattern is used to reconstruct the object's geometry [36]. The result of 3D scanning is a disorganized point cloud of the surface of the measured part, which can then be used for geometric inspection.

Without a recognized standard procedure to compare the different technologies, several researchers have developed methods and artifacts to evaluate the metrological performance of structured light 3D scanning [44, 47, 205]. Additionally, 3D scanner manufacturers also create their own evaluation artifacts that the end-user can use to verify the quality of their equipment.

This scan-based inspection result can also be used to compensate the geometry of parts to improve their geometric accuracy [192]. It is also possible to optimize the quality control process for speed even more by integrating measuring sensors in the 3D printing process [206, 207].

In this paper, we present a measurement comparison of a 3D printed Polylactic Acid (PLA) part using a CMM and a structured-Light 3D scanner. We also present an in-process 3D scanning measurement and evaluate the variation of the measurements at different layers of the printing process. This study investigates the metrological performance of structured-light 3D scanning for the geometric inspection of 3D printed parts. By comparing the results of in-process and offline 3D scanning and CMM measurement, we aim to provide insights into the accuracy and reliability of offline and in-process structured-light 3D scanning as a quality control tool for AM.

6.2 Methodology

6.2.1 Part Fabrication

The part used in this study is a plate with 16 spheres arranged in a diamond pattern. A feature to help determine the part's orientation is present on the corner used as the origin of the measurement coordinate system. A representation of the part used is presented in Figure 6.1. Spheres were chosen as the measured features due to their simple geometry, which is amenable to numerical analysis. The overall size of the part is 75 mm x 75 mm in length and width. The plate is 5 mm thick, and the radius of the spheres is 3.75 mm. The size is representative of the usual parts printed by a desktop 3D printer.

The part is printed, with white PLA, on a Prusa i3 MK3S (Prusa, Prague, Czech Republic.) modified to allow for in-process 3D scanning. The geometry was sliced using the Cura slicing software with default fast parameters. The main parameters of these settings are presented in Table 6.1. The accuracy reported by the printer's manufacturer is 0.1 mm on the Z-axis and 0.3 mm on X and Y axes [208].

The same part is measured by CMM, offline 3D scanning, and in-process 3D scanning, where the part is scanned at every five layers during the printing process. More details on the

in-process 3D scanning will be presented in section 6.2.4.

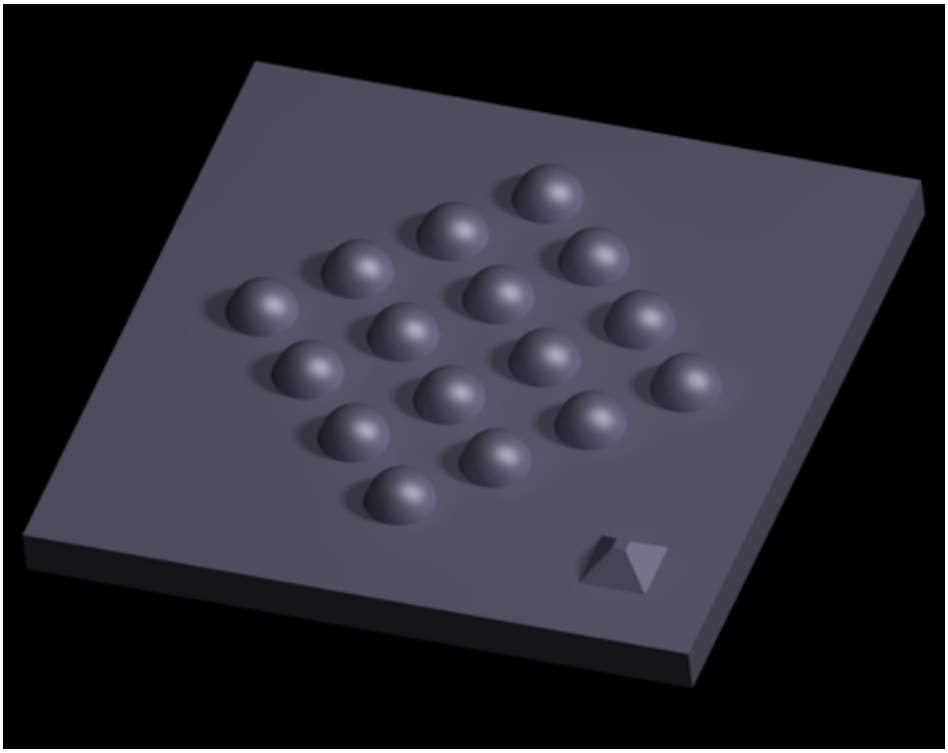

Figure 6.1 3D model of the ball plate used for the analysis.

6.2.2 CMM Measurement

The part is measured with a Coordinate Measuring Machine (CMM) following the printing and in-process scanning. The machine used for this study is a Mitutoyo Legex 960 (Mitutoyo, Kawasaki, Japan) equipped with a TP7M probe (Renishaw, Wotton-under-Edge, United Kingdom). The length of the stylus is 20 mm, and the radius of the tip is 2 mm. This measurement dataset offers a theoretically reliable and precise measurement of the printed

Table 6.1 Printing parameters of the measured part.

Printing parameters	Value
Printing temperature	200 °C
Build plate temperature	60 °C
Layer height	0.2 mm
Infill density	20 %
Printing speed	60 mm/s

part. For this reason, it is used as a reference for the other measurements. Each sphere is measured using 51 measurement points covering the whole surface of each sphere for a total of 816 measurement points.

Next, the measurement dataset is processed using a Python script. This script separates the dataset into 16 groups according to what feature it measures and fits a sphere to each. To eliminate any registration errors due to the origin being measured by the CMM on the part, an additional registration transformation is applied by using Procrustes' analysis [209] with the center of the fitted spheres and the nominal sphere centers from the CAD model.

6.2.3 Offline 3D Scanning

The printed part is then scanned using an optical structured light 3D scanner. This study uses the Atos Core 200 (GOM, Braunschweig, Germany) with GOM Scan, its data acquisition software. The part is installed rigidly on a manual turntable with scan markers, easily detectable by the 3D scanner. The part is rotated and scanned to capture the geometry from all sides. Thanks to the markers installed on the turntable, the software can accurately stitch multiple scans to form the complete point cloud of the entire part. Figure 6.2 shows the part on the turntable scanned with the Atos Core 200 3D scanner.

The resulting point cloud consists of approximately 525,000 points with a resolution of around 72.5 points/mm2. The data was then exported to GOM Inspect for registration with the nominal geometry. A Python script then isolates the points related to the spheres from the rest of the point cloud and fits spheres to them.

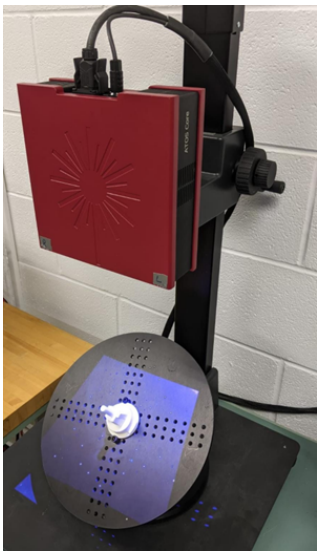

Figure 6.2 Offline 3D scanning setup.

6.2.4 In-Process 3D Scanning

The process of scanning the part while it is being printed required modifications to the 3D printer. The Prusa i3 MK3S was modified to include a flat bearing and a pulley under the build plate to allow precise and smooth rotation. A NEMA 17 stepper motor and an Arduino Uno (Arduino, Turin, Italy) microcontroller were also added to control the rotation according to serial commands sent from the controlling computer. The 3D scanner used for in-process 3D scanning is the Atos Core 200, which is used for offline 3D scanning.

Every five layers, the printer receives a stop command and moves the print head to a position on the edge of the scanning volume, and the build plate moves to the center of the scanning volume. Then, the build plate and everything on it are scanned multiple times in different orientations to complete 360 degrees of coverage. Scan markers are placed on the print bed for the 3D scanner software to compute the exact orientation and position of the bed. Figure 6.3 shows the modified 3D printer in its scanning position.

The output of the in-process 3D scan is eight point clouds made of 312,000 points for the first scanned layer to 416,000 points for the last scanned layer. Each scanned layer captures the outside geometry and the visible infill at that layer. A Python script filters the extraneous points in the point cloud, isolates the points corresponding to each sphere and computes a fitted sphere to each.

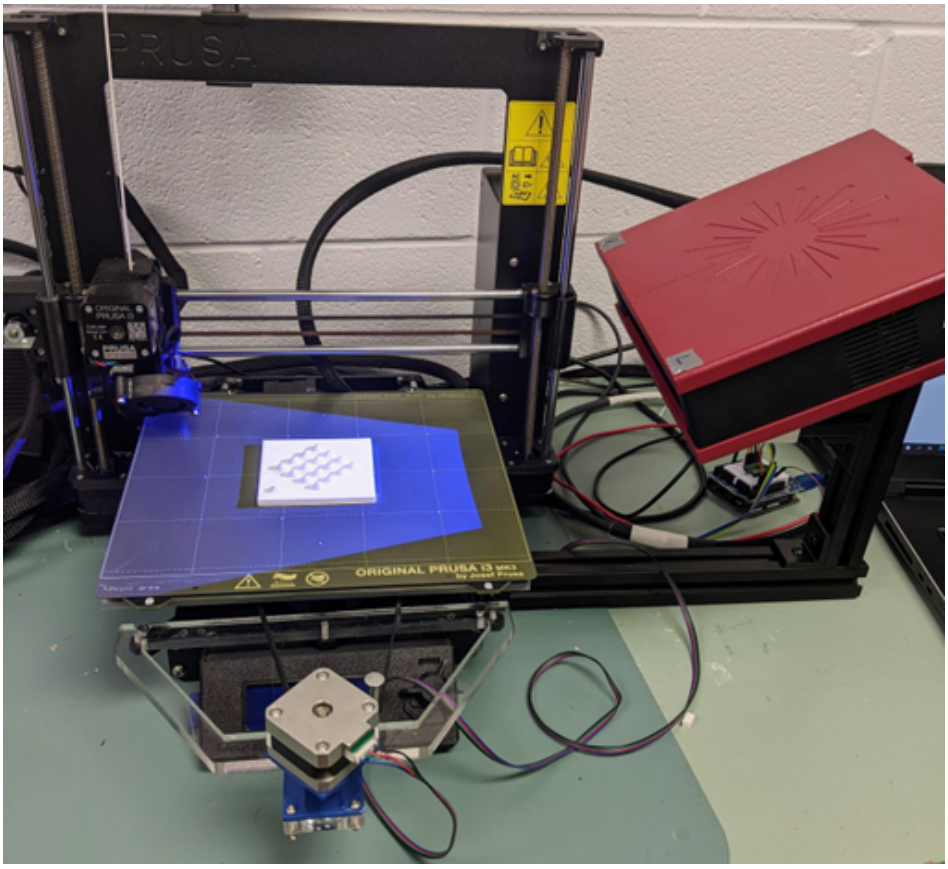

Figure 6.3 In-process 3D scanning setup in the scanning position.

6.3 Offline 3D Scan vs CMM Analysis

When analyzing the offline 3D scan dataset, the CMM measurement is taken as the reference geometry, as it offers an accurate representation of the printed part, which we use to characterize the measurement errors produced by the 3D scanner. This analysis focuses on the error in distance measurement, the error in size measurement and the error in form measurement.

6.3.1 Error in Distance Measurement

The distance between the center of each two fitted spheres is measured, and the error in distance measurement is the difference between the distance measured with the 3D scanner data and the distance measured with the CMM data. There are $\frac{n(n-1)}{2}$ unique combinations in a set of n elements; with 16 spheres, we obtain 120 distance values. Equation 6.1 demonstrates the error in distance measurement e^{uv}_{dist} as defined in this study.

$$e^{uv}_{dist} = ||c^u_{Scan} - c^v_{Scan}|| - ||c^u_{CMM} - c^v_{CMM}|| \tag{6.1}$$

Where c^u_{Scan} and c^v_{Scan} are the center of fitted sphere u and v from the scan data and c^u_{CMM} and c^v_{CMM} is the center of fitted sphere u and v from the CMM data. Figure 6.4 shows the measurement errors for each nominal distance. The average error is 0.017 mm with a standard deviation of 0.029 mm. The Root Mean Square (RMS) value is also calculated to be 0.033 mm.

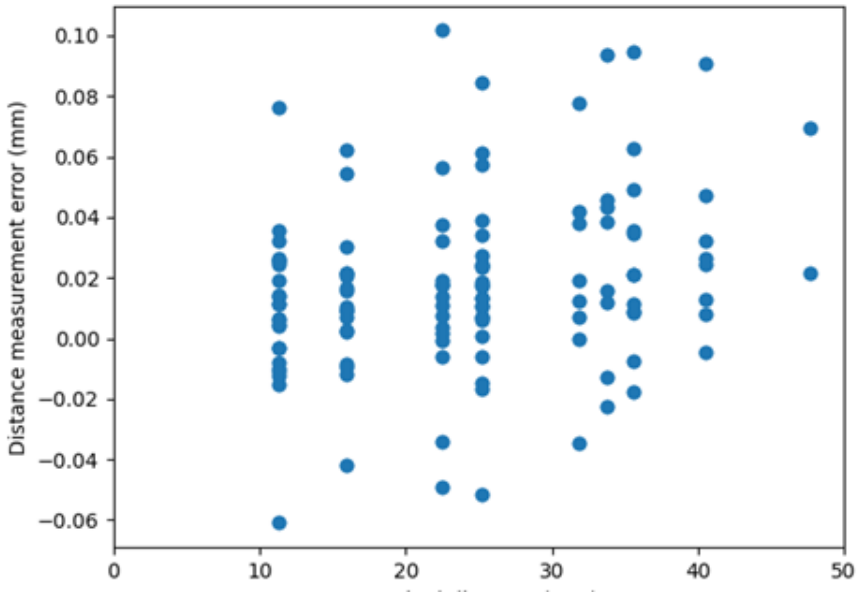

Figure 6.4 Error in distance measurement.

6.3.2 Error in Size Measurement

The size measurement is the radius of the fitted sphere and the error in size measurement is the difference between the size measured with the 3D scanner and the size measured with the CMM. The error in size measurement e^i_{size} is computed using equation 6.2.

$$e^i_{size} = r^i_{scan} - r^i_{CMM} \tag{6.2}$$

Where r^i_{scan} is the radius of fitted sphere i in the scan dataset and r^i_{CMM} is the radius of fitted sphere i in the CMM dataset. The average error in size measurement is -0.095 mm with a standard deviation of 0.030 mm. The maximum error calculated is -0.159 mm, and the minimum error is -0.053 mm.

6.3.3 Error in Form Measurement

The form measurement is represented by the fitted residuals of the fitted spheres. The error in form measurement is taken as the difference of the average of fitted residuals between each corresponding spheres from the scan and the CMM dataset. Equation 6.3 demonstrates the fitted residual $form^i_{scan}$ of sphere i in the scan dataset. The fitted residual $form^i_{CMM}$ is calculated with the same equation using the CMM dataset instead. Equation 6.4 shows the error in form measurement e^i_{form} of sphere i.

The distinction between the size measurement and the form measurement is that the latter offers information on how well the measured points form a sphere while the former informs us on what sphere represents the given points optimally.

$$form^i_{scan} = \frac{\Sigma_j^{n_{scan}} ||p^{j,i}_{Scan} - c^i_{Scan}||}{n^i_{Scan}} - r_i \tag{6.3}$$

$$e^i_{form} = form^i_{scan} - form^i_{CMM} \tag{6.4}$$

Where $p^{j,i}_{Scan}$ is the position of point j of sphere i in the scan dataset, c^i_{Scan} is the position of the center of fitted sphere i, n^i_{scan} is the number of points corresponding to sphere i in the scan dataset and r_i is the radius of fitted sphere i.

The error in form measurement for the printed part is, on average 0.010 mm and its standard deviation is 0.008 mm. The RMS for this error is 0.099 mm. After analyzing the data, it appears that the unusually high value for the RMS is the result of an outlier error on sphere 14. The form measurement error for this outlier is 0.039 mm. However, by excluding the error from this fitted sphere, we were able to obtain a new average of 0.008 mm, a standard deviation of 0.003 mm, and an RMS value of 0.008 mm. Upon further inspection, it seems that sphere 14 has a blob of solidified material that went undetected by the CMM.

6.4 In-Process 3D Scan vs Offline 3D Scan Analysis

In this section, the in-process 3D scan dataset is compared to the offline 3D scan of the same part. The offline scan is chosen as the reference data to determine if in-process 3D scanning is reliable to inform decisions on the accuracy of the 3D printed part before it is finished. As the in-process scan occurs at multiple layers, the analysis is conducted on multiple point clouds obtained at different layers, and their trends are compared to the offline scan.

6.4.1 Error in Distance Measurement

The error in distance measurement is computed similarly to equation 6.1, with the difference that the offline 3D scanner dataset is now the reference, taking the place of the CMM dataset. Also, the in-process 3D scanner dataset is the dataset to analyze, instead of the scan dataset from Equation 6.1.

Theoretically, the position of the spheres, and the distance between them, should not change between each measurement. In reality, the computed position of the fitted spheres changes from one scanned layer to another because of imperfections on the surface of the spheres which affect the computation of the fitted spheres. Additionally, imperfection on early layers of the part has a proportionally more important effect on the fitted spheres. Figures 6.5 and 6.6 show the trend of the error of the distance between spheres and it suggests that before layer 31 the data is not reliable enough to determine the geometric quality of the printed part.

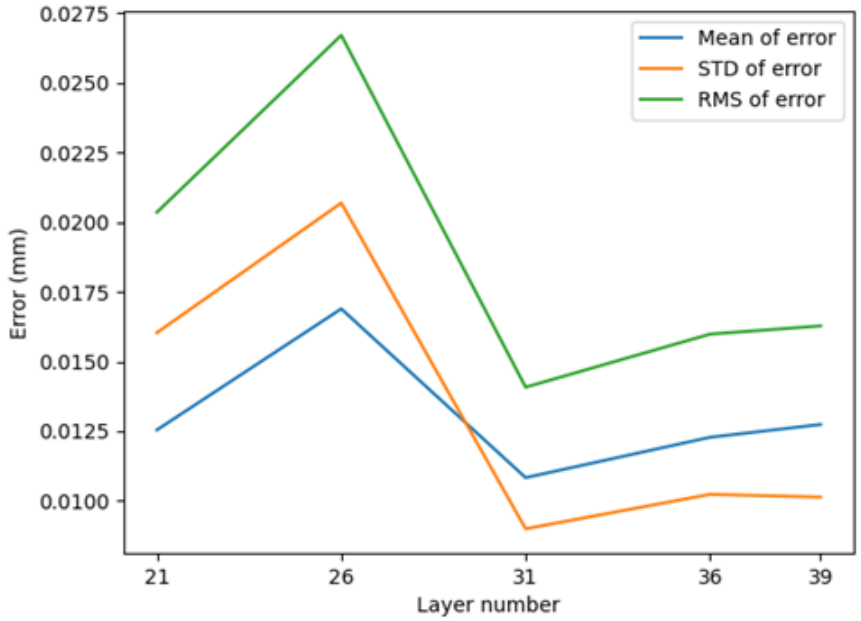

Figure 6.5 Mean, standard deviation (STD) and Root mean square (RMS) of the distance measurement error on scanned layers.

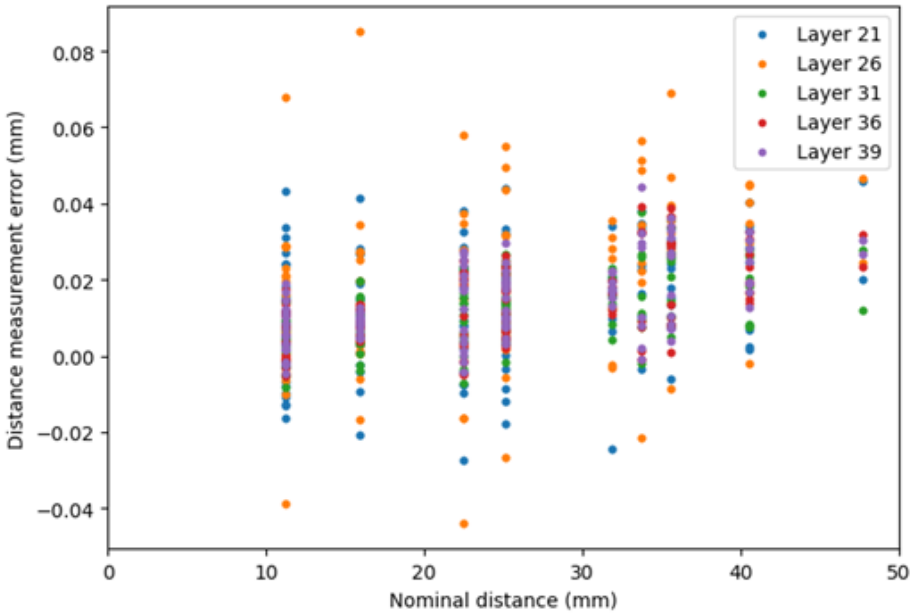

Figure 6.6 Error in distance measurement at each scanned layer.

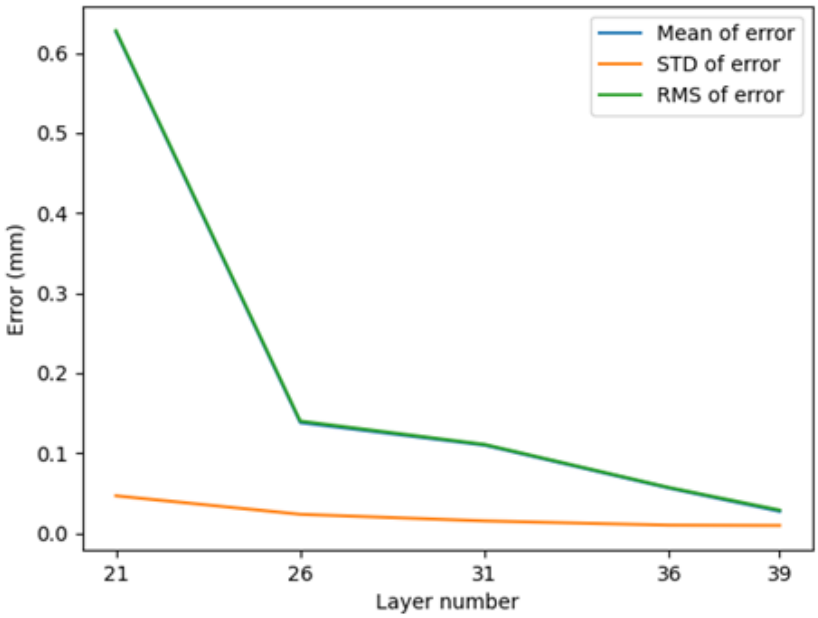

Figure 6.7 Mean, Standard deviation (STD) and Root mean square (RMS) of the size measurement error on scanned layers. Note that the mean and RMS curves appear superimposed due to the scale of the chart being much bigger than the difference between the two curves.

6.4.2 Error in Size Measurement

The size measurement error is analyzed to determine the accuracy of the 3D scanner when measuring size features on a printed part. Equation 6.2 is adapted by using the offline 3D scan as the reference data instead of the CMM data and the in-process 3D scan as the data to evaluate instead of the offline 3D scan data. The adapted equation is then used to compute the error in size measurement between the in-process 3D scanning and the offline 3D scanning.

For the in-process 3D scanning, the variation of the computed error in size measurement demonstrates that scans from early layers are most impacted by missing data and geometric deviation from the printer, as they disproportionately affect the results.

Figure 6.7 displays the progress of the error in size measurement. It is clear from this figure that the error is indeed greater in the first scanned layers than in the last two layers. In addition, we can notice that the standard deviation of the error is much smaller than the mean and RMS, which shows that there may be a systematic error common in all spheres.

6.4.3 Error in Form Measurement

The error in form measurement is important to analyze as it can help to determine if the form measurement is reliable. Equations 6.3 and 6.4 are adapted in the same manner than the other two equations, by replacing the offline 3D scan as the reference data instead of the CMM data and the in-process 3D scan as the data to evaluate instead of the offline 3D scan data. Adapted equations 6.3 and 6.4 are then used for the error computation with the offline 3D scan as the reference measurement and the in-process 3D scan as the measurement to analyze. This analysis will also be highly influenced by missing data and printing errors causing it to be unreliable in early layers.

Figure 6.8 shows the evolution of the form error across the scanned layer. From the figure, we can observe that the layers before layer 36 have a much higher error in form measurement than the last couple of layers. That is what we expect from having more data points on which we fit spheres.

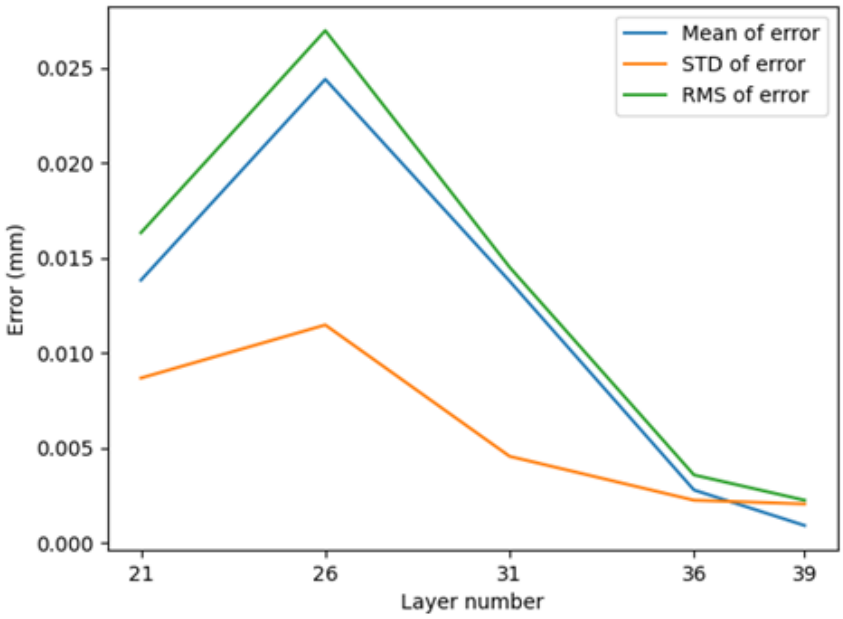

Figure 6.8 Mean, standard deviation (STD) and Root mean square (RMS) of the form measurement error on scanned layers.

6.5 Discussion

It is clear from the results of the offline scan to CMM analysis, shown as a summary in table 6.2, that the 3D scanner can accurately capture the geometric quality of a 3D printed part. However, further assessment is required to define the measurement uncertainty of the 3D scanner data. Notably, the mean error in size measurement is higher than the other measurement errors. This higher value is likely due to a previously undetected systematic error in the measurement of the 3D scanner.

On the other hand, CMMs can only measure at predetermined points on the surface of the part and can easily miss errors on the part due to the low number of measurement points. This is what we see in section 6.4.3, where a blob of extra material was present on the surface of the sphere. This blob was accurately captured by the 3D scanner, but not the CMM. On the other hand, if the CMM had detected it, it would have had a more significant impact on the quality of the measurement due to the relatively high impact of each measurement point.

On the comparison of the in-process 3D scanning and the offline 3D scanning, we see that all errors are high in early layers, meaning the scan data is not reliable to use as an early prediction of final geometric deviation. Nevertheless, using statistical analyses, could deter-

mine if a certain tolerance on a scanned feature would not be respected early in the printing process, reducing wasted material and time. However, a custom statistical model may be required for each feature type. A machine learning model could also be used to compute the probability of a tolerance being respected.

Additionally, we can compare the measurement errors of the last layer of the in-process 3D scan to the offline 3D scan measurement errors, as the scanned part is finished in both measurements. This comparison shows that the distance, size, and form errors are small relative to earlier layers, most likely due to thermal deformation. It could also be attributed to the error of repeatability of the 3D scanner. Furthermore, the offline 3D scanned part was carefully scanned to capture all sides of all spheres and leave as few holes as possible. That is something that would not be possible to guarantee for the in-process 3D scan. This fact could have decreased the quality of the in-process measurement.

6.6 Conclusion

This study shows that the 3D scanner can accurately capture the geometric accuracy of the 3D printed part and that the 3D scanner has the significant advantage of being able to capture the entirety of the surface of the geometry without requiring a significant amount of time. However, additional investigation is needed to determine the measurement uncertainty of 3D scan data.

For in-process 3D scanning, the automation of the scanning process before being removed from the 3D printer brings the same advantages as offline 3D scanning in addition to the possibility of adjusting the printing process by compensation. Despite that, more extensive research is needed to refine the acquired data to obtain similar results to offline 3D scanning.

Finally, further research should be conducted to improve the efficiency of in-process 3D scanning. Also, more quality control methods could be integrated with the proposed setup to develop a complete analysis of the geometric accuracy of the printed part and other properties that could be verified, i.e., porosity, surface roughness, or the quality of the infill.

Table 6.2 Summary of the measurement error of the offline 3D scanner to CMM analysis.

Measurement type	Mean error (mm)	Standard deviation of error (mm)	Root Mean Square of error (mm)
Distance	0.017	0.029	0.033
Size	-0.095	0.030	0.100
Form	0.010	0.008	0.099

CHAPTER 7 GENERAL DISCUSSION

7.1 Summary of findings

In the scientific literature reviewed in Chapter 2, it is evident that only a few methodologies to improve 3D printers' geometric accuracy performance are tailored to utilize dense deviation scalar fields obtained from a 3D scanner. Moreover, the methods incorporating such data often do not evaluate how best to use the data. As presented in chapter 4, using the raw deviation scalar field to compensate the nominal geometry's surface mesh is not the best method. Indeed, the first contribution of this research work is that we have demonstrated that the raw deviation scalar field includes random and systematic deviations, and the optimal compensation method is to apply the inverse of the systematic deviation scalar field on the surface mesh of the nominal geometry. The systematic deviations vary across machines, and given their complex interplay of thermomechanical and kinematic effects, no known method exists in the scientific literature to model them. The average deviation scalar field of five printed parts of the same geometry using a single machine, presented in chapter 4, adequately approximated the systematic deviation scalar field of a part of that particular geometry printed on that machine. Applying the inverse average deviation vector field to the nominal surface mesh showed a notable enhancement, with the MAE seeing a 55% improvement, the standard deviation seeing a 65% improvement, and the 99th percentile of absolute error sees an improvement of 68%. This study is intended to prove the concept and presents two significant limitations. The first limitation is the number of sacrificial parts required to obtain an average deviation vector field, which can be prohibitively expensive if working with costly materials or machines. The registration of multiple sacrificial parts is also a limiting factor in this study, as the different scan data need to be aligned with the nominal geometry, each scan will have different alignment errors. These errors will affect the deviation field and the average deviation field. As it would not be consistent from part to part, the alignment errors would be reduced in the average deviation field but would increase the proportion of random errors. The second limitation is that the approximated systematic deviation vector field relates only to a single geometry and machine's state at a time. For any new geometry, material, or variation in the printing process or measurements, five new sacrificial parts must be printed, scanned, and averaged to compute the new average deviation field. One of the major advantages of 3D printing is its flexibility and ability to produce different geometries without necessitating different setups, so requiring five sacrificial parts is antithetical to the technology.

The study presented in chapter 5 developed on the first contribution by proposing to use an ML model to interpret better the deviations scalar field of a 3D printed part obtained using a structured light 3D scanner. The ML model can quantify systematic deviations visible on the measurements of the printed part by creating images of the deviation scalar field surrounding each point of the nominal surface mesh. The CNN used a series of learnable filters and Max-Pool layers to interpret the deviation values in the neighborhood of each point, recognizing patterns that would be telltale signs of systematic deviations. This CNN was trained using a dataset consisting of sets of 3D printed parts. Each set within the training dataset was produced using different 3D printers, ensuring variability and robustness in the training process. Their corresponding average deviation scalar field, approximating the systematic deviations, was used as ground truths. Including different 3D printers allows the CNN to recognize general systematic deviation patterns in local deviation neighborhoods and discourages the network from learning a deviation pattern of a single 3D printer. This research's second significant scientific contribution demonstrates the CNN's ability to approximate the average deviation scalar field using a single deviation scalar field. This capability indicates the presence of recurring patterns within the local deviation neighborhood, which are consistent across FFF 3D printers. It also suggests the potential to approximate the systematic deviation scalar field and use this approximation to improve the geometric accuracy of subsequent parts by compensating the surface mesh of the nominal geometry. In the study presented in chapter 5, we demonstrated that the original geometry compensated by the inverse of the systematic scalar field generated by the compensation CNN produced a part with an MAE improved by 88.5%, the standard deviation seeing a 75% improvement, and the cylindricity sees an improvement of 66.2%. This improvement in geometrical accuracy comes at the cost of a single sacrificial 3D printed part, reducing material and time wasted by 80% from our first proposed method. The presented solution also has limitations that impede its performance. As noted in the study, the absence of data in some pixels created by the preprocessing algorithm harms the CNN's performance. No methods were found in the literature to handle missing data in images inputted to a CNN other than simply filling empty pixels with a value that is not in the expected domain of the image. Another limitation, typical for many ML solution implementations, is the data required for a successful training process. Indeed, thousands of independent observations would be necessary, which is well outside the scope of this research.

The last scientific contribution, presented in the conference paper at the CIRP ICME '23 conference, relates to in-process measurements of the FFF 3D printing process. The conference paper presents a 3D printing in-process 3D scanning setup that captures the geometric deviations of a part in the middle of the printing process. This setup allowed us to examine

the evolution of the dimensions throughout the printing process. We concluded that the deviations in all metrics were higher earlier in the printing process and seemed to settle at the end. In all likelihood, each layer is affected by the next layer, and a cycle of cooling, reheating, contracting, and dilating is the reason for this behavior. This conclusion finally demonstrated that more work would be required to obtain actionable measurements in-process for the FFF 3D printing process.

7.2 Recommendation for future work

Recommendations for extensions to the presented work can be separated into incremental improvements, focusing on the process's limitations as explained in the previous section, and paradigm-shifting enhancements, which would present new methodologies than those presented in this investigation.

Collecting more data from various FFF 3D printers printing various geometries in sets to obtain the average deviation scalar field would be incremental work that would allow CNN to develop its ability to extract systematic deviation patterns from local deviation neighborhood images further. Similar to this improvement, optimizing the CNN's architecture based on the enlarged dataset would enable it to perform better. Notably, the small image size of 20×20 limits the context available to the CNN and the abstraction capability of each neuron. Increasing it is not negligible, as it would worsen the missing data problem. The missing data problem is another facet that warrants more work. The ability to handle missing data intelligently, or at the very least in a manner that would not be detrimental to performance, would be an exciting avenue for future work, not only in the context of this research but also in the case of other similar problems of CNN computation.

Another exciting opportunity that has been identified in the pursuit of this investigation is the study of how different materials, printing process parameters, and different printing processes altogether. Indeed, because the material's heating and cooling are one of the causes for systematic deviations, systematic deviations would present themselves differently in the raw deviation field. If the differences are notable, it might be that a separate CNN would be needed to interpret the deviation scalar field to integrate the material selection in the computation of the systematic deviation scalar field. Integrating this knowledge could direct the research into new directions, making it more capable of inferring systematic deviations from a deviation scalar field.

Many possible future works could be paradigm-shifting in the in-process determination of systematic deviations. Understanding the deviation trends in-process would permit the cre-

ation of a deviation model according to the status of the printing process. This deviation model could then be used to adjust the scan data obtained during printing to predict the deviation at the end and compensate based on the computed systematic deviation scalar field using the compensation CNN.

CHAPTER 8 CONCLUSION

This thesis presents the current state of geometric accuracy evaluation, control, and improvement of FFF 3D printing. As an active field of research, various solutions and opportunities are continuously being explored. While numerous methodologies are documented in the scientific literature, only a few focus on analyzing the deviations of printed parts to develop a geometry-independent generalized deviation model. With the advent of metrological-grade structured-light 3D scanners, it is now possible to obtain accurate and dense data covering the entire built part. This comprehensive data can be used to characterize and understand the deviations introduced by the printing process, thereby opening new avenues for enhancing the precision and reliability of FFF 3D printing.

The primary objective of this research was to develop a robust methodology for evaluating and improving the geometric accuracy of FFF 3D printed parts. To achieve this, the study aimed to determine how to affect the 3D printing process to reduce geometric deviations based on 3D deviation values measured on the surface of the entire geometry. Additionally, it sought to interpret structured-light 3D scan data to obtain the optimal deviation value that can be acted on. Finally, the study focused on creating a model that can extract the optimal deviation values using as little data as possible.

We have demonstrated that deviations on the surface of an FFF 3D printed part consist of two components: one random and one systematic. Deviations must be processed and analyzed to distinguish between the deviation components effectively. Furthermore, we have shown that applying the inverse of the systematic deviation is an appropriate methodology to reduce the geometric deviation of printed parts. The systematic component of the deviations relating to geometry and machine can be approximated using scan data from multiple sacrificial printed parts.

In addition, we propose an ML methodology to infer the systematic deviation related to a single geometry and machine based on a single sacrificial printed part. This ML algorithm, trained on scan data of parts printed with various geometries and printers, can infer systematic deviation patterns from local deviation neighborhoods. We also present a methodology to capture the deviations of a printed part while it is still in the printing process.

The rapid adoption of 3D printing in industrial sectors, accompanied by a rise in geometric accuracy requirements in specific fields, creates the opportunity to integrate high-accuracy AM machines into supply chains. The solutions proposed in this research can improve the geometric accuracy of printed parts or reduce the cost of machines capable of such preci-

sion. Furthermore, we have paved the way for further analyses of deviations obtained by 3D scanning to detect patterns of deviation attributable to specific sources of error.

REFERENCES

[1] J. Comb, W. Priedeman, and P. W. Turley, "Fdm® technology process improvements," 1994. [Online]. Available: http://hdl.handle.net/2152/68588

[2] R. S. Woodbury, "The legend of eli whitney and interchangeable parts," *Technology and Culture*, vol. 1, no. 3, p. 235–253, 1960. [Online]. Available: https://www.jstor.org/stable/3101392

[3] C. J. Evans, "Precision engineering: an evolutionary perspective," *Philosophical Transactions of the Royal Society A: Mathematical, Physical and Engineering Sciences*, vol. 370, no. 1973, p. 3835–3851, Aug. 2012. [Online]. Available: https://royalsocietypublishing.org/doi/10.1098/rsta.2011.0050

[4] K. Maurice and O. Mayr, *The Clockwork Universe: German Clocks and Automata, 1550-1650*. Smithsonian Institution, 1980.

[5] C. Barnatt, *3D printing: the next industrial revolution*. [Nottingham, England?]: ExplainingTheFuture.com, 2013.

[6] A. Rosochowski and A. Matuszak, "Rapid tooling: the state of the art," *Journal of Materials Processing Technology*, vol. 106, no. 1, p. 191–198, Oct. 2000. [Online]. Available: https://www.sciencedirect.com/science/article/pii/S0924013600006130

[7] C. W. Lee, C. K. Chua, C. M. Cheah, L. H. Tan, and C. Feng, "Rapid investment casting: direct and indirect approaches via fused deposition modelling," *The International Journal of Advanced Manufacturing Technology*, vol. 23, no. 1, p. 93–101, Jan. 2004. [Online]. Available: https://doi.org/10.1007/s00170-003-1694-y

[8] D. Pal and B. Ravi, "Rapid tooling route selection and evaluation for sand and investment casting," *Virtual and Physical Prototyping*, vol. 2, no. 4, p. 197–207, 2007. [Online]. Available: http://www.tandfonline.com/doi/abs/10.1080/17452750701747088

[9] D. K. Pal, B. Ravi, and L. S. Bhargava, "Rapid tooling route selection for metal casting using qfd–anp methodology," *International Journal of Computer Integrated Manufacturing*, vol. 20, no. 4, p. 338–354, 2007. [Online]. Available: http://www.tandfonline.com/doi/abs/10.1080/09511920600883229

[10] M. Mahesh, Y. Wong, J. Fuh, and H. Loh, "Benchmarking for comparative evaluation of rp systems and processes," *Rapid Prototyping Journal*, vol. 10, no. 2, p. 123–135, Jan. 2004. [Online]. Available: https://doi.org/10.1108/13552540410526999

[11] Y. Zhang and Y. K. Chou, "A parametric study of part distortions in fdm using 3d fea," Sep. 2006. [Online]. Available: https://hdl.handle.net/2152/80128

[12] Y. Kuo, T. Yang, and G.-W. Huang, "The use of a grey-based taguchi method for optimizing multi-response simulation problems," *Engineering Optimization*, vol. 40, no. 6, p. 517–528, 2008. [Online]. Available: http://www.tandfonline.com/doi/abs/10.1080/03052150701857645

[13] A. K. Sood, R. K. Ohdar, and S. S. Mahapatra, "Improving dimensional accuracy of fused deposition modelling processed part using grey taguchi method," *Materials & Design*, vol. 30, no. 10, p. 4243–4252, Dec. 2009. [Online]. Available: https://www.sciencedirect.com/science/article/pii/S0261306909001794

[14] P. Hackney, "An investigation into the characteristics of materials and processes, for the production of accurate direct parts and tools using 3d rapid prototyping technologies," Ph.D. dissertation, Northumbria University, Jul 2007. [Online]. Available: http://nrl.northumbria.ac.uk/id/eprint/982/

[15] L. Bochmann, C. Bayley, M. Helu, R. Transchel, K. Wegener, and D. Dornfeld, "Understanding error generation in fused deposition modeling," *Surface Topography: Metrology and Properties*, vol. 3, no. 1, p. 014002, Jan 2015. [Online]. Available: https://iopscience.iop.org/article/10.1088/2051-672X/3/1/014002

[16] S. H. Masood and W. Q. Song, "Development of new metal/polymer materials for rapid tooling using fused deposition modelling," *Materials & Design*, vol. 25, no. 7, p. 587–594, Oct. 2004. [Online]. Available: https://www.sciencedirect.com/science/article/pii/S0261306904000378

[17] S. Khan, K. Joshi, and S. Deshmukh, "A comprehensive review on effect of printing parameters on mechanical properties of fdm printed parts," *Materials Today: Proceedings*, vol. 50, p. 2119–2127, Jan. 2022. [Online]. Available: https://www.sciencedirect.com/science/article/pii/S2214785321063495

[18] A. R. McLauchlin, O. R. Ghita, and L. Savage, "Studies on the reprocessability of poly(ether ether ketone) (peek)," *Journal of Materials Processing Technology*, vol.

214, no. 1, p. 75–80, Jan. 2014. [Online]. Available: https://www.sciencedirect.com/science/article/pii/S0924013613002367

[19] Q. Chen, Y.-Y. Zhang, P. Huang, Y.-Q. Li, and S.-Y. Fu, "Improved bond strength, reduced porosity and enhanced mechanical properties of 3d-printed polyetherimide composites by carbon nanotubes," *Composites Communications*, vol. 30, p. 101083, Feb. 2022. [Online]. Available: https://www.sciencedirect.com/science/article/pii/S2452213922000286

[20] D. Popescu, A. Zapciu, C. Amza, F. Baciu, and R. Marinescu, "Fdm process parameters influence over the mechanical properties of polymer specimens: A review," *Polymer Testing*, vol. 69, p. 157–166, Aug. 2018. [Online]. Available: https://www.sciencedirect.com/science/article/pii/S0142941818306093

[21] G. Peluso, O. Petillo, L. Ambrosio, and L. Nicolais, "Polyetherimide as biomaterial: preliminary in vitro and in vivo biocompatibility testing," *Journal of Materials Science: Materials in Medicine*, vol. 5, no. 9–10, p. 738–742, 1994. [Online]. Available: http://link.springer.com/10.1007/BF00120367

[22] S. Wickramasinghe, T. Do, and P. Tran, "Fdm-based 3d printing of polymer and associated composite: A review on mechanical properties, defects and treatments," *Polymers*, vol. 12, no. 7, p. 1529, Jul. 2020. [Online]. Available: https://www.mdpi.com/2073-4360/12/7/1529

[23] K. Rane and M. Strano, "A comprehensive review of extrusion-based additive manufacturing processes for rapid production of metallic and ceramic parts," *Advances in Manufacturing*, vol. 7, no. 2, p. 155–173, 2019. [Online]. Available: http://link.springer.com/10.1007/s40436-019-00253-6

[24] H. Gong, D. Snelling, K. Kardel, and A. Carrano, "Comparison of stainless steel 316l parts made by fdm- and slm-based additive manufacturing processes," *JOM*, vol. 71, no. 3, p. 880–885, 2019. [Online]. Available: http://link.springer.com/10.1007/s11837-018-3207-3

[25] M. Quarto, M. Carminati, and G. D'Urso, "Density and shrinkage evaluation of aisi 316l parts printed via fdm process," *Materials and Manufacturing Processes*, vol. 36, no. 13, p. 1535–1543, Oct. 2021. [Online]. Available: https://www.tandfonline.com/doi/full/10.1080/10426914.2021.1905830

[26] A. Pellegrini, M. G. Guerra, and F. Lavecchia, "Shrinkage evaluation and geometric accuracy assessment on 17–4 ph samples made by material extrusion additive manufacturing," *Journal of Manufacturing Processes*, vol. 109, p. 394–406, 2024. [Online]. Available: https://linkinghub.elsevier.com/retrieve/pii/S1526612523011374

[27] R. Jones, P. Haufe, E. Sells, P. Iravani, V. Olliver, C. Palmer, and A. Bowyer, "Reprap – the replicating rapid prototyper," *Robotica*, vol. 29, no. 1, p. 177–191, Jan. 2011. [Online]. Available: https://www.cambridge.org/core/journals/robotica/article/reprap-the-replicating-rapid-prototyper/5979FD7B0C066CBCE43EEAD869E871AA

[28] E. Pei, R. Ian Campbell, and D. de Beer, "Entry-level rp machines: how well can they cope with geometric complexity?" *Assembly Automation*, vol. 31, no. 2, p. 153–160, Jan. 2011. [Online]. Available: https://doi.org/10.1108/01445151111117737

[29] W. M. Johnson, M. Rowell, B. Deason, and M. Eubanks, "Benchmarking evaluation of an open source fused deposition modeling additive manufacturing system," 2011. [Online]. Available: https://hdl.handle.net/2152/88349

[30] P. Minetola and M. Galati, "A challenge for enhancing the dimensional accuracy of a low-cost 3d printer by means of self-replicated parts," *Additive Manufacturing*, vol. 22, p. 256–264, Aug. 2018. [Online]. Available: https://www.sciencedirect.com/science/article/pii/S2214860417301215

[31] P. Minetola, F. Calignano, and M. Galati, "Comparing geometric tolerance capabilities of additive manufacturing systems for polymers," *Additive Manufacturing*, vol. 32, p. 101103, Mar 2020. [Online]. Available: http://www.sciencedirect.com/science/article/pii/S221486041930675X

[32] P. J. Besl, "Active, optical range imaging sensors," *Machine Vision and Applications*, vol. 1, no. 2, p. 127–152, Jun. 1988. [Online]. Available: https://doi.org/10.1007/BF01212277

[33] K. L. Boyer and A. C. Kak, "Color-encoded structured light for rapid active ranging," *IEEE Transactions on Pattern Analysis and Machine Intelligence*, vol. PAMI-9, no. 1, p. 14–28, Jan. 1987. [Online]. Available: https://ieeexplore.ieee.org/document/4767869

[34] M. Levoy, K. Pulli, B. Curless, S. Rusinkiewicz, D. Koller, L. Pereira, M. Ginzton, S. Anderson, J. Davis, J. Ginsberg, J. Shade, and D. Fulk, "The digital michelangelo project: 3d scanning of large statues," in *Proceedings of the 27th annual conference on Computer graphics and interactive techniques*, ser. SIGGRAPH '00. USA: ACM

Press/Addison-Wesley Publishing Co., Jul. 2000, p. 131–144. [Online]. Available: https://dl.acm.org/doi/10.1145/344779.344849

[35] J.-A. Beraldin, F. Blais, L. Cournoyer, M. Rioux, S. El-Hakim, R. Rodella, F. Bernier, and N. Harrison, "Digital 3d imaging system for rapid response on remote sites," in *Second International Conference on 3-D Digital Imaging and Modeling (Cat. No.PR00062)*, Oct. 1999, p. 34–43. [Online]. Available: https://ieeexplore.ieee.org/document/805332

[36] C. Rocchini, P. Cignoni, C. Montani, P. Pingi, and R. Scopigno, "A low cost 3d scanner based on structured light," *Computer Graphics Forum*, vol. 20, no. 3, p. 299–308, 2001. [Online]. Available: https://onlinelibrary.wiley.com/doi/10.1111/1467-8659.00522

[37] M. Morimoto and K. Fujii, "A portable 3d scanner based on structured light and stereo camera," in *IEEE International Symposium on Communications and Information Technology, 2005. ISCIT 2005.*, vol. 1, Oct. 2005, p. 569–572. [Online]. Available: https://ieeexplore.ieee.org/abstract/document/1566919

[38] L.-S. Bieri and J. Jacot, "Three-dimensional vision using structured light applied to quality control in production line," in *Optical Metrology in Production Engineering*, vol. 5457. SPIE, Sep. 2004, p. 463–471. [Online]. Available: https://www.spiedigitallibrary.org/conference-proceedings-of-spie/5457/0000/Three-dimensional-vision-using-structured-light-applied-to-quality-control/10.1117/12.545039.full

[39] S. Voisin, D. L. Page, S. Foufou, F. Truchetet, and M. A. Abidi, "Color influence on accuracy of 3d scanners based on structured light," in *Machine Vision Applications in Industrial Inspection XIV*, vol. 6070. SPIE, Feb. 2006, p. 72–80. [Online]. Available: https://www.spiedigitallibrary.org/conference-proceedings-of-spie/6070/607009/Color-influence-on-accuracy-of-3D-scanners-based-on-structured/10.1117/12.643448.full

[40] M. Adamczyk, M. Kamiński, R. Sitnik, A. Bogdan, and M. Karaszewski, "Effect of temperature on calibration quality of structured-light three-dimensional scanners," *Applied Optics*, vol. 53, no. 23, p. 5154, Aug. 2014. [Online]. Available: https://opg.optica.org/abstract.cfm?URI=ao-53-23-5154

[41] F. Li, D. Stoddart, and I. Zwierzak, "A performance test for a fringe projection scanner in various ambient light conditions," *Procedia CIRP*, vol. 62, p. 400–404,

Jan. 2017. [Online]. Available: https://www.sciencedirect.com/science/article/pii/S2212827116306989

[42] D. Palousek, M. Omasta, D. Koutny, J. Bednar, T. Koutecky, and F. Dokoupil, "Effect of matte coating on 3d optical measurement accuracy," *Optical Materials*, vol. 40, p. 1–9, Feb. 2015. [Online]. Available: https://www.sciencedirect.com/science/article/pii/S0925346714005606

[43] J.-A. Beraldin, D. Mackinnon, and L. Cournoyer, "Metrological characterization of 3d imaging systems: progress report on standards developments," in *17th International Congress of Metrology*. EDP Sciences, 2015, p. 13003. [Online]. Available: https://cfmetrologie.edpsciences.org/articles/metrology/abs/2015/01/metrology_metr2015_13003/metrology_metr2015_13003.html

[44] P. Ghandali, F. Khameneifar, and J. R. R. Mayer, "A pseudo-3d ball lattice artifact and method for evaluating the metrological performance of structured-light 3d scanners," *Optics and Lasers in Engineering*, vol. 121, p. 87–95, Oct. 2019. [Online]. Available: https://www.sciencedirect.com/science/article/pii/S0143816618316191

[45] M. A. Isa, D. Sims-Waterhouse, S. Piano, and R. Leach, "Volumetric error modelling of a stereo vision system for error correction in photogrammetric three-dimensional coordinate metrology," *Precision Engineering*, vol. 64, p. 188–199, Jul. 2020. [Online]. Available: https://www.sciencedirect.com/science/article/pii/S0141635919309365

[46] F. Dickin, S. Pollard, and G. Adams, "Mapping and correcting the distortion of 3d structured light scanners," *Precision Engineering*, vol. 72, p. 543–555, Nov. 2021. [Online]. Available: https://www.sciencedirect.com/science/article/pii/S0141635921001550

[47] E. Cuesta, V. Meana, B. J. Álvarez, S. Giganto, and S. Martínez-Pellitero, "Metrology benchmarking of 3d scanning sensors using a ceramic gd&t-based artefact," *Sensors*, vol. 22, no. 22, p. 8596, Jan. 2022. [Online]. Available: https://www.mdpi.com/1424-8220/22/22/8596

[48] Y. Zhao, Y. Cheng, Q. Xu, Z. Luo, X. Wang, and H. Li, "Uncertainty modeling and evaluation of profile measurement by structured light scanner," *Measurement Science and Technology*, vol. 33, no. 9, p. 095018, Sep. 2022. [Online]. Available: https://iopscience.iop.org/article/10.1088/1361-6501/ac79a5

[49] W. Ameen, A. M. Al-Ahmari, and S. Hammad Mian, "Evaluation of handheld scanners for automotive applications," *Applied Sciences*, vol. 8, no. 2, p. 217, Feb. 2018. [Online]. Available: https://www.mdpi.com/2076-3417/8/2/217

[50] A. Haleem and M. Javaid, "3d scanning applications in medical field: A literature-based review," *Clinical Epidemiology and Global Health*, vol. 7, no. 2, p. 199–210, Jun. 2019. [Online]. Available: https://www.sciencedirect.com/science/article/pii/S2213398418300952

[51] K. Son and K.-b. Lee, "Effect of tooth types on the accuracy of dental 3d scanners: An in vitro study," *Materials*, vol. 13, no. 7, p. 1744, Jan. 2020. [Online]. Available: https://www.mdpi.com/1996-1944/13/7/1744

[52] L. van Brügge, K. M. Çetin, S. J. Koeberle, M. Thiele, F. Sturm, and M. Hornung, "Application of 3d-scanning for structural and geometric assessment of aerospace structures," *CEAS Aeronautical Journal*, Apr. 2023. [Online]. Available: https://doi.org/10.1007/s13272-023-00654-1

[53] Z. M. Zhang, S. Catalucci, A. Thompson, R. Leach, and S. Piano, "Applications of data fusion in optical coordinate metrology: a review," *The International Journal of Advanced Manufacturing Technology*, vol. 124, no. 5, p. 1341–1356, Jan. 2023. [Online]. Available: https://doi.org/10.1007/s00170-022-10576-7

[54] D. O. Hebb, *The organization of behavior; a neuropsychological theory*, ser. The organization of behavior; a neuropsychological theory. Oxford, England: Wiley, 1949.

[55] F. Rosenblatt, "The perceptron: A probabilistic model for information storage and organization in the brain," *Psychological Review*, vol. 65, no. 6, p. 386–408, 1958.

[56] D. H. Ackley, G. E. Hinton, and T. J. Sejnowski, "A learning algorithm for boltzmann machines," *Cognitive Science*, vol. 9, no. 1, p. 147–169, Jan. 1985. [Online]. Available: https://www.sciencedirect.com/science/article/pii/S0364021385800124

[57] D. E. Rumelhart, G. E. Hinton, and R. J. Williams, "Learning representations by back-propagating errors," *Nature*, vol. 323, no. 6088, p. 533–536, Oct. 1986. [Online]. Available: https://www.nature.com/articles/323533a0

[58] Y. Lecun, L. Bottou, Y. Bengio, and P. Haffner, "Gradient-based learning applied to document recognition," *Proceedings of the IEEE*, vol. 86, no. 11, p. 2278–2324, Nov. 1998. [Online]. Available: https://ieeexplore.ieee.org/abstract/document/726791

[59] A. Krizhevsky, I. Sutskever, and G. E. Hinton, "Imagenet classification with deep convolutional neural networks," in *Advances in Neural Information Processing Systems*, vol. 25. Curran Associates, Inc., 2012. [Online]. Available: https://papers.nips.cc/paper_files/paper/2012/hash/c399862d3b9d6b76c8436e924a68c45b-Abstract.html

[60] V. Nair and G. E. Hinton, "Rectified linear units improve restricted boltzmann machines," in *Proceedings of the 27th International Conference on International Conference on Machine Learning*, ser. ICML'10. Madison, WI, USA: Omnipress, Jun. 2010, p. 807–814.

[61] N. Srivastava, G. Hinton, A. Krizhevsky, I. Sutskever, and R. Salakhutdinov, "Dropout: A simple way to prevent neural networks from overfitting," *Journal of Machine Learning Research*, vol. 15, no. 56, p. 1929–1958, 2014. [Online]. Available: http://jmlr.org/papers/v15/srivastava14a.html

[62] K. Simonyan and A. Zisserman, "Very deep convolutional networks for large-scale image recognition," *3rd International Conference on Learning Representations (ICLR 2015)*, 2015. [Online]. Available: https://ora.ox.ac.uk/objects/uuid:60713f18-a6d1-4d97-8f45-b60ad8aebbce

[63] C. Szegedy, W. Liu, Y. Jia, P. Sermanet, S. Reed, D. Anguelov, D. Erhan, V. Vanhoucke, and A. Rabinovich, "Going deeper with convolutions," 2015, p. 1–9. [Online]. Available: https://www.cv-foundation.org/openaccess/content_cvpr_2015/html/Szegedy_Going_Deeper_With_2015_CVPR_paper.html

[64] K. He, X. Zhang, S. Ren, and J. Sun, "Deep residual learning for image recognition," in *2016 IEEE Conference on Computer Vision and Pattern Recognition (CVPR)*, Jun. 2016, p. 770–778. [Online]. Available: https://ieeexplore.ieee.org/document/7780459/figures#figures

[65] R. Socher, B. Huval, B. Bath, C. D. Manning, and A. Ng, "Convolutional-recursive deep learning for 3d object classification," in *Advances in Neural Information Processing Systems*, vol. 25. Curran Associates, Inc., 2012. [Online]. Available: https://proceedings.neurips.cc/paper/2012/hash/3eae62bba9ddf64f69d49dc48e2dd214-Abstract.html

[66] H. Su, S. Maji, E. Kalogerakis, and E. Learned-Miller, "Multi-view convolutional neural networks for 3d shape recognition," 2015, p. 945–953. [Online]. Available: https://www.cv-foundation.org/openaccess/content_iccv_2015/html/Su_Multi-View_Convolutional_Neural_ICCV_2015_paper.html

[67] Z. Wu, S. Song, A. Khosla, F. Yu, L. Zhang, X. Tang, and J. Xiao, "3d shapenets: A deep representation for volumetric shapes," 2015, p. 1912–1920. [Online]. Available: https://www.cv-foundation.org/openaccess/content_cvpr_2015/html/Wu_3D_ShapeNets_A_2015_CVPR_paper.html

[68] D. Maturana and S. Scherer, "Voxnet: A 3d convolutional neural network for real-time object recognition," in *2015 IEEE/RSJ International Conference on Intelligent Robots and Systems (IROS)*, Sep. 2015, p. 922–928. [Online]. Available: https://ieeexplore.ieee.org/abstract/document/7353481

[69] C. R. Qi, H. Su, K. Mo, and L. J. Guibas, "Pointnet: Deep learning on point sets for 3d classification and segmentation," 2017, p. 652–660. [Online]. Available: https://openaccess.thecvf.com/content_cvpr_2017/html/Qi_PointNet_Deep_Learning_CVPR_2017_paper.html

[70] C. R. Qi, L. Yi, H. Su, and L. J. Guibas, "Pointnet++: Deep hierarchical feature learning on point sets in a metric space," in *Advances in Neural Information Processing Systems*, vol. 30. Curran Associates, Inc., 2017. [Online]. Available: https://proceedings.neurips.cc/paper_files/paper/2017/hash/d8bf84be3800d12f74d8b05e9b89836f-Abstract.html

[71] R. Klokov and V. Lempitsky, "Escape from cells: Deep kd-networks for the recognition of 3d point cloud models," 2017, p. 863–872. [Online]. Available: https://openaccess.thecvf.com/content_iccv_2017/html/Klokov_Escape_From_Cells_ICCV_2017_paper.html

[72] P.-S. Wang, Y. Liu, Y.-X. Guo, C.-Y. Sun, and X. Tong, "O-cnn: octree-based convolutional neural networks for 3d shape analysis," *ACM Transactions on Graphics*, vol. 36, no. 4, pp. 72:1–72:11, Jul. 2017. [Online]. Available: https://doi.org/10.1145/3072959.3073608

[73] J. Li, B. M. Chen, and G. H. Lee, "So-net: Self-organizing network for point cloud analysis," 2018. [Online]. Available: https://arxiv.org/abs/1803.04249

[74] Y. Feng, Y. Feng, H. You, X. Zhao, and Y. Gao, "Meshnet: Mesh neural network for 3d shape representation," *Proceedings of the AAAI Conference on Artificial Intelligence*, vol. 33, no. 01, p. 8279–8286, Jul. 2019. [Online]. Available: https://ojs.aaai.org/index.php/AAAI/article/view/4840

[75] G. Chen, M. Wang, Y. Yang, K. Yu, L. Yuan, and Y. Yue, "Point-gpt: Auto-regressively generative pre-training from point clouds," *Advances in Neural Information Processing Systems*, vol. 36, p. 29667–29679, Dec. 2023. [Online]. Available: https://proceedings.neurips.cc/paper_files/paper/2023/hash/5ed5c3c846f684a54975ad7a2525199f-Abstract-Conference.html

[76] Z. Qi, R. Dong, S. Zhang, H. Geng, C. Han, Z. Ge, H. Wang, L. Yi, and K. Ma, "Shapellm: Universal 3d object understanding for embodied interaction," no. arXiv:2402.17766, Mar. 2024, arXiv:2402.17766 [cs]. [Online]. Available: http://arxiv.org/abs/2402.17766

[77] S. Srivastava and G. Sharma, "Exploiting local geometry for feature and graph construction for better 3d point cloud processing with graph neural networks," in *2021 IEEE International Conference on Robotics and Automation (ICRA)*, May 2021, p. 12903–12909. [Online]. Available: https://ieeexplore.ieee.org/document/9561327

[78] Z. Liu, G. Wang, Y. Huo, and W. Zhao, "Research on precise control of 3d print nozzle temperature in peek material," Hubei Province, China, 2017, p. 040076. [Online]. Available: https://pubs.aip.org/aip/acp/article/688226

[79] H. Wu, Z. Yu, and Y. Wang, "A new approach for online monitoring of additive manufacturing based on acoustic emission," in *Volume 3: Joint MSEC-NAMRC Symposia*. Blacksburg, Virginia, USA: American Society of Mechanical Engineers, Jun. 2016, p. V003T08A013. [Online]. Available: https://asmedigitalcollection.asme.org/MSEC/proceedings/MSEC2016/49910/Blacksburg,%20Virginia,%20USA/267244

[80] H. Wu, Y. Wang, and Z. Yu, "In situ monitoring of fdm machine condition via acoustic emission," *The International Journal of Advanced Manufacturing Technology*, vol. 84, no. 5, p. 1483–1495, May 2016. [Online]. Available: https://doi.org/10.1007/s00170-015-7809-4

[81] H. Wu, Z. Yu, and Y. Wang, "Real-time fdm machine condition monitoring and diagnosis based on acoustic emission and hidden semi-markov model," *The International Journal of Advanced Manufacturing Technology*, vol. 90, no. 5, p. 2027–2036, May 2017. [Online]. Available: https://doi.org/10.1007/s00170-016-9548-6

[82] J. Liu, Y. Hu, B. Wu, and Y. Wang, "An improved fault diagnosis approach for fdm process with acoustic emission," *Journal of Manufacturing Processes*, vol. 35, p. 570–579, Oct. 2018. [Online]. Available: https://www.sciencedirect.com/science/article/pii/S1526612518312714

[83] S. A. Shevchik, C. Kenel, C. Leinenbach, and K. Wasmer, "Acoustic emission for in situ quality monitoring in additive manufacturing using spectral convolutional neural networks," *Additive Manufacturing*, vol. 21, p. 598–604, May 2018. [Online]. Available: https://www.sciencedirect.com/science/article/pii/S221486041730132X

[84] Y. Li, W. Zhao, Q. Li, T. Wang, and G. Wang, "In-situ monitoring and diagnosing for fused filament fabrication process based on vibration sensors," *Sensors*, vol. 19, no. 11, p. 2589, Jan. 2019. [Online]. Available: https://www.mdpi.com/1424-8220/19/11/2589

[85] J. E. Seppala and K. D. Migler, "Infrared thermography of welding zones produced by polymer extrusion additive manufacturing," *Additive Manufacturing*, vol. 12, p. 71–76, Oct. 2016. [Online]. Available: https://www.sciencedirect.com/science/article/pii/S2214860416301269

[86] G. Bi, A. Gasser, K. Wissenbach, A. Drenker, and R. Poprawe, "Identification and qualification of temperature signal for monitoring and control in laser cladding," *Optics and Lasers in Engineering*, vol. 44, no. 12, p. 1348–1359, Dec. 2006. [Online]. Available: https://www.sciencedirect.com/science/article/pii/S0143816606000273

[87] ——, "Characterization of the process control for the direct laser metallic powder deposition," *Surface and Coatings Technology*, vol. 201, no. 6, p. 2676–2683, Dec. 2006. [Online]. Available: https://www.sciencedirect.com/science/article/pii/S0257897206004117

[88] C. Kousiatza and D. Karalekas, "In-situ monitoring of strain and temperature distributions during fused deposition modeling process," *Materials & Design*, vol. 97, p. 400–406, May 2016. [Online]. Available: https://www.sciencedirect.com/science/article/pii/S0264127516302441

[89] S. J. Pan and Q. Yang, "A survey on transfer learning," *IEEE Transactions on Knowledge and Data Engineering*, vol. 22, no. 10, p. 1345–1359, Oct. 2010. [Online]. Available: https://ieeexplore.ieee.org/abstract/document/5288526

[90] O. Russakovsky, J. Deng, H. Su, J. Krause, S. Satheesh, S. Ma, Z. Huang, A. Karpathy, A. Khosla, M. Bernstein, A. C. Berg, and L. Fei-Fei, "Imagenet large scale visual recognition challenge," *International Journal of Computer Vision*, vol. 115, no. 3, p. 211–252, Dec. 2015. [Online]. Available: https://doi.org/10.1007/s11263-015-0816-y

[91] J. M. Gardner, K. A. Hunt, A. B. Ebel, E. S. Rose, S. C. Zylich, B. D. Jensen, K. E. Wise, E. J. Siochi, and G. Sauti, "Machines as craftsmen: Localized

parameter setting optimization for fused filament fabrication 3d printing," *Advanced Materials Technologies*, vol. 4, no. 3, p. 1800653, 2019. [Online]. Available: https://onlinelibrary.wiley.com/doi/10.1002/admt.201800653

[92] Y. Bengio, A. Courville, and P. Vincent, "Representation learning: A review and new perspectives," *IEEE Transactions on Pattern Analysis and Machine Intelligence*, vol. 35, no. 8, p. 1798–1828, Aug. 2013. [Online]. Available: https://ieeexplore.ieee.org/abstract/document/6472238

[93] M. Minsky and S. A. Papert, "Linear separation and learning," Oct. 1968. [Online]. Available: https://dspace.mit.edu/handle/1721.1/6170

[94] C. Liu, A. C. C. Law, D. Roberson, and Z. J. Kong, "Image analysis-based closed loop quality control for additive manufacturing with fused filament fabrication," *Journal of Manufacturing Systems*, vol. 51, p. 75–86, Apr. 2019. [Online]. Available: https://www.sciencedirect.com/science/article/pii/S0278612518304060

[95] Z. Jin, Z. Zhang, and G. X. Gu, "Autonomous in-situ correction of fused deposition modeling printers using computer vision and deep learning," *Manufacturing Letters*, vol. 22, p. 11–15, Oct. 2019. [Online]. Available: https://www.sciencedirect.com/science/article/pii/S2213846319300847

[96] D. A. J. Brion and S. W. Pattinson, "Quantitative and real-time control of 3d printing material flow through deep learning," *Advanced Intelligent Systems*, vol. 4, no. 11, p. 2200153, 2022. [Online]. Available: https://onlinelibrary.wiley.com/doi/10.1002/aisy.202200153

[97] A. Vaswani, N. Shazeer, N. Parmar, J. Uszkoreit, L. Jones, A. N. Gomez, L. Kaiser, and I. Polosukhin, "Attention is all you need," in *Advances in Neural Information Processing Systems*, vol. 30. Curran Associates, Inc., 2017. [Online]. Available: https://proceedings.neurips.cc/paper_files/paper/2017/hash/3f5ee243547dee91fbd053c1c4a845aa-Abstract.html

[98] D. A. J. Brion and S. W. Pattinson, "Generalisable 3d printing error detection and correction via multi-head neural networks," *Nature Communications*, vol. 13, no. 1, p. 4654, Aug. 2022. [Online]. Available: https://www.nature.com/articles/s41467-022-31985-y

[99] S. Sartori and G. X. Zhang, "Geometric error measurement and compensation of machines," *CIRP Annals*, vol. 44, no. 2, p. 599–609, Jan. 1995. [Online]. Available: https://www.sciencedirect.com/science/article/pii/S0007850607605071

[100] S. Chowdhury and S. Anand, "Artificial neural network based geometric compensation for thermal deformation in additive manufacturing processes," Sep 2016. [Online]. Available: https://asmedigitalcollection.asme.org/MSEC/proceedings/MSEC2016/49910/V003T08A006/267254

[101] S. Chowdhury, K. Mhapsekar, and S. Anand, "Part build orientation optimization and neural network-based geometry compensation for additive manufacturing process," *Journal of Manufacturing Science and Engineering*, vol. 140, no. 3, Mar 2018. [Online]. Available: https://asmedigitalcollection.asme.org/manufacturingscience/article/140/3/031009/366667/Part-Build-Orientation-Optimization-and-Neural

[102] Z. Zhu, N. Anwer, and L. Mathieu, "Geometric deviation modeling with statistical shape analysis in design for additive manufacturing," *Procedia CIRP*, vol. 84, p. 496–501, Jan. 2019. [Online]. Available: https://www.sciencedirect.com/science/article/pii/S2212827119308984

[103] Z. Zhu, K. Ferreira, N. Anwer, L. Mathieu, K. Guo, and L. Qiao, "Convolutional neural network for geometric deviation prediction in additive manufacturing," *Procedia CIRP*, vol. 91, p. 534–539, Jan. 2020. [Online]. Available: https://www.sciencedirect.com/science/article/pii/S2212827120308623

[104] P. Charalampous, I. Kostavelis, T. Kontodina, and D. Tzovaras, "Learning-based error modeling in fdm 3d printing process," *Rapid Prototyping Journal*, vol. 27, no. 3, p. 507–517, Jan. 2021. [Online]. Available: https://doi.org/10.1108/RPJ-03-2020-0046

[105] K. Tong, E. A. Lehtihet, and S. Joshi, "Software compensation of rapid prototyping machines," *Precision Engineering*, vol. 28, no. 3, p. 280–292, Jul 2004. [Online]. Available: http://www.sciencedirect.com/science/article/pii/S0141635903001594

[106] C. Cajal, J. Santolaria, J. Velazquez, S. Aguado, and J. Albajez, "Volumetric error compensation technique for 3d printers," *Procedia Engineering*, vol. 63, p. 642–649, Jan 2013. [Online]. Available: http://www.sciencedirect.com/science/article/pii/S1877705813014896

[107] C. Cajal, J. Santolaria, D. Samper, and J. Velazquez, "Efficient volumetric error compensation technique for additive manufacturing machines," *Rapid Prototyping Journal*, vol. 22, no. 1, p. 2–19, Jan. 2016. [Online]. Available: https://doi.org/10.1108/RPJ-05-2014-0061

[108] L. Cheng, F. Tsung, and A. Wang, "A statistical transfer learning perspective for modeling shape deviations in additive manufacturing," *IEEE Robotics and Automation Letters*, vol. 2, no. 4, p. 1988–1993, Oct. 2017. [Online]. Available: https://ieeexplore.ieee.org/abstract/document/7942096

[109] N. Cressie, "Spatial prediction and ordinary kriging," *Mathematical Geology*, vol. 20, no. 4, p. 405–421, May 1988. [Online]. Available: https://doi.org/10.1007/BF00892986

[110] S. Song, A. Wang, Q. Huang, and F. Tsung, "Shape deviation modeling for fused deposition modeling processes," in *2014 IEEE International Conference on Automation Science and Engineering (CASE)*. Taipei: IEEE, 2014, p. 758–763. [Online]. Available: http://ieeexplore.ieee.org/document/6899411/

[111] Q. Huang, H. Nouri, K. Xu, Y. Chen, S. Sosina, and T. Dasgupta, "Statistical predictive modeling and compensation of geometric deviations of three-dimensional printed products," *Journal of Manufacturing Science and Engineering*, vol. 136, no. 6, p. 061008, Oct 2014. [Online]. Available: http://manufacturingscience.asmedigitalcollection.asme.org/article.aspx?doi=10.1115/1.4028510

[112] ——, "Predictive modeling of geometric deviations of 3d printed products - a unified modeling approach for cylindrical and polygon shapes," in *2014 IEEE International Conference on Automation Science and Engineering (CASE)*, Aug. 2014, p. 25–30. [Online]. Available: https://ieeexplore.ieee.org/document/6899299

[113] Q. Huang, J. Zhang, A. Sabbaghi, and T. Dasgupta, "Optimal offline compensation of shape shrinkage for three-dimensional printing processes," *IIE Transactions*, vol. 47, no. 5, p. 431–441, May 2015. [Online]. Available: https://doi.org/10.1080/0740817X.2014.955599

[114] H. Luan and Q. Huang, "Prescriptive modeling and compensation of in-plane shape deformation for 3-d printed freeform products," *IEEE Transactions on Automation Science and Engineering*, vol. 14, no. 1, pp. 73–82, 2016.

[115] L. Cheng, A. Wang, and F. Tsung, "A prediction and compensation scheme for in-plane shape deviation of additive manufacturing with information on process parameters," *IISE Transactions*, vol. 50, no. 5, p. 394–406, May 2018. [Online]. Available: https://www.tandfonline.com/doi/full/10.1080/24725854.2017.1402224

[116] Q. Huang, Y. Wang, M. Lyu, and W. Lin, "Shape deviation generator—a convolution framework for learning and predicting 3-d printing shape accuracy," *IEEE Transactions on Automation Science and Engineering*, vol. 17, no. 3, p. 1486–1500, Jul 2020.

[117] H. Wang and Q. Huang, "Using error equivalence concept to automatically adjust discrete manufacturing processes for dimensional variation control," *Journal of Manufacturing Science and Engineering*, vol. 129, no. 3, p. 644–652, Jun. 2007. [Online]. Available: https://asmedigitalcollection.asme.org/manufacturingscience/article/129/3/644/462150/Using-Error-Equivalence-Concept-to-Automatically

[118] Y. Jin, S. J. Qin, and Q. Huang, "Modeling inter-layer interactions for out-of-plane shape deviation reduction in additive manufacturing," *IISE Transactions*, vol. 52, no. 7, p. 721–731, Jul. 2020. [Online]. Available: https://www.tandfonline.com/doi/full/10.1080/24725854.2019.1676936

[119] S. Afazov, A. Okioga, A. Holloway, W. Denmark, A. Triantaphyllou, S.-A. Smith, and L. Bradley-Smith, "A methodology for precision additive manufacturing through compensation," *Precision Engineering*, vol. 50, p. 269–274, 2017. [Online]. Available: https://linkinghub.elsevier.com/retrieve/pii/S0141635917301484

[120] N. Decker, M. Lyu, Y. Wang, and Q. Huang, "Geometric accuracy prediction and improvement for additive manufacturing using triangular mesh shape data," *Journal of Manufacturing Science and Engineering*, vol. 143, no. 6, p. 061006, Jun 2021. [Online]. Available: https://asmedigitalcollection.asme.org/manufacturingscience/article/143/6/061006/1091390/Geometric-Accuracy-Prediction-and-Improvement-for

[121] M. Zhao, G. Xiong, W. Wang, Q. Fang, Z. Shen, L. Wan, and F. Zhu, "A point-based neural network for real-scenario deformation prediction in additive manufacturing," in *2022 IEEE 18th International Conference on Automation Science and Engineering (CASE)*, Aug. 2022, p. 1656–1661. [Online]. Available: https://ieeexplore.ieee.org/document/9926549

[122] Y. Wang, C. Ruiz, and Q. Huang, "Learning and predicting shape deviations of smooth and non-smooth 3d geometries through mathematical decomposition of additive manufacturing," *IEEE Transactions on Automation Science and Engineering*, vol. 20, no. 3, p. 1527–1538, Jul. 2023. [Online]. Available: https://ieeexplore.ieee.org/abstract/document/9786748

[123] E. Sachs, M. Cima, P. Williams, D. Brancazio, and J. Cornie, "Three dimensional printing: Rapid tooling and prototypes directly from a cad model," *Journal of Engineering for Industry*, vol. 114, no. 4, p. 481–488, Nov 1992. [Online]. Available: https://asmedigitalcollection.asme.org/manufacturingscience/article/114/4/481/454796/Three-Dimensional-Printing-Rapid-Tooling-and

[124] W. Gao, Y. Zhang, D. Ramanujan, K. Ramani, Y. Chen, C. B. Williams, C. C. L. Wang, Y. C. Shin, S. Zhang, and P. D. Zavattieri, "The status, challenges, and future of additive manufacturing in engineering," *Computer-Aided Design*, vol. 69, p. 65–89, Dec 2015. [Online]. Available: http://www.sciencedirect.com/science/article/pii/S0010448515000469

[125] B. Msallem, N. Sharma, S. Cao, F. S. Halbeisen, H.-F. Zeilhofer, and F. M. Thieringer, "Evaluation of the dimensional accuracy of 3d-printed anatomical mandibular models using fff, sla, sls, mj, and bj printing technology," *Journal of Clinical Medicine*, vol. 9, no. 3, p. 817, Mar 2020. [Online]. Available: https://www.mdpi.com/2077-0383/9/3/817

[126] A. Manero, P. Smith, A. Koontz, M. Dombrowski, J. Sparkman, D. Courbin, and A. Chi, "Leveraging 3d printing capacity in times of crisis: Recommendations for covid-19 distributed manufacturing for medical equipment rapid response," *International Journal of Environmental Research and Public Health*, vol. 17, no. 13, p. 4634, Jan 2020. [Online]. Available: https://www.mdpi.com/1660-4601/17/13/4634

[127] J. M. Pearce, "Distributed manufacturing of open source medical hardware for pandemics," *Journal of Manufacturing and Materials Processing*, vol. 4, no. 2, p. 49, Jun 2020. [Online]. Available: https://www.mdpi.com/2504-4494/4/2/49

[128] V. Akinsowon and M. Nahirna, "State of the 3d printing industry survey 2019: Am service providers," Feb 2019. [Online]. Available: https://amfg.ai/state-of-the-3d-industry-survey-2019-am-service-providers-2/?cn-reloaded=1

[129] I. Gibson, D. W. Rosen, and B. Stucker, *Additive manufacturing technologies: 3D printing, rapid prototyping, and direct digital manufacturing.* Springer, 2016.

[130] H. J. Yang, P. J. Hwang, and S. H. Lee, "A study on shrinkage compensation of the sls process by using the taguchi method," *International Journal of Machine Tools and Manufacture*, vol. 42, no. 11, p. 1203–1212, Sep 2002. [Online]. Available: http://www.sciencedirect.com/science/article/pii/S0890695502000706

[131] D. Karalekas and A. Aggelopoulos, "Study of shrinkage strains in a stereolithography cured acrylic photopolymer resin," *Journal of Materials Processing Technology*, vol. 136, no. 1, p. 146–150, May 2003. [Online]. Available: http://www.sciencedirect.com/science/article/pii/S0924013603000281

[132] T.-M. Wang, J.-T. Xi, and Y. Jin, "A model research for prototype warp deformation in the fdm process," *The International Journal of Advanced Manufacturing Technology*, vol. 33, no. 11, p. 1087–1096, Aug 2007. [Online]. Available: https://doi.org/10.1007/s00170-006-0556-9

[133] D. Bourell, J. P. Kruth, M. Leu, G. Levy, D. Rosen, A. M. Beese, and A. Clare, "Materials for additive manufacturing," *CIRP Annals*, vol. 66, no. 2, p. 659–681, Jan 2017. [Online]. Available: http://www.sciencedirect.com/science/article/pii/S0007850617301488

[134] K. Tong, E. Amine Lehtihet, and S. Joshi, "Parametric error modeling and software error compensation for rapid prototyping," *Rapid Prototyping Journal*, vol. 9, no. 5, p. 301–313, 2003. [Online]. Available: http://www.emeraldinsight.com/doi/10.1108/13552540310502202

[135] K. Tong, S. Joshi, and E. Amine Lehtihet, "Error compensation for fused deposition modeling (fdm) machine by correcting slice files," *Rapid Prototyping Journal*, vol. 14, no. 1, p. 4–14, Jan 2008. [Online]. Available: http://www.emeraldinsight.com/doi/10.1108/13552540810841517

[136] J. Lyu and S. Manoochehri, "Modeling machine motion and process parameter errors for improving dimensional accuracy of fused deposition modeling machines," *Journal of Manufacturing Science and Engineering*, vol. 140, no. 12, Dec 2018. [Online]. Available: https://asmedigitalcollection.asme.org/manufacturingscience/article/140/12/121012/367005/Modeling-Machine-Motion-and-Process-Parameter

[137] Q. Huang, "An analytical foundation for optimal compensation of three-dimensional shape deformation in additive manufacturing," *Journal of Manufacturing Science and Engineering*, vol. 138, no. 6, pp. 061 010–061 010–8, Jan 2016. [Online]. Available: http://dx.doi.org/10.1115/1.4032220

[138] M. McConaha and S. Anand, "Additive manufacturing distortion compensation based on scan data of built geometry," *Journal of Manufacturing Science and Engineering*, vol. 142, no. 6, Jun 2020. [Online]. Available: https://asmedigitalcollection.asme.org/manufacturingscience/article/142/6/061001/1074959/Additive-Manufacturing-Distortion-Compensation

[139] K. Xu, T.-H. Kwok, Z. Zhao, and Y. Chen, "A reverse compensation framework for shape deformation control in additive manufacturing," *Journal of Computing and*

Information Science in Engineering, vol. 17, no. 2, pp. 021 012–021 012–9, Feb 2017. [Online]. Available: http://dx.doi.org/10.1115/1.4034874

[140] T. Grimm, *Users guide to rapid prototyping.* Society of Manufacturing Engineeers, 2004.

[141] P. J. Besl and N. D. McKay, "A method for registration of 3-d shapes," *IEEE Transactions on Pattern Analysis and Machine Intelligence*, vol. 14, no. 2, pp. 239–256, 1992.

[142] M. M. Dowling, P. M. Griffin, T. K L, and C. Zhou, "Statistical issues in geometric feature inspection using coordinate measuring machines," *Technometrics*, vol. 39, no. 1, p. 3, 02 1997, copyright - Copyright American Statistical Association Feb 1997; Last updated - 2013-01-07; CODEN - TCMTA2. [Online]. Available: https://search.proquest.com/docview/213687964?accountid=40695

[143] T. Weyrich, M. Pauly, R. Keiser, S. Heinzle, S. Scandella, and M. Gross, "Post-processing of scanned 3d surface data," *Proceedings of the First Eurographics Conference on Point-Based Graphics*, p. 85–94, 2004.

[144] M. Desbrun, M. Meyer, P. Schröder, and A. H. Barr, "Implicit fairing of irregular meshes using diffusion and curvature flow," *Proceedings of the 26th annual conference on Computer graphics and interactive techniques - SIGGRAPH 99*, 1999.

[145] N. Sharp, Y. Soliman, and K. Crane, "The vector heat method," *ACM Transactions on Graphics*, vol. 38, no. 3, p. 24:1–24:19, Jun 2019. [Online]. Available: https://doi.org/10.1145/3243651

[146] A. Bunge, P. Herholz, M. Kazhdan, and M. Botsch, "Polygon laplacian made simple," *Computer Graphics Forum*, vol. 39, no. 2, p. 303–313, 2020. [Online]. Available: https://onlinelibrary.wiley.com/doi/abs/10.1111/cgf.13931

[147] R. Lipman and J. Filliben, "Testing implementations of geometric dimensioning and tolerancing in cad software," *Computer-Aided Design and Applications*, vol. 17, pp. 1241–1265, 02 2020.

[148] G. Navangul, R. Paul, and S. Anand, "Error minimization in layered manufacturing parts by stereolithography file modification using a vertex translation algorithm," *Journal of Manufacturing Science and Engineering*, vol. 135, no. 3, Jun 2013. [Online]. Available: https://asmedigitalcollection.asme.org/manufacturingscience/article/135/3/031006/377087/Error-Minimization-in-Layered-Manufacturing-Parts

[149] (2019) Acceptance/reverification according to vdi/vde 2634, part 3. [Online]. Available: https://www.zebicon.com/fileadmin/user_upload/2_Maaleudstyr/9_Certifikater/ATOS_Core_200_SN160300/2019-04-02_Acceptance_test_ATOS_Core_MV200_SN160300.pdf

[150] Dawson-Haggerty et al., "Trimesh," 2019, https://trimsh.org/.

[151] A. Jacobson, D. Panozzo *et al.*, "libigl: A simple C++ geometry processing library," 2018, https://libigl.github.io/.

[152] American Society of Mechanical Engineers, *ASME Y14.5 - 2018: Dimensioning and Tolerancing*, 2018. [Online]. Available: https://books.google.ca/books?id=babdxgEACAAJ

[153] E. Sachs, M. Cima, P. Williams, D. Brancazio, and J. Cornie, "Three dimensional printing: rapid tooling and prototypes directly from a cad model," *Journal of Engineering for Industry*, 1992.

[154] I. Campbell, D. Bourell, and I. Gibson, "Additive manufacturing: rapid prototyping comes of age," *Rapid prototyping journal*, vol. 18, no. 4, pp. 255–258, 2012.

[155] B. M. Colosimo, Q. Huang, T. Dasgupta, and F. Tsung, "Opportunities and challenges of quality engineering for additive manufacturing," *Journal of Quality Technology*, vol. 50, no. 3, p. 233–252, Jul 2018. [Online]. Available: https://doi.org/10.1080/00224065.2018.1487726

[156] M. Mehrpouya, A. Dehghanghadikolaei, B. Fotovvati, A. Vosooghnia, S. S. Emamian, and A. Gisario, "The potential of additive manufacturing in the smart factory industrial 4.0: A review," *Applied Sciences*, vol. 9, no. 18, p. 3865, 2019.

[157] Z. Ye, C. Liu, W. Tian, and C. Kan, "A deep learning approach for the identification of small process shifts in additive manufacturing using 3d point clouds," *Procedia Manufacturing*, vol. 48, pp. 770–775, 2020.

[158] T. S. Tamir, G. Xiong, Q. Fang, Y. Yang, Z. Shen, M. Zhou, and J. Jiang, "Machine-learning-based monitoring and optimization of processing parameters in 3d printing," *International Journal of Computer Integrated Manufacturing*, pp. 1–17, 2022.

[159] D. A. Brion and S. W. Pattinson, "Generalisable 3d printing error detection and correction via multi-head neural networks," *Nature Communications*, vol. 13, no. 1, p. 4654, 2022.

[160] J. Chacón, M. A. Caminero, E. García-Plaza, and P. J. Núnez, "Additive manufacturing of pla structures using fused deposition modelling: Effect of process parameters on mechanical properties and their optimal selection," *Materials & Design*, vol. 124, pp. 143–157, 2017.

[161] S. Liu, P. Zhao, S. Wu, C. Zhang, J. Fu, and Z. Chen, "A pellet 3d printer: device design and process parameters optimization," *Advances in Polymer Technology*, vol. 2019, pp. 1–8, 2019.

[162] A. Elkaseer, S. Schneider, and S. G. Scholz, "Experiment-based process modeling and optimization for high-quality and resource-efficient fff 3d printing," *Applied Sciences*, vol. 10, no. 8, p. 2899, 2020.

[163] S. Deswal, R. Narang, and D. Chhabra, "Modeling and parametric optimization of fdm 3d printing process using hybrid techniques for enhancing dimensional preciseness," *International Journal on Interactive Design and Manufacturing (IJIDeM)*, vol. 13, pp. 1197–1214, 2019.

[164] R. F. Sarraga, "Modifying cad/cam surfaces according to displacements prescribed at a finite set of points," *Computer-Aided Design*, vol. 36, no. 4, p. 343–349, 2004. [Online]. Available: https://linkinghub.elsevier.com/retrieve/pii/S0010448503001015

[165] S. Chowdhury and S. Anand, "Artificial neural network based geometric compensation for thermal deformation in additive manufacturing processes," in *International Manufacturing Science and Engineering Conference*, vol. 49910. American Society of Mechanical Engineers, 2016, p. V003T08A006.

[166] J. Francis and L. Bian, "Deep learning for distortion prediction in laser-based additive manufacturing using big data," *Manufacturing Letters*, vol. 20, p. 10–14, 2019. [Online]. Available: https://linkinghub.elsevier.com/retrieve/pii/S221384631830172X

[167] P. Nath, J. D. Olson, S. Mahadevan, and Y.-T. T. Lee, "Optimization of fused filament fabrication process parameters under uncertainty to maximize part geometry accuracy," *Additive Manufacturing*, vol. 35, p. 101331, Oct 2020. [Online]. Available: https://www.sciencedirect.com/science/article/pii/S221486042030703X

[168] P. Shah, R. Racasan, and P. Bills, "Comparison of different additive manufacturing methods using computed tomography," *Case Studies in Nondestructive Testing and Evaluation*, vol. 6, p. 69–78, Nov. 2016. [Online]. Available: https://www.sciencedirect.com/science/article/pii/S2214657116300260

[169] A. Wang, S. Song, Q. Huang, and F. Tsung, "In-plane shape-deviation modeling and compensation for fused deposition modeling processes," *IEEE Transactions on Automation Science and Engineering*, vol. 14, no. 2, p. 968–976, Apr 2017.

[170] H. Luan and Q. Huang, "Prescriptive modeling and compensation of in-plane shape deformation for 3-d printed freeform products," *IEEE Transactions on Automation Science and Engineering*, vol. 14, no. 1, p. 73–82, Jan 2017.

[171] Y. Wang, C. Ruiz, and Q. Huang, "Learning and predicting shape deviations of smooth and non-smooth 3d geometries through mathematical decomposition of additive manufacturing," *IEEE Transactions on Automation Science and Engineering*, 2022.

[172] A. Sabbaghi, Q. Huang, and T. Dasgupta, "Bayesian model building from small samples of disparate data for capturing in-plane deviation in additive manufacturing," *Technometrics*, vol. 60, no. 4, pp. 532–544, 2018.

[173] A. Sabbaghi and Q. Huang, "Model transfer across additive manufacturing processes via mean effect equivalence of lurking variables," *The Annals of Applied Statistics*, vol. 12, no. 4, pp. 2409–2429, 2018.

[174] F. Tsung, K. Zhang, L. Cheng, and Z. Song, "Statistical transfer learning: A review and some extensions to statistical process control," *Quality Engineering*, vol. 30, no. 1, pp. 115–128, 2018.

[175] R. d. S. B. Ferreira, A. Sabbaghi, and Q. Huang, "Automated geometric shape deviation modeling for additive manufacturing systems via bayesian neural networks," *IEEE Transactions on Automation Science and Engineering*, vol. 17, no. 2, pp. 584–598, 2019.

[176] C. Tao, J. Du, and T.-S. Chang, "Anomaly detection for fabricated artifact by using unstructured 3d point cloud data," *IISE Transactions*, vol. 55, no. 11, p. 1174–1186, Nov 2023. [Online]. Available: https://www.tandfonline.com/doi/full/10.1080/24725854.2022.2152140

[177] Q. Huang, "An impulse response formulation for small-sample learning and control of additive manufacturing quality," *IISE Transactions*, pp. 1–14, 2022.

[178] M. Khanzadeh, P. Rao, R. Jafari-Marandi, B. K. Smith, M. A. Tschopp, and L. Bian, "Quantifying geometric accuracy with unsupervised machine learning: Using self-organizing map on fused filament fabrication additive manufacturing parts," *Journal of Manufacturing Science and Engineering*, vol. 140, no. 3, 2018.

[179] L. Breiman, "Random forests," *Machine Learning*, vol. 45, no. 1, p. 5–32, Oct. 2001. [Online]. Available: https://doi.org/10.1023/A:1010933404324

[180] L. Li, R. McGuan, R. Isaac, P. Kavehpour, and R. Candler, "Improving precision of material extrusion 3d printing by in-situ monitoring & predicting 3d geometric deviation using conditional adversarial networks," *Additive Manufacturing*, vol. 38, p. 101695, Feb 2021. [Online]. Available: https://www.sciencedirect.com/science/article/pii/S2214860420310678

[181] D. J. McGregor, M. V. Bimrose, C. Shao, S. Tawfick, and W. P. King, "Using machine learning to predict dimensions and qualify diverse part designs across multiple additive machines and materials," *Additive Manufacturing*, vol. 55, p. 102848, Jul 2022. [Online]. Available: https://www.sciencedirect.com/science/article/pii/S2214860422002470

[182] J. J. Hopfield, "Artificial neural networks," *IEEE Circuits and Devices Magazine*, vol. 4, no. 5, pp. 3–10, 1988.

[183] A. Krizhevsky, I. Sutskever, and G. E. Hinton, "Imagenet classification with deep convolutional neural networks," *Communications of the ACM*, vol. 60, no. 6, pp. 84–90, 2017.

[184] Y. Pu, Z. Gan, R. Henao, X. Yuan, C. Li, A. Stevens, and L. Carin, "Variational autoencoder for deep learning of images, labels and captions," *Advances in neural information processing systems*, vol. 29, 2016.

[185] L. Alzubaidi, J. Zhang, A. J. Humaidi, A. Al-Dujaili, Y. Duan, O. Al-Shamma, J. Santamaría, M. A. Fadhel, M. Al-Amidie, and L. Farhan, "Review of deep learning: concepts, cnn architectures, challenges, applications, future directions," *Journal of Big Data*, vol. 8, no. 1, p. 53, Mar. 2021. [Online]. Available: https://doi.org/10.1186/s40537-021-00444-8

[186] R. Geirhos, C. R. Temme, J. Rauber, H. H. Schütt, M. Bethge, and F. A. Wichmann, "Generalisation in humans and deep neural networks," *Advances in neural information processing systems*, vol. 31, 2018.

[187] A. Garcia-Garcia, F. Gomez-Donoso, J. Garcia-Rodriguez, S. Orts-Escolano, M. Cazorla, and J. Azorin-Lopez, "Pointnet: A 3d convolutional neural network for real-time object class recognition," in *2016 International joint conference on neural networks (IJCNN)*. IEEE, 2016, pp. 1578–1584.

[188] R. Hanocka, A. Hertz, N. Fish, R. Giryes, S. Fleishman, and D. Cohen-Or, "Meshcnn: a network with an edge," *ACM Transactions on Graphics (TOG)*, vol. 38, no. 4, pp. 1–12, 2019.

[189] C. R. Qi, L. Yi, H. Su, and L. J. Guibas, "Pointnet++: Deep hierarchical feature learning on point sets in a metric space," *Advances in neural information processing systems*, vol. 30, 2017.

[190] S. Song, S. P. Lichtenberg, and J. Xiao, "Sun rgb-d: A rgb-d scene understanding benchmark suite," in *Proceedings of the IEEE conference on computer vision and pattern recognition*, 2015, pp. 567–576.

[191] Q. Tan, L. Gao, Y.-K. Lai, and S. Xia, "Variational autoencoders for deforming 3d mesh models," in *Proceedings of the IEEE conference on computer vision and pattern recognition*, 2018, pp. 5841–5850.

[192] M. Jadayel and F. Khameneifar, "Improving geometric accuracy of 3d printed parts using 3d metrology feedback and mesh morphing," *Journal of Manufacturing and Materials Processing*, vol. 4, no. 4, p. 112, Dec 2020. [Online]. Available: https://www.mdpi.com/2504-4494/4/4/112

[193] J. L. Bentley, "Multidimensional binary search trees used for associative searching," *Communications of the ACM*, vol. 18, no. 9, p. 509–517, Sep 1975. [Online]. Available: https://doi.org/10.1145/361002.361007

[194] K. He, X. Zhang, S. Ren, and J. Sun, "Deep residual learning for image recognition," *CoRR*, vol. abs/1512.03385, 2015. [Online]. Available: http://arxiv.org/abs/1512.03385

[195] A. Paszke, S. Gross, F. Massa, A. Lerer, J. Bradbury, G. Chanan, T. Killeen, Z. Lin, N. Gimelshein, L. Antiga, A. Desmaison, A. Kopf, E. Yang, Z. DeVito, M. Raison, A. Tejani, S. Chilamkurthy, B. Steiner, L. Fang, J. Bai, and S. Chintala, "Pytorch: An imperative style, high-performance deep learning library," in *Advances in Neural Information Processing Systems 32*. Curran Associates, Inc., 2019, pp. 8024–8035. [Online]. Available: http://papers.neurips.cc/paper/9015-pytorch-an-imperative-style-high-performance-deep-learning-library.pdf

[196] Q. Wang, Y. Ma, K. Zhao, and Y. Tian, "A comprehensive survey of loss functions in machine learning," *Annals of Data Science*, vol. 9, no. 2, p. 187–212, Apr 2022. [Online]. Available: https://doi.org/10.1007/s40745-020-00253-5

[197] N. Srivastava, G. Hinton, A. Krizhevsky, I. Sutskever, and R. Salakhutdinov, "Dropout: a simple way to prevent neural networks from overfitting," *The journal of machine learning research*, vol. 15, no. 1, pp. 1929–1958, 2014.

[198] L. Biewald, "Experiment tracking with weights and biases," 2020, software available from wandb.com. [Online]. Available: https://www.wandb.com/

[199] D. P. Kingma and J. Ba, "Adam: A method for stochastic optimization," *arXiv preprint arXiv:1412.6980*, 2014.

[200] C. Darken, J. Chang, and J. Moody, "Learning rate schedules for faster stochastic gradient search," in *Neural Networks for Signal Processing II Proceedings of the 1992 IEEE Workshop*, Aug. 1992, p. 3–12. [Online]. Available: https://ieeexplore.ieee.org/abstract/document/253713/citations#citations

[201] C. Zhang, S. Bengio, M. Hardt, B. Recht, and O. Vinyals, "Understanding deep learning requires rethinking generalization," no. arXiv:1611.03530, Feb. 2017, arXiv:1611.03530 [cs]. [Online]. Available: http://arxiv.org/abs/1611.03530

[202] M. Khorasani, A. Ghasemi, B. Rolfe, and I. Gibson, "Additive manufacturing a powerful tool for the aerospace industry," *Rapid Prototyping Journal*, vol. 28, no. 1, p. 87–100, Jan. 2021. [Online]. Available: https://doi.org/10.1108/RPJ-01-2021-0009

[203] H. Kim, Y. Lin, and T.-L. B. Tseng, "A review on quality control in additive manufacturing," *Rapid Prototyping Journal*, vol. 24, no. 3, p. 645–669, Jan. 2018. [Online]. Available: https://doi.org/10.1108/RPJ-03-2017-0048

[204] R. Wang, A. C. Law, D. Garcia, S. Yang, and Z. Kong, "Development of structured light 3d-scanner with high spatial resolution and its applications for additive manufacturing quality assurance," *The International Journal of Advanced Manufacturing Technology*, vol. 117, no. 3, p. 845–862, Nov. 2021. [Online]. Available: https://doi.org/10.1007/s00170-021-07780-2

[205] R. Bonin, F. Khameneifar, and J. Mayer, "Evaluation of the metrological performance of a handheld 3d laser scanner using a pseudo-3d ball-lattice artifact," *Sensors*, vol. 21, no. 6, p. 2137, Mar. 2021. [Online]. Available: https://www.mdpi.com/1424-8220/21/6/2137

[206] W. Sun, Z. Zhang, W. Ren, J. Mazumder, and J. J. Jin, "In situ monitoring of optical emission spectra for microscopic pores in metal additive manufacturing," *Journal of*

Manufacturing Science and Engineering, vol. 144, no. 1, p. 011006, Jan. 2022. [Online]. Available: https://asmedigitalcollection.asme.org/manufacturingscience/article/144/1/011006/1111564/In-Situ-Monitoring-of-Optical-Emission-Spectra-for

[207] J. Qin, F. Hu, Y. Liu, P. Witherell, C. C. L. Wang, D. W. Rosen, T. W. Simpson, Y. Lu, and Q. Tang, "Research and application of machine learning for additive manufacturing," *Additive Manufacturing*, vol. 52, p. 102691, Apr. 2022. [Online]. Available: https://www.sciencedirect.com/science/article/pii/S2214860422000963

[208] [Online]. Available: https://help.prusa3d.com/article/faq-frequently-asked-questions_1932

[209] J. C. Gower, "Generalized procrustes analysis," *Psychometrika*, vol. 40, no. 1, p. 33–51, 1975. [Online]. Available: http://link.springer.com/10.1007/BF02291478